JETP Letters, Vol. 77, No. 2, 2003, pp. 104–107. Translated from Pis'ma v Zhurnal Éksperimental'noĭ i Teoreticheskoĭ Fiziki, Vol. 77, No. 2, 2003, pp. 109–113.

Reconstruction of Heterogeneous Single-Channel Neutralization Kinetics by the Method of Fast-Ion Grazing Scattering from Metal Surfaces

E. A. Andreev* and F. I. Dalidchik

Semenov Institute of Chemical Physics, Russian Academy of Sciences, ul. Kosygina 4, Moscow, 117977 Russia

** e-mail: rsa@center.chph.ras.ru*

Received December 24, 2002

A method is suggested for the unambiguous reconstruction of the heterogeneous slow-ion neutralization kinetics near the surface of a conductor. The method is based on the special features of fast-ion grazing scattering with above-thermal energies of translational motion along the normal. It is shown that the angular distributions of fast particles reflected from the surface are related to the slow-ion neutralization rate by a simple algebraic expression. The method allows the reconstruction of the coordinate dependence for the neutralization rate and the interaction potentials. Its possibilities are demonstrated by the example of neutralizing fast He^+ ions (ion energies $E_1 \approx 2$ keV and glancing angles $\theta_0 \approx 0.5°$–$0.8°$) scattered from the Al(111) surface. © *2003 MAIK "Nauka/Interperiodica".*

PACS numbers: 68.49.Sf; 68.43.-h

Heterogeneous neutralization of slow ions is at the basis of two modern spectroscopic methods for studying the structure of the electronic subsystem of solid surfaces (SSs): ion-neutralization Auger spectroscopy [1] and spectroscopy of resonance and threshold features in the currents of reflected particles [2]. For low velocities of an ion approaching the surface and a rather large difference in the atomic ionization potential and metal work function, the neutralization events can be considered irreversible. In the case of single-channel neutralization accompanied by the formation of only unexcited particles (as, e.g., for the majority of inert gases interacting with metals whose work function exceeds the excited-state ionization potential), the electron-transition kinetics are described by the simplest equation for the number of ions N_i:

$$\dot{N}_i(\mathbf{R}, t) = -\Gamma(\mathbf{R})N_i(\mathbf{R}, t), \qquad (1)$$

where $\Gamma(\mathbf{R})$ is the neutralization rate of an ion fixed at the point specified by the vector $\mathbf{R}$. The progress in the implementation of spectroscopic possibilities of the above-mentioned ion-neutralization methods depends essentially on the accuracy of determining the function $\Gamma(\mathbf{R})$ and the interaction potential $U_i(\mathbf{R})$ that determines the ion trajectory $\mathbf{R}(t)$. These functions are ordinarily found by the trial-and-error procedure using various approximations and by fitting the calculated energy dependences of survival probabilities to the experimental energy dependences of the reflected ion currents. The disadvantages of this way of reconstructing the neutralization rates are quite evident. The reliability of the obtained results depends substantially on the quality of the chosen approximation. The purpose of this communication is to show that the kinetics of electronic transitions accompanying the motion of atomic particles near the SS can be unambiguously reconstructed from measurements of the angular distributions of neutral atoms that are formed upon the grazing scattering of fast ions. Below, it will be shown that the results of angular measurements of the scattered particles would suffice to unambiguously reconstruct Γ and U_i as functions of the distance Z from the ion to the metal surface.

The grazing scattering regime of fast atomic particles from the solid surface (glancing angles $\theta_0 \approx 0.5°$–$5°$ and particle energies $E_1 \sim 1$–10 keV) has a number of kinematic features, which were studied in [3–7]. For fast motion along the surface, the potentials $U(\mathbf{R})$ and the electron-transition rates $\Gamma(\mathbf{R})$ are effectively averaged. As a result, the dynamics of particle motion and the electron-transition kinetics are governed by the quantities that depend only on the coordinate Z. The energy of ion (or the formed atom) motion along the normal to the surface ($E_2 = E_1\sin^2\theta_0$), which, hence, determines the character of particle–surface interaction, comprises only 0.03–10 eV. The grazing scattering of the nonneutralized fast ions is virtually specular; the corresponding angle of reflection $\theta_f = \theta_0$, and its scatter $\Delta\theta_f \ll \theta_0$. The neutralization is accompanied by a change of the particle–surface interaction potential.

Because of this, the angle of reflection is a function of the coordinate Z at the time of neutralization:

$$\theta^2 = \theta_0^2 + \Delta U(Z)/E_1. \quad (2)$$

Here, $U = (U_i - U_a)$ and $U_{i,a}(Z) \longrightarrow 0$ as $Z \longrightarrow \infty$ (indices i and a refer, respectively, to the ion and ground-state atom). If $\Delta U \gtrsim E_1\theta_0$ in the electron-transition region, then one has $\Delta\theta \gtrsim \theta_0$ for the width of the angular distribution of the fast particles formed in ion-neutralization events.

The number of ions that survive to the time t, when the particle is at the distance $Z(t)$, is determined by the neutralization kinetics, which can be reconstructed if the relation between the angular distribution of fast neutral atoms and the neutralization rate is known. Introduce the trajectory $Z(t)$ within the ion term of the system. Then it is straightforward to obtain from Eq. (1) the following expression for the angular distribution density $f[\theta(Z)]$ of the reflected ground-state atoms, which takes into account the two-valued character of the function $t(Z)$:

$$f[\theta(Z)] = \Gamma_{ia}(Z)\exp(-q)2\cosh[\chi(Z)]/\left[v_i(Z)\left|\frac{\partial\theta(Z)}{\partial Z}\right|\right],$$
$$\chi(Z) = \int_{Z_t}^{Z}\Gamma_{ia}(Z)\frac{dZ}{v_i(Z)}. \quad (3)$$

Here, Γ_{ia} is the electron-transition rate, v_i is the absolute value of ion velocity, Z_t is the coordinate of the turning point on the ion trajectory, and $q = \chi(Z = \infty)$. The function $\Delta U(Z)$ is assumed to be monotonic. Taking into account that $\Gamma_{ia}[Z(t)] = \partial\chi[Z(t)]/\partial t$, we obtain the following relation for the angular distribution:

$$P(\theta) = \int_{\theta}^{\theta_t} f(\theta')d\theta' = 2\exp(-q)\sinh(\chi), \quad (4)$$

where θ_t is the maximal angular deviation caused by the electronic transition at the turning point Z_t and $\theta_t = \theta(Z_t)$. The total neutralization probability in the collision is

$$P_a = 1 - \exp(-2q) = P(\theta_0). \quad (5)$$

Relations (2)–(5) can be used to obtain the following expression for the neutralization rate:

$$\Gamma_{ia}(Z) = f[\theta(Z)]\frac{v_i(Z)|\Delta F(Z)|}{2E_1\theta(Z)}/\sqrt{4P_i + P[\theta(Z)]^2}, \quad (6)$$

where $\Delta F = -\partial\Delta U/\partial Z$ and $P_i = 1 - P_a$.

When analyzing the dependence of angular distribution on the neutralization rate, the following qualitatively different situations can be distinguished. At $P_i \ll 1$, the neutralization mainly occurs before the turning point, and $f(\theta)$ has a maximum between the angles θ_0 and θ_t.

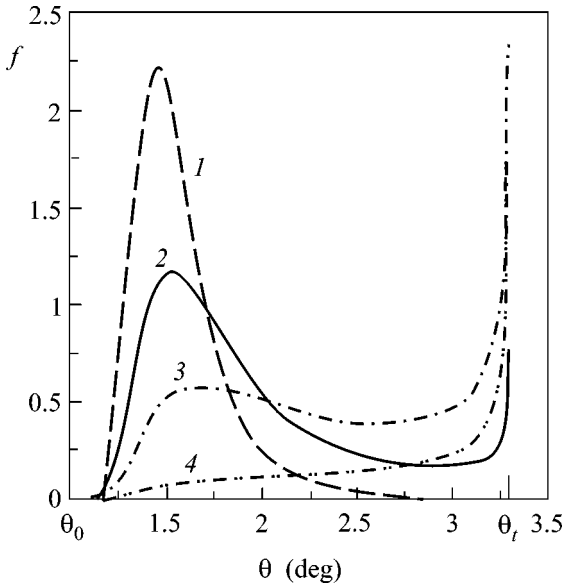

Fig. 1. Various types of angular distribution of neutral atoms formed by the neutralization of fast ions in their grazing scattering from solid surface (scattering parameters are given in the text).

In the other limiting case, $P_a \ll 1$, the neutralization events mainly occur near the turning point, and the scattered beam contains only a small fraction of neutral atoms, whose angular distribution is concentrated near θ_t and displays the rainbow effect. The results of numerical calculations illustrating these conclusions are presented in Fig. 1. The distributions were obtained for the model with the following parameters:[1] $U_a(Z) = A\exp(-\alpha Z)$; $\Delta U(Z) = -1/4Z$; $\Gamma_{ia}(Z) = C\exp(-\gamma Z)$, $E_1 = 2$ keV, $\theta_0 = 1°$, mass of the incident atom $m = 4$ au, $A = 300$ eV, $\alpha = 3$, and $\gamma = 1.12$. Four values of parameter C were used in calculations: 0.2, 0.1, 0.05, and 0.002 (curves *1–4*, respectively). The calculated neutralization probabilities P_a are 0.999999, 0.9999, 0.99, and 0.17. In this model, Z is measured from the plane of the so-called image forces; this plane does not necessarily coincide with the plane of surface atoms. The fact that the rainbow effect arises at rather large P_a values is noteworthy (curves *2*, *3* in Fig. 1).

Measurements of $f(\theta)$ for two different values of E_2 (initial energy of particle motion along the normal to the surface) and the determination of the corresponding values of P_a provide, in principle, the possibility of determining Γ_{ia}, U_i, and U_a as functions of ΔU. In the method suggested, the function $U_a(Z)$ is assumed to be known and $\Delta U(Z)$ is assumed to be monotonic. As a result, the functions $\Gamma_{ia}(Z)$ and $U_i(Z)$ can be reconstructed unambiguously. Note that, for the practical implementation of this procedure, the angular distributions for different values of E_2 should be essentially dif-

[1] Atomic units are used, unless otherwise stated.

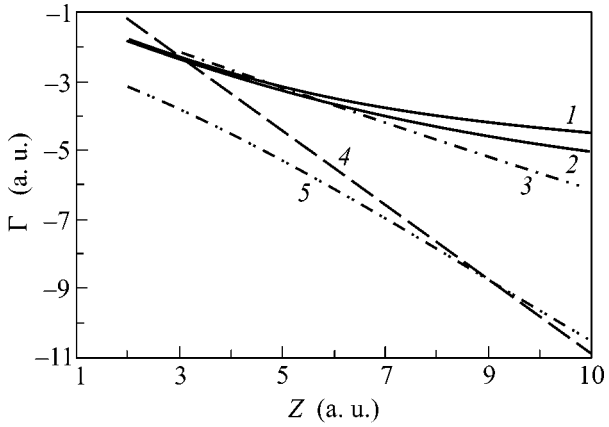

Fig. 2. Coordinate dependences of the neutralization rate $\Gamma_{ia}(Z)$.

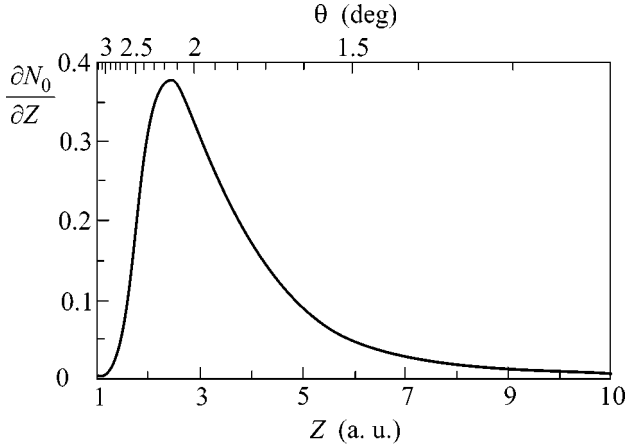

Fig. 3. Kinetic curve for the neutralization of He^+ ions (E_1 = 2.3 keV, $\theta_0 = 0.79°$) in their collisions with the Al(111) surface. Calculations are carried out with the reconstructed $\Gamma_{ia}(Z)$ function.

ferent from each other. The features caused by the rainbow effect in the angular distribution of the resulting neutral atoms can also be used to determine the parameters of interaction potential at the trajectory turning point, because $U_i(Z_t) = E_2$, while $\Delta U(Z_t)$ is determined from Eq. (1).

In [8, 9], angular distributions of the He atoms formed upon the grazing scattering of He^+ ions from the Al(111) surface were measured. The collision parameters were E_1 = 2.0 and 2.3 keV, $\theta_0 = 0.5°$ and 0.79°, and E_2 = 0.15 and 0.44 eV. In the cited works, the following expression was suggested for the neutralization rate: $\Gamma_1(Z) = 10\exp(-2.5Z)$. It was obtained by fitting the corresponding parameters to the experimental result. There are some considerations that cast doubt not only on this expression but also on the reliability of the procedure used for determining the neutralization rate. There is no rational physical interpretation of such a big exponent. At large Z, the neutralization process is controlled by the subbarrier electron transition from the surface to the ion. The probability of this transition is determined by the electron density, which decreases exponentially with increasing Z, with the exponent being $\gamma = 2(2\Phi)^{1/2}$, where Φ is the work function; for Al(111), Φ = 4.25 eV and γ = 1.12. Moreover, as was already stated, this procedure does not provide unambiguity in determining these parameters.

In our method, $\Gamma_{ia}[Z(\theta)]$ is directly expressed through $f(\theta)$. The angular distributions measured in [8, 9] for the neutral atoms are close to each other over the entire interval of scattering angles and have maxima at $\theta_m = 1.95°$ and 1.88°. From the form of these functions, one can conclude that the ion neutralization mainly proceeds before the trajectory turning point. This fact enables one to assume that the repulsive components of the potentials $U_i(Z)$ and $U_a(Z)$ can be ignored when determining $v_i(Z)$ and $\Delta F(Z)$ and restrict oneself to the image forces. The functions $\Gamma_{ia}(Z)$ reconstructed by us on the basis of the results presented in [8, 9] are shown in Fig. 2. (curves *1* and *2*, respectively). Curve *3* is the corresponding interpolation function $\Gamma_{int}(Z) = 0.15\exp(-\gamma Z)$. Curves *4* and *5* are, respectively, the above-mentioned $\Gamma_1(Z)$ and the neutralization rate calculated in [10].

In conclusion, the following is noteworthy. The possibility of determining the neutralization rate $\Gamma_{ia}(Z)$ from the directly measured angular distribution $f[\theta]$ allows one to reconstruct the ion neutralization kinetics and calculate the Auger spectra. Equation (2) determines the characteristic distances from the surface which make the greatest contribution to the heterogeneous neutralization. In particular, for the distributions obtained in [8, 9], the θ_m values presented above yield Z_m = 3.14 and 3.33, respectively. Note that the potential barrier to electron transition from metal to ion along the Z coordinate is absent for such distances. The analytic approximation of the geometrical mean of the functions $\Gamma_{ia}(Z)$ reconstructed on the basis of the results presented in [8, 9] gives $\Gamma_{ia}(Z) = B/Z^n$, with B = 0.28 and n = 4. The corresponding kinetic curve $\partial N_0/\partial Z$ is shown in Fig. 3, where N_0 is the number (normalized to unity) of atoms formed in the ground state.

The power-law $\Gamma_{ia}(Z)$ dependence, rather than the commonly accepted exponential dependence, can be explained by the absence of potential barrier to the transition of an electron with Fermi energy. This region of distances poses the greatest difficulties for the theoretical study of the Auger neutralization mechanism. For example, the attempt undertaken in [10] at calculating $\Gamma_{ia}(Z)$ for the He^+–Al(111) system gave neutralization rates differing by more than an order of magnitude from the values obtained using the experimental data (Fig. 2). The possibility of directly comparing the experimental and theoretical results is one more merit

of the problem considered. It is worth noting that this method is highly sensitive to the accuracy of measuring angular distributions. For example, the discrepancy between the $\Gamma_{ia}(Z)$ values reconstructed on the basis of the results [8, 9] (Fig. 2) is caused by the poor accuracy of measurements in the angular range $\theta_0 < \theta < \theta_m$ in [9]. Recall that the opposite edge of angular distribution ($\theta_m < \theta < \theta_t$) is of importance to the reconstruction of the parameters of interaction potential. It is thus necessary to accurately measure $f[\theta]$ for the neutral atoms over the entire range of scattering angles ($\theta_0 < \theta < \theta_t$) and not just in the vicinity of the distribution maximum.

Finally, the method suggested for reconstructing the single-channel kinetics can be used in the study of the processes with several channels. In [9], the angular distribution $f_{\text{met}}[\theta]$ was also measured for the ground-state He atoms formed in the grazing scattering of fast metastable He(2^3S) atoms with the same $\theta_0 = 0.79$ and $E_1 = 2.3$ keV as in the case of the He^+ ions. The $f_{\text{met}}[\theta]$ distribution was similar to $f[\theta]$, but it was shifted to the smaller scattering angles; the maximum of $f_{\text{met}}[\theta]$ corresponded to $\theta_{\text{met}} = 1.65°$. The following mechanism can be suggested for the heterogeneous de-excitation of metastable He atoms. When the He(2^3S) atom approaches the surface, an electron can undergo transition directly to the free metal states (above the Fermi level).[2] These transitions occur at $Z < Z_1$, where $Z_1 = 13.1$ is found from the equation

$$1/4Z_1 = I_m - \Phi, \tag{7}$$

where $I_m = 4.77$ eV is the He(2^3S) ionization potential. In this region of distances, the potential barrier to the electron motion along the normal is small (it disappears at $Z < 10$). For this reason, the electron transition with the ionization of the metastable atom can be rather fast. The resulting ion is accelerated in its motion toward the surface. However, the image force potential starts to act not at infinity but at the point 13.1, thereby shifting the distribution function to smaller angles. This shift is estimated at –0.21°. The corresponding experimental value in the region of distribution maxima is –0.23°. This fact is one more argument in favor of the mechanism suggested in this work.

This work was supported by the Russian Foundation for Basic Research, project no. 00-02-17090.

REFERENCES

1. Y. D. Hagstrum, in *Electron and Ion Spectroscopy of Solids*, Ed. by L. Fiermans (Plenum, New York, 1978).
2. M. V. Grishin, F. I. Dalidchik, S. A. Kovalevskii, *et al.*, Chem. Phys. Rep. **14**, 1069 (1995).
3. E. A. Andreev and M. Yu. Knizhnikov, Khim. Fiz. **18** (1), 26 (1999).
4. E. A. Andreev, F. I. Dalidchik, and M. Yu. Knizhnikov, Khim. Fiz. **18** (7), 27 (1999).
5. E. A. Andreev and M. Yu. Knizhnikov, Khim. Fiz. **19** (4), 11 (2000).
6. E. A. Andreev, F. I. Dalidchik, and M. Yu. Knizhnikov, Dokl. Akad. Nauk **370**, 764 (2000).
7. E. A. Andreev and F. I. Dalidchik, Chem. Phys. Lett. **356**, 233 (2002).
8. T. Heht, H. Winter, and A. G. Borisov, Surf. Sci. **406**, L607 (1998).
9. T. Heht, R. Pfandzelter, H. Winter, *et al.*, Nucl. Instrum. Methods Phys. Res. B **157**, 82 (1999).
10. N. Lorente and R. Monreal, Phys. Rev. A **49**, 4716 (1994).

[2] The temperature of the surface is assumed to be zero.

Translated by V. Sakun

JETP Letters, Vol. 77, No. 2, 2003, pp. 108–111. From Pis'ma v Zhurnal Éksperimental'noĭ i Teoreticheskoĭ Fiziki, Vol. 77, No. 2, 2003, pp. 114–117.

σ and π-Band Dispersion of Graphite from Polarized Resonant Inelastic X-ray Scattering Measurements¶

A. V. Sokolov[1], E. Z. Kurmaev[1], J. MacNaughton[2], A. Moewes[2], N. A. Skorikov[1], and L. D. Finkelstein[1]

[1] *Institute of Metal Physics, Ural Division, Russian Academy of Sciences, Yekaterinburg, 620219 Russia*

[2] *Department of Physics and Engineering Physics, University of Saskatchewan, Saskatoon, Saskatchewan S7N 5E2, Canada*

Received December 24, 2002

Resonant inelastic X-ray scattering of highly oriented pyrolytic graphite (HOPG) is observed above the C 1*s* threshold at different polarization angles. It is shown that combining the polarization and excitation energy dependence of X-ray emission spectra makes it possible to perform quantitative band mapping selective to the chemical bonding (σ and π). © *2003 MAIK "Nauka/Interperiodica".*

PACS numbers: 61.50.Lt; 61.10.Eq; 78.70.En

Nonresonant X-ray emission can exhibit radiation anisotropy or linear dichroism in anisotropic crystals [1–3]. It is shown that, using the orientation dependence of polarized X-ray emission spectra (XES) of single crystals with low symmetry, additional information about the anisotropy of chemical bonding parameters can be obtained [4]. Conversely, it was recently demonstrated that quantitative band mapping can be performed for occupied electronic states in SiC [5], diamond, graphite, and MgB_2 [6] with the help of resonant inelastic X-ray scattering (RIXS) measurements. In this paper, we combined both the polarization dependence of the X-ray absorption spectrum (XAS) and RIXS measurements to perform quantitative band mapping selective to chemical bonding. The excitation energy dependence of C *K*α XES ($2p \longrightarrow 1s$ transition) of highly oriented pyrolytic graphite was measured above the C 1*s* threshold for 0–10 eV at two different polarization geometries. The results were compared with specially performed band structure calculations of graphite.

The X-ray fluorescence measurements were performed on a Beamline 8.0 at the Advanced Light Source (ALS) at the Lawrence Berkeley National Laboratory using a fluorescence endstation, described in detail elsewhere [7]. Emitted radiation was measured using a Rowland circle type spectrometer with a large spherical grating and a photon-counting area detector. Total experimental resolution in the carbon *K*α X-ray emission region was 0.3 eV FWHM. The bandwidth of the incident photons was varied between 500 meV and 1 eV. The C 1*s* XAS was measured in total electron yield mode. The fluorescence measurements were made at the beamline using a depolarized configuration (which means that the vector **E** of the incidence beam lies in the scattering plane; i.e., we used *p* polarization), as well as with the direction of the emitted photons perpendicular to the incidence one. Two geometries were used: $\alpha = 85°$ (which is close to the normal incidence) and $\alpha = 25°$ (which is close to the grazing incidence). The variable **c** is the sample normal and **α** is the angle between incident photons and the surface of the sample.

We used the self-consistent linearized muffin–tin orbital (LMTO) method within the local density approximation (LDA) for the band structure calculation of graphite (TBLMTO-47 computer code [8]). The tetrahedron method was used to calculate the dispersion curves $E(\mathbf{k})$ with 1152 **k** points.

Initially, we studied the polarization dependence of the near-edge X-ray absorption fine structure of graphite. The transition matrix element **M** in the X-ray absorption process contains the scalar product of the polarization vector of the incoming photon, **E**, and the position vector of the electron, **r**. The expression is

$$M = \langle \varphi_{1s} | \mathbf{E} \cdot \mathbf{r} | \varphi_f \rangle,$$

where φ_{1s} is the wave function of the C 1*s* core electron and φ_f is the wave function of the final state into which the 1*s* electron is excited [9]. The dipole transition operator $\mathbf{E} \cdot \mathbf{r}$ projects orbitals along the direction of the polarization vector. Therefore, the orbital-symmetry-dependent absorption spectra can be obtained using linearly polarized synchrotron radiation. In highly oriented pyrolytic graphite, the **c** axis coincides with the sample normal. This means that the p_z or out-of-plane orbitals (π*-bands) are mainly excited at *K* edges or when $\mathbf{E} \parallel \mathbf{c}$. Similarly, the $p_{x,y}$ or in-plane orbitals (σ* bands) are preferentially excited when $\mathbf{E} \perp \mathbf{c}$.

¶This article was submitted by the authors in English.

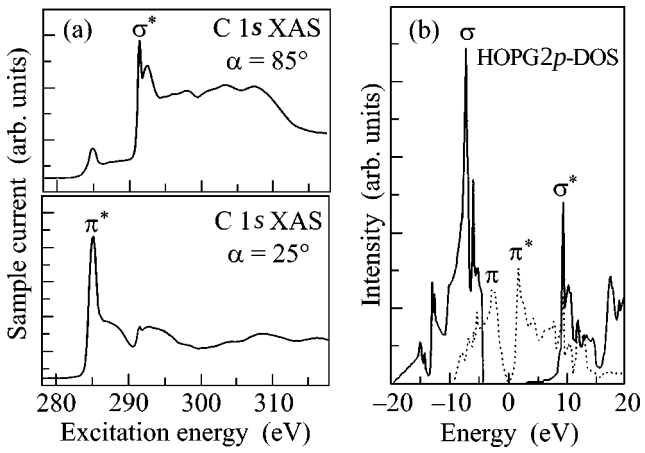

Fig. 1. (a) C 1*s* XAS of graphite measured at polarization angles α = 25° and 85°; (b) C 2*p*-DOS separated for σ and π states.

Figure 1a shows C 1*s* XAS of graphite measured at different incidence angles (α = 85° and α = 25°) and Fig. 1b shows the 2*p*-DOS calculations separately for π and σ bonds. As observed, the fine structure of C 1*s* XAS is very sensitive to the incidence angle. The absorption peak located at 285 eV caused by the dominant π* states [10] is enhanced at α = 25°. Alternately, at normal incidence (α = 85°) the σ* states are mainly probed and the absorption peak located at 291.5 eV has the highest intensity.

The excitation energy dependence of the X-ray emission spectra measured for different incidence angles (α = 25° and α = 85°) is presented in Figs. 2 and 3. The excitation energies were selected according to features (*a–h*) in the C 1*s* XAS (indicated by arrows in Figs. 2, 3). Excitation energies *a–h* have the same values for both incidence angles. The intensities of each emission spectrum have been normalized to the incident flux.

Abiding by the dipole selection rules, the carbon *K*α XES of graphite probes the occupied 2*p* states. This process depends strongly on the excitation energy of incoming photons and varies significantly for the two angles chosen.

When the excitation energy shifts above the *K* edge, the fine structure of C *K*α XES changes dramatically. Instead of linear dispersion, the peaks move in a nonlinear fashion. Some of these features move in a manner opposite to the increasing excitation energy. To interpret these spectra, we used the concept [11] that the absorption–emission process should be treated as a single inelastic scattering process with well-defined crystal momentum conservation for both the photoelectron and the hole in the valence band. This indicates that, when a core electron is promoted to a conduction band with a certain crystal momentum, resulting emission

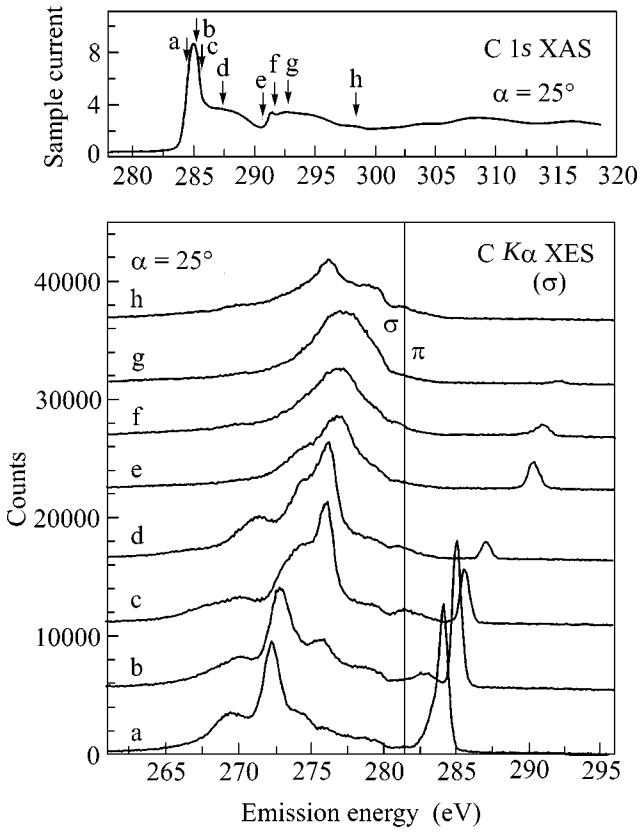

Fig. 2. Excitation energy dependence of C *K*α XES of graphite measured for incidence angle α = 25°.

from the valence band at the same point in the Brillouin zone will be induced.

To compare the presented spectra for two angles, one should take into account the fact that the contribution of π and σ states to the emission process is determined by the direction in which we register emitted photons. If this outgoing direction is parallel to the **c** axis, then the polarization vector of emitted photons is parallel to the sample surface and thus the dominant component is σ. In the opposite situation, when the direction of departing photons is perpendicular to the **c** axis, the polarization vector of the emitted photons is either parallel to the *c* direction or to one of the directions in the sample surface, producing both π and σ contributions. Our results indicate that the direction of registration is perpendicular to the incident direction. Thus, for incidence angle α = 25° (close to grazing incidence), the direction of registration of the emitted photons is nearly parallel to the *c* axis and the dominant component is σ. For α = 85° (close to normal incidence), the direction of registration is nearly perpendicular to the *c* axis, and we have both π and σ components.

All the features of the RIXS for α = 25° are results of the σ component, with the exception of those in the high-energy field of the valence band. These π states for

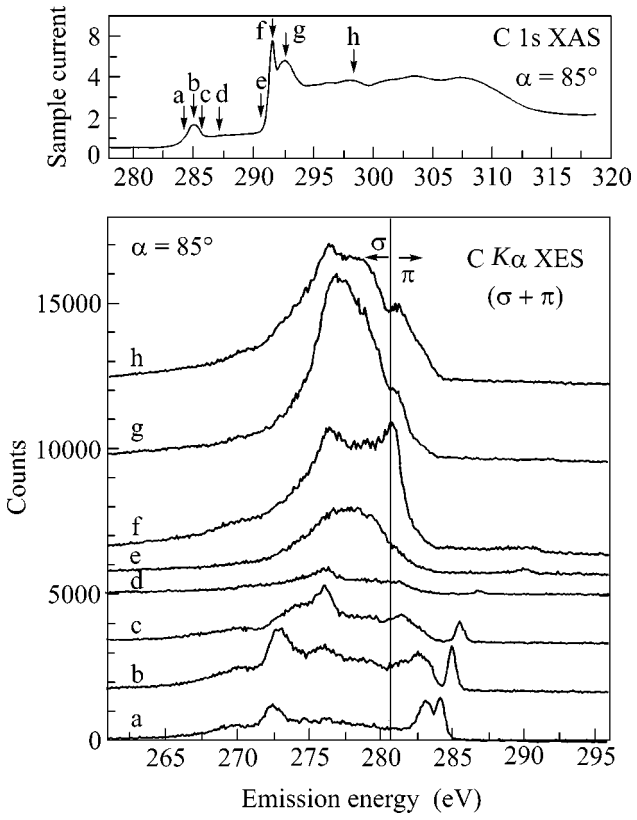

Fig. 3. Excitation energy dependence of C *K*α XES of graphite measured for incidence angle α = 85°.

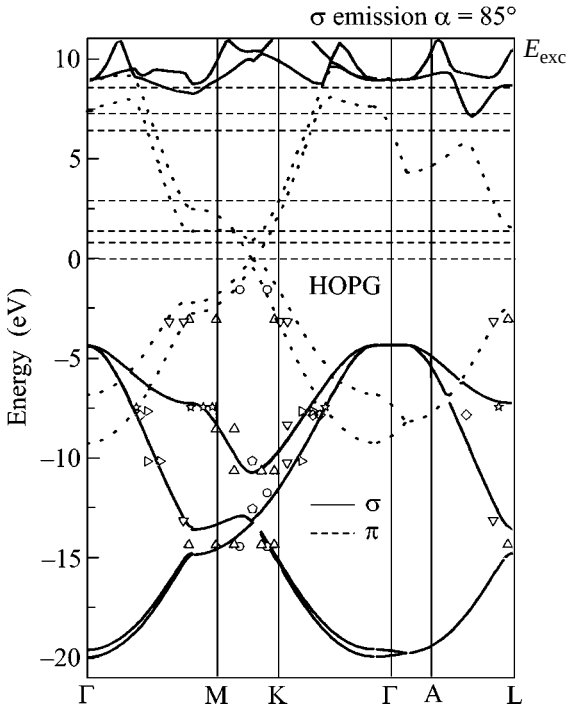

Fig. 4. Band mapping using resonant inelastic X-ray scattering: (lines) calculated band structure and (dots) experimental results (for α = 25°; values of E_{exc} are: (★) 292.9, (◇) 291.7, (▷) 290.8, (▽) 287.3, (△) 285.8, (○) 285.2, and (◊) 285.4).

excitation energies *b–d* appear because the registration of emitted photons is not strictly parallel to the **c** axis. For α = 85° with both π and σ components are allowed in the emission process, the π (high-energy) features are more considerable in the whole excitation energy range. The strong elastic peaks corresponding to α = 25° occur because of their localized character and the strong deviation from grazing incidence that results in the permissibility of π* states in the emission process.

To construct the experimental dispersion curves from selectively excited X-ray emission spectra, we used the procedure described in [5, 6]. According to this procedure, the top of the valence band corresponding to the calculated zero in the energy scale is related to the XPS C 1*s* binding energy of 284.5 eV measured for graphite [12]. For the band mapping procedure, we used only the inelastic part of the spectra. The possible values of the **k** vector for excited C 1*s* electrons are determined by the intersection of the selected excitation energy and the calculated dispersion curves for the 2*p*-vacant states. Using **k**-momentum conservation, vertical lines from intersection points are drawn down on dispersion curves for occupied states. The occupied states revealed by features in the carbon *K*α XES for selected excitation energies can be indicated by horizontal lines on the dispersion curves for occupied 2*p*-states. The intersection points of horizontal and vertical lines give the experimental points on dispersion curves for the occupied states.

As a result, the quantitative band mapping selective to the chemical bonding (π and σ) was realized for α = 25° (Fig. 4). The obtained results show a good agreement between experiment (points) and calculated dispersion curves for occupied π (dotted lines) and σ (solid lines) states of graphite, which are located at the top and the bottom of the valence band, respectively.

In conclusion, we have shown that resonant inelastic X-ray scattering spectra measured at different incidence angles can be used for quantitative band mapping selective to the chemical bonding using the *p* polarization of the incoming photons. This technique has advantages with respect to angle-resolved photoemission because of the higher sensitivity to the chemical bonding and a greater potential for probing the **k**-resolved electronic structure of layered materials.

This work was supported by the Russian Foundation for Basic Research (project no. 00-15-96575) and the National Sciences and Engineering Research Council (NSERC). The work at the Advanced Light Source at Lawrence Berkeley National Laboratory was supported by the U.S. Department of Energy (contract no. DE-AC03-76SF00098).

REFERENCES

1. I. B. Borovskii, V. I. Matiskin, and V. I. Nefedov, J. Phys. (Paris) **32**, C4-207 (1971).
2. V. M. Cherkashenko, E. Z. Kurmaev, and V. L. Volkov, J. Electron Spectrosc. Relat. Phenom. **28**, 1 (1982); S. P. Freidman, V. M. Cherkashenko, V. A. Gubanov, *et al.*, Z. Phys. B **46**, 31 (1982).
3. G. Drager and O. Brummer, Phys. Status Solidi B **124**, 300 (1984).
4. Chr. Beyreuther, R. Hierl, and G. Wiech, Ber. Bunsen-Ges. Phys. Chem. **79**, 1082 (1975).
5. J. Luning, J. -E. Rubensson, C. Ellmers, *et al.*, Phys. Rev. B **56**, 13147 (1997).
6. A. V. Sokolov, E. Z. Kurmaev, S. Leitch, *et al*. (in press).
7. J. J. Jia, T. A. Callcott, J. Yurkas, *et al.*, Rev. Sci. Instrum. **66**, 1394 (1995).
8. O. K. Anderson, Phys. Rev. B **12**, 3060 (1975).
9. J. Stohr, *NEXAFS Spectroscopy* (Springer, Berlin, 1992).
10. D. M. Gruen, A. R. Krauss, C. D. Zuiker, *et al.*, Appl. Phys. Lett. **68**, 1640 (1996).
11. Y. Ma, N. Wassdahl, P. Skytt, *et al.*, Phys. Rev. Lett. **69**, 2598 (1992).
12. J. F. Moulder *et al.*, *Handbook of X-Ray Photoelectron Spectroscopy* (Perkin–Elmer, Eden Prairie, MN, 1992).

JETP Letters, Vol. 77, No. 2, 2003, pp. 112–114. Translated from Pis'ma v Zhurnal Éksperimental'noĭ i Teoreticheskoĭ Fiziki, Vol. 77, No. 2, 2003, pp. 118–120.

Influence of Long-Range Effects on the Critical Behavior of Three-Dimensional Systems

S. V. Belim

Omsk State University, pr. Mira 55, Omsk, 644077 Russia

e-mail: belim@univer.omsk.su

Received December 16, 2002

The Padé–Borel resummation technique is used to describe field-theoretically, in the two-loop approximation, the behavior of Ising systems with long-range effects directly in a three-dimensional space. The renormalization-group equations are analyzed and the fixed points governing the critical behavior of the system are determined. It is shown that the long-range effects can bring about a change in both the regime of critical behavior and the kind of phase transition. *© 2003 MAIK "Nauka/Interperiodica".*

PACS numbers: 75.10.-b; 64.60.Ak; 11.10.Lm

The influence of long-range effects showing a power-law behavior $1/r^{-D-a}$ at large distances has been studied analytically within the framework of the ε-expansion approach [1–3] and numerically by the Monte Carlo method [4–6] for one- and two-dimensional systems. It was shown that, for $a < 2$, these effects have a sizable influence on the critical behavior of Ising systems. However, up to now, this problem has not been solved analytically directly for the space dimensionality $D = 3$. Nevertheless, such a description is necessary because of a poor convergence of the ε-expansion series. In this work, the critical behavior of three- dimensional Ising systems is described with allowance for long-range effects and for different values of parameter a.

The Hamiltonian of a system with long-range effects can be written as

$$H = \int d^D q \left\{ \frac{1}{2}(\tau_0 + q^a)\varphi^2 + u_0\varphi^4 \right\}, \qquad (1)$$

where φ is the order-parameter fluctuations, D is the space dimensionality, $\tau_0 \sim |T - T_c|$, T_c is the critical temperature, and u_0 is a positive constant. The critical behavior depends essentially on the parameter a that determines the rate of interaction decay with increasing distance. As was shown in [1], the influence of long-range effects is appreciable for $0 < a < 2$, while the critical behavior at $a \geq 2$ is equivalent to the behavior of short-range systems. For this reason, we restrict ourselves in what follows to the case $0 < a < 2$.

The standard renormalization-group procedure based on the Feynman diagrams [7] with the $G(\mathbf{k}) = 1/(\tau + |\mathbf{k}|^a)$ propagator yields the following expressions for the functions β, γ_φ, and γ_t specifying the differential renormalization-group equation:

$$\beta = -(4-D)\left[1 - 36uJ_0 + 1728\left(2J_1 - J_0^2 - \frac{2}{9}G\right)u^2\right],$$

$$\gamma_t = (4-D)\left[-12uJ_0 + 288\left(2J_1 - J_0^2 - \frac{1}{3}G\right)u^2\right],$$

$$\gamma_\varphi = (4-D)96Gu^2,$$

$$J_1 = \int \frac{d^D q d^D p}{(1+|\mathbf{q}|^a)^2(1+|\mathbf{p}|^a)(1+|q^2+p^2+2\mathbf{pq}|^{a/2})}, \qquad (2)$$

$$J_0 = \int \frac{d^D q}{(1+|\mathbf{q}|^a)^2},$$

$$G = -\frac{\partial}{\partial|\mathbf{k}|^a} \times \int \frac{d^D q d^D p}{(1+|q^2+k^2+2\mathbf{kq}|^a)(1+|\mathbf{p}|^a)(1+|q^2+p^2+2\mathbf{pq}|^{a/2})}.$$

Let us redefine the effective interaction vertex as

$$v = u/J_0. \qquad (3)$$

As a result, we arrive at the following expressions for the functions β, γ_φ, and γ_t:

$$\beta = -(4-D)\left[1 - 36v + 1728\left(2\tilde{J}_1 - 1 - \frac{2}{9}\tilde{G}\right)v^2\right],$$

$$\gamma_t = (4-D)\left[-12v + 288\left(2\tilde{J}_1 - 1 - \frac{1}{3}\tilde{G}\right)v^2\right], \qquad (4)$$

$$\gamma_\varphi = (4-D)96\tilde{G}v^2,$$

$$\tilde{J}_1 = \frac{J_1}{J_0^2} \quad \tilde{G} = \frac{G}{J_0^2}.$$

0021-3640/03/7702-0112$24.00 © 2003 MAIK "Nauka/Interperiodica"

Fixed points, stability eigenvalues, and critical indices for three-dimensional systems

a	v^*	λ	ν	α	η	γ
1.5	0.015151	0.918690	0.555566	0.333302	0.002647	1.109661
1.6	0.015974	0.874129	0.557889	0.326333	0.003936	1.113582
1.7	0.020485	0.699732	0.567334	0.297998	0.004862	1.131910
1.8	0.023230	0.628209	0.572714	0.281858	0.007461	1.141155
1.9	0.042067	0.683927	0.620054	0.139838	0.013420	1.231787

This redefinition is meaningful for $a \le D/2$. In this case, the functions J_0, J_1, and G diverge. However, after the introduction of the cutoff parameter Λ, the expressions

$$\frac{J_1}{J_0^2} = \frac{\int_0^\Lambda\int_0^\Lambda d^Dq d^Dp/((1+|\mathbf{q}|^a)^2(1+|\mathbf{p}|^a)(1+|q^2+p^2+2\mathbf{pq}|^a))}{\left[\int_0^\Lambda d^Dq/(1+|\mathbf{q}|^a)^2\right]^2},$$
$$\frac{G}{J_0^2} = \frac{-\partial/(\partial|\mathbf{k}|^a)\int_0^\Lambda\int_0^\Lambda d^Dq d^Dp/((1+|q^2+k^2+2\mathbf{kq}|^a)(1+|\mathbf{p}|^a)(1+|q^2+p^2+2\mathbf{pq}|^a))}{\left[\int_0^\Lambda d^Dq/(1+|\mathbf{q}|^a)^2\right]^2} \quad (5)$$

become finite in the limit $\Lambda \longrightarrow \infty$.

The integrals were taken numerically. In the case of $a \le D/2$, the sequence of the J_1/J_0^2 and G/J_0^2 values was constructed for different values of Λ and approximated to infinity.

The critical behavior regime is fully determined by the stable fixed points of the renormalization-group transformation; these points can be found from the condition that the β functions vanish:

$$\beta(v^*) = 0. \quad (6)$$

The condition for stability reduces to the requirement that the β-function derivative at the fixed point be positive:

$$\lambda = \partial\beta(v^*)/\partial v > 0. \quad (7)$$

The index ν characterizing the growth of the correlation radius in the vicinity of critical point ($R_c \sim |T - T_c|^{-\nu}$) is found from the expression

$$\nu = \frac{1}{2}(1+\gamma_t)^{-1}.$$

The Fisher index η describing the behavior of the correlation function in the vicinity of critical point in the wave-vector space ($G \sim k^{2+\eta}$) is determined by the scaling function γ_φ: $h = \gamma_\varphi$. Other critical indices can be determined from the scaling relations.

It is known that the perturbation-theory series are asymptotic, and the interaction vertices for the order-parameter fluctuations are too large for Eq. (4) to be directly used. For this reason, the necessary physical information was extracted from these expressions by using the Padé–Borel resummation method. The direct and inverse Borel transformations have the form

$$f(v) = \sum_i c_i v^i = \int_0^\infty e^{-t}F(vt)dt, \quad (8)$$

$$F(v) = \sum_i \frac{c_i}{i!}v^i. \quad (9)$$

The β functions were calculated using a [2/1]-Padé approximant, and a [1/1] approximant was used to calculate the functions γ_t and γ_φ.

The stable fixed points of renormalization-group transformation, the β-function derivatives at the fixed point, and the critical indices for $1.5 \le a \le 1.9$ are given in the table. For $0 < a < 1.5$, an unstable Gaussian fixed point $v^* = 0$ only exists. This result is consistent with the ε-expansion predictions [1–3]. The absence of a sta-

ble fixed point is evidence that the second-order phase transition changes to the first-order transition [8].

An analysis of the critical indices shows that ν decreases with decreasing a; i.e., the growth rate of the correlation radius decreases as the critical point is approached.

Thus, the increase in long-rage effects in the three-dimensional Ising systems first decelerates the growth rate of the correlation radius in the critical region, after which the kind of phase transition changes at $a < 3/2$.

REFERENCES

1. M. E. Fisher, S.-K. Ma, and B. G. Nickel, Phys. Rev. Lett. **29**, 917 (1972).
2. J. Honkonen, J. Phys. A **23**, 825 (1990).
3. E. Luijten and H. Mebingfeld, Phys. Rev. Lett. **86**, 5305 (2001).
4. E. Bayong and H. T. Diep, Phys. Rev. B **59**, 11919 (1999).
5. E. Luijten, Phys. Rev. E **60**, 7558 (1999).
6. E. Luijten and H. W. J. Blooöte, Phys. Rev. B **56**, 8945 (1997).
7. J. Zinn-Justin, *Quantum Field Theory and Critical Phenomena* (Clarendon Press, Oxford, 1989).
8. Yu. A. Izyumov and V. N. Syromyatnikov, *Phase Transitions and Crystal Symmetry* (Nauka, Moscow, 1984).

Translated by V. Sakun

JETP Letters, Vol. 77, No. 2, 2003, pp. 115–117. Translated from Pis'ma v Zhurnal Éksperimental'noĭ i Teoreticheskoĭ Fiziki, Vol. 77, No. 2, 2003, pp. 121–123.

Detection of Infrasound from the Vitim Bolide on September 24, 2002

O. I. Shumilov*, E. A. Kasatkina*, E. D. Tereshchenko*, S. N. Kulichkov, and A. N. Vasil'ev***

** Polar Geophysical Institute, Kola Science Center, Russian Academy of Sciences, Apatity, Murmansk region, 184209 Russia*

*** Obukhov Institute of Atmospheric Physics, Russian Academy of Sciences, Pyzhevskiĭ per. 3, Moscow, 109017 Russia*

Received December 24, 2002

An infrasonic signal from an atmospheric bolide explosion was detected on September 24, 2002 near the Vitim river, Irkutsk region (57.9 N, 112.9 E). The signal was detected by three spatially separated microbarographs of the Polar Geophysical Institute (PGI), Kola Science Center, Russian Academy of Sciences, Apatity (67.6 N, 33 E) at a distance of 4000 km from the source. The acoustic-gravity signal from a falling meteorite at high latitudes was detected at such a distance for the first time in Russia. © *2003 MAIK "Nauka/Interperiodica".*

PACS numbers: 94.10.Jd; 92.60.Dj; 96.50.Kr

The generation and propagation of acoustic-gravity waves induced by meteoric bodies invading the atmosphere were studied in [1–5]. According to satellite data, large bodies 1–10 m in size, which are responsible for the bolide phenomenon, appear no more frequently than once a year [6]. Meteorites such as the Tunguska meteorite collide with the Earth no more frequently than once per one thousand years [6]. The character of wave radiation depends on the energy release to the atmosphere and on the parameters of the atmosphere. Therefore, the mass of a meteoric body can be estimated from variations in atmospheric pressure recorded by microbarographs [1, 2], and a conclusion about the existence of a waveguide in the atmosphere can be drawn. The formation of atmospheric waveguides at various altitudes determined by the temperature and wind-velocity gradients [7], as well as the superreflection effect [8], allow the infrasonic signal to cover hundreds and thousands of kilometers from a source.

We report here the results of our preliminary analysis of the infrasonic signal from the Vitim bolide, which was detected on September 24, 2002 by microbarographs of the PGI at a distance of 4000 km from the source. According to the information from the Institute of Solar–Terrestrial Physics, Siberian Division, Russian Academy of Sciences, a large space object (presumably a meteorite) fell near the Vitim river at a distance of several tens of kilometers from Bodaibo, Irkutsk region. The fall of the space body was preceded by an explosion at an altitude of 30 km, which was detected by U.S. satellites at 16:49 UT on September 24, 2002. According to eyewitnesses, a large shooting star drew a line through the night sky and collapsed on the hills. A blinding flash illuminated the taiga for several instants with a bright light resembling electric light, and then such a strong explosion thundered that ground shaking similar to that from an earthquake was felt over several kilometers from the fall point.

The table presents some U.S. satellite data on bolides (coordinates and radiation energies) since 1991 [6]. For most bolides, an infrasonic signal was detected by a global network of infrasound-monitoring stations [5, 6]. As is seen, the Vitim bolide is among the largest recently detected bolides.

Energy and coordinates of points where some bolides entered the atmosphere according to U.S. satellites [6]

Date	UT	Coordinates	E, J
7.05.1991	23:04	50 N, 15 W	5×10^{10}
15.06.1994	00:03	46 N, 73 W	1.3×10^{10}
9.10.1997	18:47	32 N, 106 W	1.9×10^{11}
16.8.1999	05:18	35 N, 107 W	3.8×10^{10}
18.01.2000	16:43	60 N, 135 W	1.1×10^{12}
18.02.2000	09:26	1 S, 109 E	3.6×10^{12}
6.05.2000	11:54	50 N, 18 E	2.5×10^{10}
25.08.2000	01:12	15 N, 106 W	1.4×10^{12}
23.04.2001	06:12	28 N, 134 W	4.6×10^{12}
9.03.2002	01:20	7 N, 147 W	2.2×10^{11}
6.06.2002	04:28	34 N, 21 E	3.8×10^{12}
25.07.2002	15:58	29 S, 47 E	2.5×10^{11}
24.09.2002	16:49	57.91 N, 112.9 E	8.6×10^{11}

0021-3640/03/7702-0115$24.00 © 2003 MAIK "Nauka/Interperiodica"

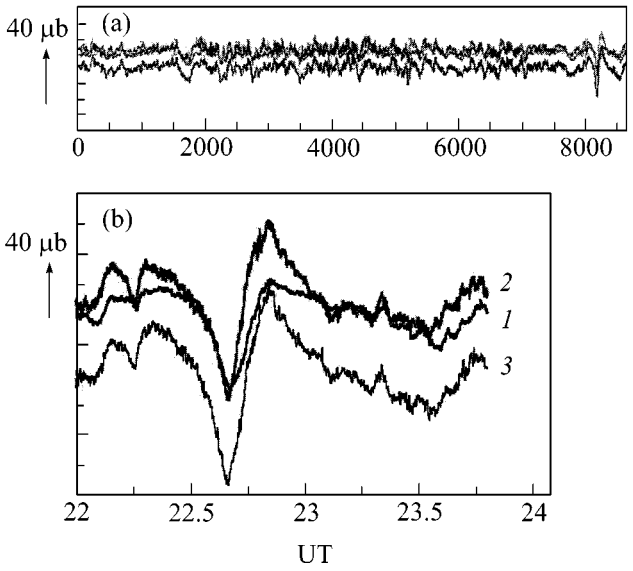

Fig. 1. Records of microbarographs at the Apatity observatory for (a) the entire day of September 24, 2002 and (b) the 22:00–24:00 UT interval.

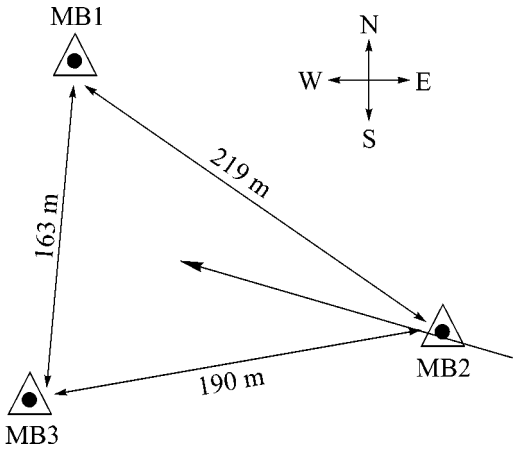

Fig. 2. Scheme of the arrangement of microbarographs (MB1–MB3).

The infrasonic signal was detected by three spatially separated microbarographs of the PGI high-altitude measuring complex [9]. In addition to these microbarographs for measuring variations in atmospheric pressure in the frequency range from 0.0001 to 1 Hz, the complex includes the electric-field sensors and an instrument for measuring the air conductivity. The computer data-acquisition system can gain information with a polling frequency of five times per second.

Figure 1 shows the records of three microbarographs on September 24, 2002. It is clearly seen that all three detectors fixed the arrival of an infrasonic signal with the maximum amplitude $\Delta P \cong 45$ dyn/cm^2 at ~22:20 UT. This signal is clearly seen even against the background of continuously observed downstream waves associated with the neighboring Khibiny mountains [9].

Figure 2 shows the arrangement of three microbarographs. By the method of separated receivers, a horizontal-trace velocity of 247 m/s and a wave-arrival angle of 117° (measured from north) were determined from the measured differences between the signal arrival times. Using the time of signal arrival (~22:20 UT) and the distance from the source (~4000 km), one can estimate the average horizontal projection of signal-propagation velocity at $V = R/T = 209$ m/s. This value, together with the source azimuth, as calculated from geographical coordinates (113°), agree with the value of horizontal trace and the signal arrival direction, which were calculated from the data of three microbarographs. Such velocities are characteristic for the signal propagation in the thermosphere (at altitudes > 85 km) [7], which can be due to the west circulation of air masses at stratospheric heights at the given latitude in this season.

The bolide mass was estimated using the relationships between the energy E_0 of a pulsed source and the disturbed pressure ΔP detected at the distance R from the radiation source [1, 10]. According to [1],

$$\Delta P \approx \frac{(\gamma-1)E_0(R-ct)\exp\left(\dfrac{-z/2H-(ct-R)^2}{R_0^2\sin^2\theta + L^2\cos^2\theta}\right)}{2\pi^{3/2}R(R_0^2\sin^2\theta + L^2\cos^2\theta)^{1/2}}. \quad (1)$$

Here, c is the speed of sound, H scales the altitude of uniform atmosphere, L is the length of the meteoric trace, $\gamma = 1.4$ is the specific heat ratio, θ is the angle between the direction of infrasonic signal and the axis of meteoric trace,

$$R_0 = M_0^{1/3}V_0^2/2(2gHQ_0)1/2\rho_0^{1/3} \quad (2)$$

is the average radius of the meteoric trace, where M_0 and V_0 (11.2 km/s < V_0 < 73.2 km/s) are the meteoric mass and velocity, respectively, and $Q_0 = 8 \times 10^{10}$ erg/g is the latent evaporation heat [1].

Assuming that the detected infrasonic signal propagates in the plane perpendicular to the axis of meteoric trace ($\theta = \pi/2$), we find from Eq. (1) that [1]

$$\Delta P \approx (\gamma-1)E_0/2\pi^{3/2}RR_0^2. \quad (3)$$

Substituting $\Delta P = 45$ dyn/cm^2 and the average velocity $V_0 = 30$ km/s into Eq. (3), we obtain $M_0 = 6$ ton. This value is a lower limit, because Eq. (3) was derived for a signal propagating without reflections [1]. In the case under consideration, the propagating infrasonic signal undergoes multiple reflections from the waveguide walls [7].

Reed [10] proposed the following empirical relation between the explosion energy E_0 (kilotons of TNT;

1 kiloton of TNT = 4.185×10^{12} J) and the disturbed pressure ΔP (kPa) at distance R (km):

$$\Delta P = 11.8 E_0^{0.4} R^{-1.2}. \quad (4)$$

This gives $M_0 = 38$ and 1 ton, respectively, for limiting velocities $V_0 = 11.2$ and 73.2 km/s.

The table presents the radiation energies of the bolide, which were obtained from the satellite optical data. The optical radiation energy comprises from 5 to 10% of the total energy of bolide [6]. In our case, the optical energy is $E = 8.6 \times 10^{11}$ J. Assuming that this value is equal to 10% of the total energy E_0, we obtain the bolide mass $M_0 = 142$ and 3.5 ton for two limiting velocities, respectively. These values are in satisfactory agreement with the above estimates obtained from the amplitude of the infrasonic signal.

The analysis of this event corroborates the previous conclusion that bright heavy bolides can be responsible for high-power pulsed radiation of acoustic-gravity waves in the Earth's atmosphere, which can be detected by microbarographs at a distance of several thousands of kilometers.

This work was supported by the Russian Foundation for Basic Research (project no. 01-05-64850) and INTAS (grant no. 31008).

REFERENCES

1. G. S. Golitsyn, G. I. Grigor'ev, and V. P. Dokuchaev, Izv. Akad. Nauk SSSR, Fiz. Atmos. Okeana **13**, 926 (1977).
2. D. O. ReVelle, J. Geophys. Res. **81**, 1217 (1976).
3. B. A. McIntosh, M. D. Watson, and D. O. ReVelle, Can. J. Phys. **54**, 655 (1976).
4. L. G. Evers and H. W. Haak, Geophys. Res. Lett. **28**, 41 (2001).
5. P. G. Brown, D. O. ReVelle, E. Tagliaferri, and A. R. Hildebrand, Meteoritics Planet. Sci. **37**, 661 (2002).
6. P. Brown, R. E. Spalding, D. O. ReVelle, *et al.*, Nature **420**, 294 (2002).
7. S. N. Kulichkov, Izv. Ross. Akad. Nauk, Fiz. Atmos. Okeana **28**, 339 (1992).
8. N. N. Romanova and I. G. Yakushkin, Izv. Ross. Akad. Nauk, Fiz. Atmos. Okeana **31**, 163 (1995).
9. O. I. Shumilov, E. A. Kasatkina, E. D. Tereshchenko, *et al.*, Izv. Ross. Akad. Nauk, Fiz. Atmos. Okeana **38**, 471 (2002).
10. J. W. Reed, J. Geophys. Res. **77**, 1623 (1972).

Translated by R. Tyapaev

JETP Letters, Vol. 77, No. 2, 2003, p. 118.

ERRATA

Erratum: Critical Current in a System of Two Superconductors Connected by a Short Small-Diameter Normal Metal Bridge (Pis'ma Zh. Éksp. Teor. Fiz. 76, 380 (2002) [JETP Lett. 76, 321 (2002)]

Yu. N. Ovchinnikov and A. I. Larkin

PACS numbers: 74.50.+r; 74.25.Sv

In our article published in vol. 76, no. 5, pp 321–325, we studied current states in the SNS junctions. The solutions described by Eq. (8) in the low-frequency limit do not agree with the high-frequency results known from perturbation theory. We have concluded that the states described by our solution do not exist and that the only correct solution is that found by I. Kulik and A. Omel'yanchuk.

We are grateful to M. Feĭgel'man and Ya. Fominov for pinpointing this fact.

Yu. Ovchinnikov and A. Larkin

0021-3640/02/7702-0118$24.00

JETP Letters, Vol. 77, No. 2, 2003, p. 119.

ERRATA

Erratum: Polariton Dispersion of Periodic Quantum Well Structures (Pis'ma Zh. Éksp. Teor. Fiz. 76, 739 (2002) [JETP Lett. 76, 637 (2002)]

A. V. Mintsev, L. V. Butov, C. Ell, S. Mosor, G. Khitrova, and H. M. Gibbs

PACS numbers: 73.21.Fg; 71.36.+c; 73.20.Mf

In the article of A.V. Mintsev, L.V. Butov, C. Ell, S. Mosor, G. Khitrova, and H.M. Gibbs published in vol. 76, no. 10, pp. 637–640, Figures 1 and 2 should be reversed.

JETP Letters, Vol. 77, No. 2, 2003, pp. 53–57. From Pis'ma v Zhurnal Éksperimental'noĭ i Teoreticheskoĭ Fiziki, Vol. 77, No. 2, 2003, pp. 59–63.

Commutativity Equations and Dressing Transformations¶

A. Losev[1] and I. Polyubin[1, 2]

[1] *Institute of Theoretical and Experimental Physics, Moscow, 117259 Russia*

[2] *Landau Institute for Theoretical Physics, Moscow, 117334 Russia*

Received December 19, 2002

We study dressing transformations that generate all solutions to commutativity equations and, after picking up special coordinates, all solutions to WDVV equations. We conjecture that the homological tensor product of solutions to the commutativity equations corresponds to the tensor product of matrices of the dressing transformation and check this in the first nontrivial case. © *2003 MAIK "Nauka/Interperiodica"*.

PACS numbers: 11.25.Hf

The main problem in our current understanding of the theory of quantum gravity is the uniqueness of M-theory. In order to understand it, we need to find and study much simpler and tractable models that have common features with M-theory. That is why so much attention is spent on so-called topological strings [1–12]. Moreover, recent studies of superstrings made by Berkovits [13] indicate that probably even superstrings themselves could be considered somehow as a rather special case of topological strings.

From the very first days of topological strings, it was found that their tree level amplitudes satisfy remarkable quadratic equations (WDVV or associativity equations). Moreover, it turns out that, in many known examples, higher loop amplitudes can be expressed in terms of the tree level amplitudes.

All this leads to the following scheme of study of topological theories. First, we classify solutions to the WDVV equations. Second, we look for conditions on solutions to the WDVV equations that correspond to topological strings.

In this paper, we give a classification of all solutions of the WDVV equations based on their relations to solutions of the commutativity equations [14–17] on $GL(\dim W)$-valued functions in the base space S.

In particular, we will classify all solutions to the commutativity equations in terms of the maximal commutative subgroups of $GL(\dim W)$ and dressing transformation matrices, which are matrices whose elements are polynomials of one variable.

Moreover, the parametrization of solutions to the commutativity equations in terms of dressing matrices looks rather natural when we study the tensor product of solutions in this parametrization.

Indeed, recall that solutions to the commutativity equations can be obtained from supersymmetric quantum mechanics. Therefore, one can define the tensor product by considering the tensor product of quantum mechanics—the total Hilbert space is a product of Hilbert spaces, while the total supercharges are sums of supercharges. As was shown in [16], this tensor product is equal to the homological tensor product on solutions to commutativity equations. Really, each solution corresponds to a factorizable map to cohomologies of the moduli space $\bar{L}_n$, and a tensor product can be obtained by taking the product in cohomologies of the moduli spaces.

In this paper, we conjecture that the above-mentioned tensor product corresponds just to the tensor product of maximal commuting subalgebras and to the tensor product of dressing transformation matrices. We check this conjecture in the first nontrivial case and find that it actually works.

In [18], we studied the procedure of reconstruction of solutions to the WDVV equations from solutions to the commutativity equation and found that the homological tensor product was compatible with the reconstruction procedure. Therefore, we managed not only to classify solutions to WDVV but also to find a parametrization in which the tensor product on such solutions takes a rather simple form.

All this implies that the theory of the WDVV equation and the theory of its quantization in the spirit of [19, 20] should be rewritten in terms of a dressing matrix. We should mention that a similar construction for the semisimple case was given by [21], but from our presentation it should be clear that the semisimplicity condition is an auxiliary assumption.

Commutativity equations [14, 17–19] are the set of equations on $\tau(t)$—a $GL(\dim W)$-valued formal series in $t_1, \ldots, t_n$ (later, we would like to treat $t_1, \ldots, t_n$ as a set of coordinates on an n-dimensional space S).

If we choose a basis e_a in the vector space W, then we can consider $\tau(t)$ as a matrix $\tau_a^b(t)$ taking values in the formal series in $t_1, \ldots, t_n$.

¶ This article was submitted by the authors in English.

The commutativity equations have the form

$$d\tau \wedge d\tau = 0 \tag{1}$$

or, in components,

$$\frac{\partial \tau_a^b(t)}{\partial t_i}\frac{\partial \tau_b^c(t)}{\partial t_j} = \frac{\partial \tau_a^b(t)}{\partial t_j}\frac{\partial \tau_b^c(t)}{\partial t_i}. \tag{2}$$

We will use the following properties of the commutativity equations:

(A) Suppose that we have a map f: $S' \subset S$,

$$t_i = f_i(t'). \tag{3}$$

Then $f^*\tau$ is an induced solution to the commutativity equations, where

$$(f^*\tau)(t') = \tau(f_1(t'), \ldots, f_n(t')). \tag{4}$$

(B) The commutativity equations are equivalent to the flat connections in the trivial bundle W over S with the spectral parameter z; namely, if

$$\nabla(z) = d + z^{-1}A \tag{5}$$

then from

$$(\nabla(z))^2 = 0, \tag{6}$$

it follows that (from the terms linear in z^{-1})

$$A = d\tau \tag{7}$$

and that (from the terms quadratic in z^{-1})

$$A^2 = 0, \tag{8}$$

which is the commutativity equations.

Now we begin our description of the classification of solutions to the commutativity equations.

Due to property (A), it is reasonable to consider only the primitive solution, i.e., solutions with $\dim W = \dim S$ and such that these solutions cannot be induced from the solution with $\dim S < \dim W$.

In the classification of primitive solutions, we use the dressing technique (we are grateful to V. Fock for discussion on this subject), which works as follows.

We start with the maximal commutative subalgebra in End(W), which has $\dim W$ generators ϕ_i. It corresponds to the simple solution of the commutativity equations

$$\tau = \phi = \sum_{i=1}^{\dim} \phi_i t_i. \tag{9}$$

This corresponds to the connection

$$d + z^{-1}\sum_i \phi_i dt_i = \exp(-z^{-1}\phi)d\exp(z^{-1}\phi). \tag{10}$$

Consider an arbitrary matrix

$$U(z) = \exp\left(\sum_{k=1}^{\infty} z^k V_k\right) \tag{11}$$

that is a holomorphic function of z, and consider the factorization problem

$$\exp(z^{-1}\phi(r))U(z) = M(t, z)N(t, z^{-1}), \tag{12}$$

such that $N(t, 0) = 1$. Then,

$$N(t, z^{-1}) = M(t, z)^{-1}\exp(z^{-1}\phi(t))U(z), \tag{13}$$

and thus

$$\begin{aligned} &N(t, z^{-1})dN^{-1}(t, z^{-1}) \\ &\quad = M(t, z)^{-1}(d + z^{-1}d\phi)M(t, z). \end{aligned} \tag{14}$$

The left-hand side of the above equation has the form $d + z^{-1}A_1(z^{-1}, t)$, while the right-hand side is obviously $d + z^{-1}A_2(z, t)$. Thus,

$$A_1(z^{-1}, t) = A_2(z, t) = A(t) \tag{15}$$

and (from the expression for A_2) it follows that

$$A(t) = M(0, t)^{-1}\phi_i M(0, t)dt_i \tag{16}$$

and that $A(t) = d\tau$, and that this τ solves the commutativity equations.

In order to get explicit expressions for $M(0, t)$, consider the level zero representation of the $GL(\dim W)$ current algebra. Consider the vacuum $|a\rangle$ and covacuum $\langle b|$, which are annihilated by positive and negative modes of currents and which form fundamental representations for the zero modes of currents. Then, $M(0, t)$ is a tau function:

$$M(0, t)_a^b = \langle b|\widehat{\exp(z^{-1}\phi)}\,\widehat{U(z)}|a\rangle, \tag{17}$$

where $\widehat{K(z, z^{-1})}$ denotes the operator corresponding to the matrix K in the level zero representation.

Below, we will present some explicit formulas for the first terms in the expansion of τ in terms of dressing transformation parameters V.

The log of the dressing matrix $M(0, t)$ up to the third order in t is equal to

$$\begin{aligned} \log M_0(t) &= V_1' + \frac{1}{2}V_2'' + \frac{1}{2!2!}[V_1'', V_1] \\ &+ \frac{1}{3!2!2!}[V_1'', [V_1', V_1]] + \frac{1}{3!2!2!}[[V_1'', V_1'], V_1] \\ &+ \frac{1}{3!3!}[[V_1''', V_1], V_1] + \frac{1}{3!2!}[V_2''', V_1] \\ &+ \frac{1}{3!2!}[V_1''', V_2] + \frac{1}{2!2!}[V_1'', V_2] + \frac{1}{3!}V_3''' + O(t^4). \end{aligned} \tag{18}$$

The expression for τ up to the fourth order in t is as follows:

$$\begin{aligned}\tau(t) &= \phi + \frac{1}{2!}V_1'' + \frac{1}{3!2!}[V_1''', V_1] + \frac{1}{3!}V_2''' \\ &+ \frac{1}{2!2!}[V_1'', V_1'] + \frac{1}{3!2!2!}[V_1'', [V_1'', V_1]] \\ &+ \frac{1}{3!3!}[[V_1''', V_1'], V_1] + \frac{1}{3!3!}[[V_1''', V_1], V_1'] \\ &+ \frac{1}{4!3!}[[V_1'''', V_1], V_1] + \frac{1}{3!2!}[[V_1'', V_1'], V_1'] \\ &+ \frac{1}{4!2!}[V_2'''', V_1] + \frac{1}{4!2!}[V_1'''', V_2] + \frac{1}{3!2!}[V_2''', V_1'] \\ &+ \frac{1}{3!2!}[V_1''', V_2'] + \frac{1}{2!2!2!}[V_1'', V_2''] + \frac{1}{4!}V_3'''' + O(t^5),\end{aligned} \tag{19}$$

where $V_i' = [\phi, V_i]$, $V_i'' = [\phi, [\phi, V_i]]$, $V''' = [\phi, [\phi, [\phi, V_i]]]$, etc.

Explicit formulas for solutions to commutativity equations suggest that one can obtain a universal formula as a series in the Lie algebra generated by matrices V_k and ϕ_i. Conjecturally, the terms in this series are classified by three-valent rooted trees, and the combinatorial coefficient is something like an inverse factorial for the number of ϕ times inverse factorial for the number of V's. This suggests that the commutativity equation can be proved directly through graphical reasoning without appealing to dressing transformations. We leave this problem for future work.

One can show that the general solution can be induced from the solution obtained by the dressing transformation.

After classification of the solutions to the commutativity equations, we describe the procedure of reconstruction of solutions to the associativity (WDVV) equations.

We begin with the acyclic associativity equations.

The associativity equations are not the only equations that one can associate with the Deligne–Mumford compactification of the moduli space of marked points on the sphere. The reason for this is that one can mark all points as "in" points or "out" points. Consider a subspace or markings that contain one "out" point, with all other points marked as "in" points. When the sphere degenerates into two spheres, it produces two points—one "in" point (on the component that contains the "out" point) and one "out" point (on the component that contained only "in" points). If we associate vector spaces with "in" points and dual vector spaces with "out" points, we can postulate that degeneration is accompanied by the canonical pairing between the vector space associated to the "in" point and its dual associated to the "out" point. Reasoning as in the standard derivation of associativity equations from the Keel relations, we see that now the generating function for the correlators is a vector field $v(T)$ on the base space W, equipped with the special coordinates T, such that its second derivatives form structure constants of associative algebra. This is what we will call the acyclic associativity equation:

$$\frac{\partial^2 v^e(T)}{\partial T^a \partial T^b}\frac{\partial^2 v^d(T)}{\partial T^e \partial T^c} = \frac{\partial^2 v^e(T)}{\partial T^a \partial T^c}\frac{\partial^2 v^d(T)}{\partial T^e \partial T^b}. \tag{20}$$

Solutions to the acyclic associativity equations can be obtained from the solutions to commutativity equations if we suppose that the latter have a primitive element—a vector $h \in W$, such that the operator $d\tau(h)$ considered as an operator from the tangent space to the base S to the space W is nondegenerate.

The construction goes as follows (see [15, 18]). Consider a map from S to W that sends the point on V with coordinates t to the point on W with coordinates $T^b(t)$ given by:

$$T^b(t) = \tau_a^b(t)h^a. \tag{21}$$

Consider the inverse map f from W to S; it expresses t^i as a function of T^a:

$$t^i = f^i(T; h); \quad T^b = \tau_a^b(f(T, h))h^a. \tag{22}$$

Then one can show that there exists a vector field $v^a(T)$ such that

$$f^*(\tau)_a^b = \partial v^b/\partial T^a \tag{23}$$

and this vector field solves the acyclic associativity equations.

The special feature of this choice of coordinates is that the coordinate in the direction of h enters v only linearly, namely,

$$h^a\frac{\partial^2 v^b}{\partial T^a \partial T^c} = \delta_b^c. \tag{24}$$

There are other choices of coordinates that still produce acyclic associativity equations; they are related to lifting to the action gravitational descendants and they will violate property (24). We will discuss this topic elsewhere.

By associativity equations (without an Euler vector field) we mean the following equations on a function $F(T)$ on the space W:

$$\begin{aligned}&\frac{\partial^3 F(T)}{\partial T^a \partial T^b \partial T^e}\eta^{ef}\frac{\partial^3 F(T)}{\partial T^f \partial T^c \partial T^d} \\ &= \frac{\partial^3 F(T)}{\partial T^a \partial T^c \partial T^e}\eta^{ef}\frac{\partial^3 F(T)}{\partial T^f \partial T^d \partial T^d},\end{aligned} \tag{25}$$

where η is a constant pairing on the space W.

Suppose that we have a solution to the acyclic associativity equations and there is a constant metric η such that

$$dT^b v^a \eta_{ab} = dF(T). \quad (26)$$

Then it is easy to show that $F(T)$ is a solution to the associativity equations. Moreover, if we introduce a special coordinate

$$T_0 = h^a T^b \eta_{ab} \quad (27)$$

then one can show that

$$\frac{\partial^3 F(T)}{\partial T_0 \partial T_a \partial T_b} = \eta_{ab}; \quad (28)$$

i.e., we get solutions to WDVV with the identity.

We call $\tau(t)$a symmetric (with respect to η) solution to the commutativity equations if $\tau^T = \tau$; i.e.,

$$\tau^b_a \eta_{bc} = \tau^b_c \eta_{ba}. \quad (29)$$

Suppose that the symmetric solution to the commutativity equations admits a primitive element h. Then the solution to the acyclic associativity equation will satisfy property (26), i.e., will lead to the solution to the associativity equations with identity.

Thus, in order to get solutions to the associativity equations, we need to study symmetric solutions to the commutativity equations. As one can show (and check using the manifest formula), we need to impose the following conditions on ϕ and V_k:

$$\phi^T = \phi, \quad V_k^T = (-1)^{k+1} V_k, \quad (30)$$

where symmetry is studied with respect to metric η.

We have already seen how useful the dressing transformation is in studying the commutativity equations and their ability to be promoted to WDVV equations. Now we will show that dressing transformation parametrization probably drastically simplifies the computation of the homological tensor product of solutions on the commutativity equations. Namely, we will compare two tensor products. In order to write explicit formulas, we need to introduce coefficients of the expansion of the solution to the commutativity equations in parameters t:

$$\tau(t) = \sum_n \sum_{i_1 \dots i_n} \tau_{i_1 \dots i_n} \frac{t_{i_1} \dots t_{i_n}}{n!}. \quad (31)$$

The first tensor product on solutions to the commutativity equations comes from the tensor products on commutative algebras and on matrices of the dressing transformations. Namely, if e_i is a basis in S_1 and $e_{i'}$ is a basis in S_2, then we take

$$e_I = e_{ii'} = e_i \otimes e_{i'} \quad (32)$$

to be a basis in $V^{1 \otimes 2} = V^1 \otimes \tilde{V}^2$. Thus, we have

$$\phi_I^{1 \otimes 2} = \phi_i \otimes \phi_{i'} \quad (33)$$

and

$$V_m^{1 \otimes 2} = 1 \otimes \tilde{V}_m + V_m \otimes 1. \quad (34)$$

The latter formula can be also rewritten in a form suggestive for the matrices of dressing transformations:

$$U^{1 \otimes 2}(z) = U(z) \otimes \tilde{U}(z), \quad (35)$$

where U and $\tilde{U}$ are the matrices of dressing transformations for the first and the second solutions to the commutativity equations.

The explicit formulas for the tensor product up to the third order (the formulas for the first two orders are rather simple) look as follows:

$$\tau_I^{1 \otimes 2} = \tau_i \otimes \tau_{i'}, \quad (36)$$

$$\tau_{IJ}^{1 \otimes 2} = \tau_i \tau_j \otimes \tau_{i'j'} + \tau_{ij} \otimes \tau_{i'} \tau_{j'}, \quad (37)$$

$$\begin{aligned}
\tau_{IJK}^{1 \otimes 2} &= \tau_{ijk} \otimes \phi_{i'} \phi_{j'} \phi_{k'} + \phi_i \phi_j \phi_k \otimes \tau_{i'j'k'} \\
&+ \frac{1}{2}(\tau_{ij} \phi_k \otimes \phi_{i'} \phi_{j'} [\phi_{k'}, \tilde{V}_1] - \phi_k \tau_{ij} \otimes [\phi_{k'}, \tilde{V}_1] \phi_{i'} \phi_{j'} \\
&+ \tau_{ik} \phi_j \otimes \phi_{i'} \phi_{k'} [\phi_{j'}, \tilde{V}_1] - \phi_j \tau_{ik} \otimes [\phi_{j'}, \tilde{V}_1] \phi_{i'} \phi_{k'} \\
&+ \phi_i \tau_{jk} \otimes \phi_{i'} [\phi_{j'} \phi_{k'}, \tilde{V}_1] - \tau_{ik} \phi_i \otimes [\phi_{j'} \phi_{k'}, \tilde{V}_1] \phi_{i'} \\
&+ \phi_i \phi_j [\phi_k, V_1] \otimes \tau_{i'j'} \phi_{k'} - [\phi_k, V_1] \phi_i \phi_j \otimes \phi_{k'} \tau_{i'j'} \\
&+ \phi_i \phi_k [\phi_j, V_1] \otimes \tau_{i'k'} \phi_{j'} - [\phi_j, V_1] \phi_i \phi_k \otimes \phi_{i'} \tau_{j'k'}, \\
&+ \phi_i [\phi_j \phi_k, V_1] \otimes \tau_{i'k'} - [\phi_j \phi_k, V_1] \otimes \phi_{i'} \tau_{j'k'} \phi_{i'}),
\end{aligned} \quad (38)$$

where $\tau_{ij} = [\phi_i, [\phi_j, V_1]]$.

The second product comes from the interpretation of the solutions to the commutativity equations as factorizable maps onto cohomologies of the moduli space $\bar{L}_n$ introduced in [12, 16–18].

Recall that $\bar{L}_n$ is the compactification of $C^{*,n}/C^*$; i.e., the moduli space of n points on C^* acted on by a multiplication by a nonzero complex number.

Namely, given a solution to the commutativity equation τ, one can construct an element h_n:

$$h_n \in H^*(\bar{L}_n) \otimes S^{*\otimes n} \otimes \mathrm{End}(W) \quad (39)$$

and

$$h_{n,1 \otimes 2} = h_{n,1} h_{n,2}, \quad (40)$$

where the product on the r.h.s. of (40) is the product in cohomologies and a tensor product in $S^{*\otimes n} \otimes \mathrm{End}(W)$ (note that $S_{1 \otimes 2} = S_1 \otimes S_2$ and $W_{1 \otimes 2} = W_1 \otimes W_2$).

In the explicit computation of the product, we use the fact that

$$h_{n,1} \cap h_{n,2}(\bar{L}_n) = \sum_{A,B} h_{n,1}(C_A) h_{n,2}(C_B) N^{AB} \qquad (41)$$

where C_A stands for the basis of cycles in homologies of $\bar{L}_n$ and N is the inverse to their intersection matrix.

The equivalence of the tensor products computed on $\bar{L}_1$ and $\bar{L}_2$ is obvious and, thus, it is not quite representative. Here we will compute and compare two tensor products on $\bar{L}_3$ (i.e., for the term that is of third order in t in the expansion of $\tau(t)$).

In particular (see [18] for details), we obtained the following result for $\bar{L}_3$.

In this case, the intersection matrix of 2-cycles has rank 4. Let $(x, y)(z)$ correspond to the cycle where the sphere degenerates into two spheres, with two points with labels x, y on the first sphere and a point with label z on the second.

Let j, k, l denote the labels of the marked points.

In the basis of cycles

$$\begin{gathered}(jl)(k) + (j)(kl) \\ + (jk)(l);\ (jk)(l);\ (jl)(k);\ (kl)(j)\end{gathered} \qquad (42)$$

the intersection matrix is diagonal: diag(1; –1; –1; –1). Therefore,

$$\begin{aligned}\tau_{IJK}^{Hom1\otimes 2} &= \tau_{jkl} \otimes \phi_{j'}\phi_{k'}\phi_{l'} + \phi_j\phi_k\phi_l \otimes \tau_{j'k'l'} \\ &+ \tau_{kl}\phi_j \otimes \tau_{k'l'}\phi_{j'} + \tau_{kl}\phi_j \otimes \phi_{l'}\tau_{j'k'} \\ &+ \tau_{kl}\phi_j \otimes \phi_{k'}\tau_{j'l'} + \phi_k\tau_{jl} \otimes \tau_{k'l'}\phi_{j'} \\ &+ \phi_k\tau_{jl} \otimes \phi_{l'}\tau_{j'k'} + \phi_l\tau_{jk} \otimes \tau_{k'l'}\phi_{j'} \\ &+ \phi_l\tau_{jk} \otimes \phi_{k'}\tau_{j'l'} - \phi_j\tau_{kl} \otimes \phi_{j'}\tau_{k'l'}.\end{aligned} \qquad (43)$$

By comparing formulas (38) and (43), one can show that they define the same tensor product structure on $\bar{L}_3$.

Thus, we have seen that the dressing matrix parametrization of the solutions to the commutativity equations is quite effective. The next question is to find a representation for the higher loop amplitudes [19, 20] in terms of dressing matrices.

We are especially grateful to V. Fock for explanation of the dressing transformations technique.

The work of A.L. was partially supported by INTAS (grant no. 99-590), the Russian Foundation for Basic Research (project no. 00-02-16530), and the Program of Support for Scientific Schools (grant no. 00-15-96557).

The work of I.P. was partially supported by INTAS (grant no. 00-00055), the CRDF (grant no. RP1-2254), the Russian Foundation for Basic Research (project no. 00-02-16477), and the Program of Support for Scientific Schools (grant no. 00-15-965779).

REFERENCES

1. E. Witten, Nucl. Phys. B **340**, 281 (1990).
2. R. Dijkgraaf and E. Witten, Nucl. Phys. B **342**, 486 (1990).
3. E. Verlinde and H. Verlinde, Nucl. Phys. B **348**, 457 (1991).
4. R. Dijkgraaf, E. Verlinde, and H. Verlinde, in *Proceedings of the Trieste Spring School on String Theory and Quantum Gravity, 1990*, Ed. by M. Green *et al.* (World Sci., Singapore, 1991).
5. E. Witten, hep-th/9207094.
6. A. Losev, Theor. Math. Phys. **95**, 595 (1993).
7. T. Eguchi, H. Kanno, Y. Yamada, *et al.*, Phys. Lett. B **305**, 235 (1993).
8. M. Kontsevich and Yu. Manin, Commun. Math. Phys. **164**, 525 (1994).
9. B. Dubrovin, hep-th/9407018; Lect. Notes Math. **1620**, 120 (1996).
10. M. Bershadsky, S. Cecotti, H. Ooguri, and C. Vafa, Commun. Math. Phys. **165**, 311 (1994).
11. A. Losev and I. Polyubin, Int. J. Mod. Phys. A **10**, 4161 (1995).
12. M. Kontsevich and Yu. Manin, with appendix by Kaufmann, q-alg/9502009.
13. N. Berkovits, J. High Energy Phys. **0004**, 018 (2000).
14. S. Cecotti and C. Vafa, Nucl. Phys. B **367**, 359 (1991).
15. A. Losev, in *Proceedings of Taniguchi Conference on Theory of Primitive Form and Topological Field Theory*; hep-th/9801179.
16. A. Losev, Preprint No. ITEP-TH-84/98, ITÉF (Inst. of Theoretical and Experimental Physics, Moscow, 1998); Preprint LPTHE-61/98 (1998).
17. A. Losev and Yu. Manin, Mich. Math. J. **48**, 443 (2000).
18. A. Losev and I. Polyubin, Pis'ma Zh. Éksp. Teor. Fiz. **73**, 59 (2001) [JETP Lett. **73**, 53 (2001)].
19. A. Givental, math@xxx.lanl.gov, AG/0008067.
20. B. Dubrovin and Y. Zhang, math@xxx.lanl.gov, DG/0108160.
21. H. Aratyn and J. Van de Leur, in *Talk on 15th Euroconference on Nonlinear Evolution Equations and Dynamical Systems NEEDS 2001, Cambridge, England, 2001*; hep-th/0111243.

JETP Letters, Vol. 77, No. 2, 2003, pp. 58–62. From Pis'ma v Zhurnal Éksperimental'noĭ i Teoreticheskoĭ Fiziki, Vol. 77, No. 2, 2003, pp. 64–67.

Spectroscopy of Baryons Containing Two Heavy Quarks in Nonperturbative Quark Dynamics¶

I. M. Narodetskii, A. N. Plekhanov, and A. I. Veselov

Institute of Theoretical and Experimental Physics, Moscow, 117218 Russia

Received December 24, 2002

We have studied three quark systems in an effective Hamiltonian approach in QCD. With only two parameters, namely, the string tension $\sigma = 0.15$ GeV^2 and the strong coupling constant $\alpha_s = 0.39$, we obtain a good description of the ground state light and heavy baryons. The predictions of masses of the doubly heavy baryons not yet discovered are also given. In particular, a mass of 3637 MeV for the lightest *ccu* baryon is found by employing the hyperspherical formalism to the three-quark confining potential with the string junction. © *2003 MAIK "Nauka/Interperiodica".*

PACS numbers: 12.38.Lg; 14.20.-c

The discovery of the B_c meson [1] demonstrates that new sectors of hadron physics are becoming accessible to experiment. In particular, the existence of doubly heavy baryons is a natural consequence of the quark model, and it would be surprising if they did not exist. Data from the BaBar and Belle collaborations at the SLAG and KEK B-factories would be good places to look for doubly charmed baryons. Recently, the SELEX, the charm hadroproduction experiment at Fermilab, reported a narrow state at 3519 ± 1 MeV decaying into $\Lambda_c^+ K^- \pi^+$, consistent with the weak decay of the doubly charged baryon Ξ_{cc}^+ [2]. The SELEX result was recently critically discussed in [3]. Whether or not the state that SELEX reports turns out to be the first observation of doubly charmed baryons, studying their properties is important for a full understanding of the strong interaction between quarks.

Estimates for the masses and spectra of baryons containing two or more heavy quarks have been considered by many authors [4]. The purpose of this letter is to present a consistent treatment of the masses and wave functions of the light, heavy, and doubly heavy baryons obtained in a simple approximation within nonperturbative QCD. In [5], starting from the QCD Lagrangian and assuming the minimal area for the asymptotics of the Wilson loop, the Hamiltonian of the $3q$ system in the rest frame was derived. The methodology of the approach has been reviewed recently [6]. By using this approach and the hypercentral approximation [7], we calculate the ground state energies and wave functions of the doubly heavy baryons as three-quark systems, with the three-body confinement force. As a by-product, we also report the masses and wave functions for light and heavy baryons.

From an experimental point of view, a detailed discussion of the excited QQ'q states is probably premature. Therefore, we consider ground state baryons without radial and orbital excitations, in which case tensor and spin–orbit forces do not contribute perturbatively. Then only the spin–spin interaction survives in the perturbative approximation. The effective Hamiltonian (EH) has the form [6]

$$H = \sum_{i=1}^{3}\left(\frac{m_i^{(0)2}}{2m_i} + \frac{m_i}{2}\right) + H_0 + V, \tag{1}$$

where H_0 is the nonrelativistic kinetic energy operator, V is the sum of the perturbative one-gluon exchange potentials V_c,

$$V_c = -\frac{2}{3}\alpha_s \sum_{i<j}\frac{1}{r_{ij}}, \tag{2}$$

and the string potential

$$V_{\text{string}}(\mathbf{r}_1, \mathbf{r}_2, \mathbf{r}_3) = \sigma l_{\min}, \tag{3}$$

where $l_{\min}$ is the sum of the three distances $|\mathbf{r}_i|$ from the string junction point. In contrast to the standard approach of the constituent quark model, the dynamical masses m_i are no longer free parameters. They are expressed in terms of the running masses $m_i^{(0)}(Q^2)$ defined at the appropriate hadronic scale of Q^2 from the condition of the minimum of the baryon mass $M_B^{(0)}$ as function of m_i:

$$\frac{\partial M_B^{(0)}(m_i)}{\partial m_i} = 0,$$
$$M_B^{(0)} = \sum_{i=1}^{3}\left(\frac{m_i^{(0)2}}{2m_i} + \frac{m_i}{2}\right) + E_0(m_1, m_2, m_3), \tag{4}$$

¶This article was submitted by the authors in English.

0021-3640/03/7702-0058$24.00

E_0 being an eigenvalue of the operator $H_0 + V$. Technically, this has been done using the einbein (auxiliary fields) approach, which has proven to be rather accurate in various calculations for relativistic systems. Einbeins are treated as c number variational parameters: the eigenvalues of the EH are minimized with respect to einbeins to obtain the physical spectrum. Such a procedure provides a reasonable accuracy for meson ground states [8].

The physical mass M_B of a baryon is [9]

$$M_B = M_B^{(0)} + C, \quad C = -\frac{2\sigma}{\pi}\sum_i \frac{\eta_i}{m_i}, \tag{5}$$

where the constant C has the meaning of the quark self-energy. The values of η_i are taken from [9]. They are 1, 0.88, 0.234, and 0.052 for q, s, c, and b quarks, respectively.

The EH is solved using the hyperspherical approach adequate for confining potentials. The baryon wave function depends on the three-body Jacobi coordinates

$$\begin{aligned}\boldsymbol{\rho}_{ij} &= \sqrt{\frac{\mu_{ij}}{\mu}}(\mathbf{r}_i - \mathbf{r}_j),\\ \boldsymbol{\lambda}_{ij} &= \sqrt{\frac{\mu_{ij,k}}{\mu}}\left(\frac{m_i\mathbf{r}_i + m_j\mathbf{r}_j}{m_i + m_j} - \mathbf{r}_k\right)\end{aligned} \tag{6}$$

(i, j, k cyclic), where μ_{ij} and $\mu_{ij,k}$ are the appropriate reduced masses

$$\mu_{ij} = \frac{m_i m_j}{m_i + m_j}, \quad \mu_{ij,k} = \frac{(m_i + m_j)m_k}{m_i + m_j + m_k}, \tag{7}$$

and μ is an arbitrary parameter with the dimension of mass that drops off in the final expressions. In terms of the Jacobi coordinates, the kinetic energy operator H_0 is written as

$$\begin{aligned}H_0 &= -\frac{1}{2\mu}\left(\frac{\partial^2}{\partial\boldsymbol{\rho}^2} + \frac{\partial^2}{\partial\boldsymbol{\lambda}^2}\right)\\ &= -\frac{1}{2\mu}\left(\frac{\partial^2}{\partial R^2} + \frac{5}{R}\frac{\partial}{\partial R} + \frac{K^2(\Omega)}{R^2}\right),\end{aligned} \tag{8}$$

where R is the six-dimensional hyperradius $R^2 = \boldsymbol{\rho}_{ij}^2 + \boldsymbol{\lambda}_{ij}^2$ and $K^2(\Omega)$ is the angular momentum operator, whose eigenfunctions (the hyperspherical harmonics) are $K^2(\Omega)Y_{[K]} = -K(K+4)Y_{[K]}$, with K being the grand orbital momentum. In terms of $Y_{[K]}$, the wave function $\psi(\boldsymbol{\rho}, \boldsymbol{\lambda})$ can be written in a symbolic shorthand as [10]

$$\psi(\boldsymbol{\rho}, \boldsymbol{\lambda}) = \sum_K \psi_K(R)Y_{[K]}(\Omega). \tag{9}$$

In the hyperradial approximation that we shall use below, $K = 0$ and $\psi = \psi(R)$. Since R^2 is exchange-symmetric, the baryon wave function is totally symmetric under exchange. Introducing the variable $x = \sqrt{\mu}R$ and averaging the interaction $U = V_c + V_{\text{string}}$ over the six-dimensional sphere Ω_6, one obtains the Schrödinger equation for $u(x) = x^{5/6}\psi(x)$:

$$\frac{d^2u(x)}{dx^2} + 2\left[E_0 + \frac{a}{x} - bx - \frac{15}{8x^2}\right]u(x) = 0, \tag{10}$$

with the boundary conditions $u(x) \sim \mathbb{O}(x^{5/2})$ as $x \longrightarrow 0$ and the asymptotic $u(x) \sim Ai(y) \sim \frac{1}{2}\pi^{-1/2}y^{-1/4}\exp\left(-\frac{2}{3}y^{3/2}\right)$, $y = (2b)^{1/3}x$, as $x \longrightarrow \infty$. In Eq. (10), E_0 is the ground state eigenvalue and

$$\begin{aligned}a &= \frac{2\alpha_s}{3}\frac{16}{3\pi}\sum_{i<j}\sqrt{\mu_{ij}},\\ b &= \frac{1}{R\sqrt{\mu}}\int V_{\text{string}}(\mathbf{r}_1, \mathbf{r}_2, \mathbf{r}_3)\frac{d\Omega_6}{\pi^3}.\end{aligned} \tag{11}$$

The potential $V_{\text{string}}(\mathbf{r}_1, \mathbf{r}_2, \mathbf{r}_3)$ has a rather complicated structure. In a Y shape, the strings meet at 120° in order to ensure the minimum energy. This shape moves continuously to a two-legs configuration, where the legs meet at an angle larger than 120°. Let φ_{ijk} be the angle between the line from quark i to quark j and that from quark j to quark k. If φ_{ijk} are all smaller than 120°, then the equilibrium junction position coincides with the so-called Torichelli point of the triangle in which the vertices of the three quarks are situated. In this case, in terms of the variables x, $\theta = \arctan(\rho_{12}/\lambda_{12})$, and $\cos\chi = \boldsymbol{\rho}_{12}\cdot\boldsymbol{\lambda}_{12}/\rho_{12}\lambda_{12}$ ($0 \leqq \theta \leqq \pi/2$, $0 \leqq \chi \leqq \pi$), one obtains

$$\begin{aligned}l_{\min}^2 &= x^2\cos^2\theta\left(\frac{(m_1^3 - m_2^3)\tan^2\theta}{m_1m_2(m_1^2 - m_2^2)}\right.\\ &\left. + \left(\frac{m_2 - m_1}{m_2 + m_1}\cos\chi + \sqrt{3}\sin\chi\right)\frac{\tan\theta}{m} + \frac{1}{\mu_{12,3}}\right),\end{aligned} \tag{12}$$

where $m^2 = m_1m_2m_3/(m_1 + m_2 + m_3)$. For the case $m_1 = m_2 = m_3$, this expression coincides with that derived in [11]. If $\varphi_{ijk} > 120°$, the lowest energy configuration has the junction at the position of quark j and $l_{\min} = r_{ij} + r_{jk}$, where

$$\begin{aligned}r_{12} &= \frac{x\sin\theta}{\sqrt{\mu_{12}}},\\ r_{13} &= \frac{x\cos\theta}{\sqrt{\mu_{12,3}}}\sqrt{\frac{m^2}{m_1^2}\tan^2\theta + \frac{2m}{m_1}\tan\theta\cos\chi + 1},\end{aligned} \tag{13}$$

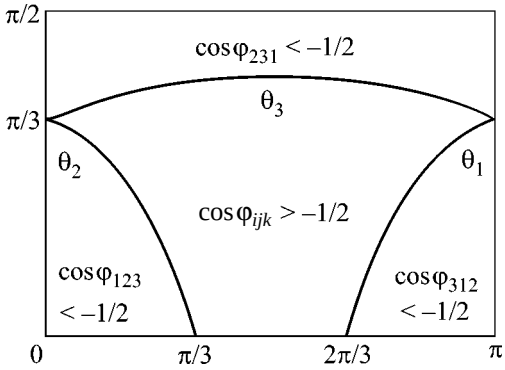

The four regions in the (θ, χ) plane corresponding to $\varphi_{ijk} \geq 120°$ and $\varphi_{ijk} \leq 120°$ for the case of equal quark masses.

and

$$r_{23} = \frac{x\cos\theta}{\sqrt{\mu_{12,3}}}\sqrt{\frac{m^2}{m_2^2}\tan^2\theta - \frac{2m}{m_2}\tan\theta\cos\chi + 1}. \quad (14)$$

The boundaries corresponding to the various regions in the (θ, χ) plane are $\theta_{1(2)}(\chi) = \arctan(m_{1(2)}(\mp\cos\chi - \sin\chi/\sqrt{3})/m)$, $\theta_3(\chi) = \arctan(m_2(f(\chi) + \sqrt{f^2(\chi) + 4\kappa})/2m)$, $f(\chi) = (1 - \kappa)\cos\chi + (1 + \kappa)\sin\chi/\sqrt{3}$, $\kappa = m_1/m_2$. These boundaries are shown in the figure for the case of equal quark masses.

Note that the frequently used approximation [6, 12] is to choose the string junction point as coinciding with the center-of-mass coordinate. In this case,

$$V_{\text{string}} = \sigma\sum_{i<j}\frac{1}{m_k}\sqrt{\mu\mu_{ij,k}}|\boldsymbol{\lambda}_{ij}|,$$
$$b = \sigma\frac{32}{15\pi}\sum_{i<j}\frac{\sqrt{\mu_{ij,k}}}{m_k}. \quad (15)$$

Table 1. Illustration of the accuracy of the approximation (15)

Baryon	Eq. (11)	Eq. (15)
qqq	1.583	1.663
qqs	1.556	1.636
qss	1.530	1.608
qsc	1.339	1.417
qqb	1.293	1.384
qcb	1.038	1.101
qbb	0.925	0.975

Shown are the values $b\sqrt{m_q}/\sigma$ given by Eqs. (11) and (15), where m_q is the lightest quark mass.

This approximation greatly simplifies the calculations and increases the value of b in Eq. (10) by ~5%, as illustrated by the results of Table 1.

We first solve Eq. (4) for the dynamical quark masses m_i and retain only the string potential in the effective Hamiltonian (1). This procedure is consistent with [6] but different from that of [12]. Then we add the perturbative Coulomb potential and solve Eq. (10) to obtain the ground state eigenvalues E_0. The baryon masses M_B are then obtained by solving Eq. (5).

We use the same parameters as in [13]: $\sigma = 0.15$ GeV^2 (this value has been confirmed in a recent lattice study [14]), $\alpha_s = 0.39$, $m_q^{(0)} = 0.009$ GeV, $m_s^{(0)} = 0.17$ GeV, $m_c^{(0)} = 1.4$ GeV, and $m_b^{(0)} = 4.8$ GeV. In Table 2, for various three-quark states, we give the quark masses m_i, the ground state eigenvalues E_0, and the baryon masses M_B. For completeness, in the last column, we report the values of the integral

$$\gamma = \int\frac{u^2(x)}{x^3}dx \quad (16)$$

in terms of which the quantities $R_{ijk} = (4\mu_{ij}^{3/2}/\pi^2)\gamma$ determining the probability of finding a quark i at the location of the quark j in a baryon ijk are expressed. These quantities are of special importance for the lifetime calculations of heavy hadrons.

Note that there is no good theoretical reason why quark masses m_i need to be the same in different baryons. Inspection of Table 2 shows that the masses of the light quarks (u, d, or s) are increased by ~100 MeV when going from light to heavy baryons. The dynamical masses of light quarks $m_q \sim \sqrt{\sigma} \sim$ 400–500 MeV qualitatively agree with the results of [13] obtained from the analysis of the heavy–light ground state mesons.

While studying Table 2 is sufficient to give an appreciation of the accuracy of our predictions, a few comments should be added. We expect the accuracy of the baryon predictions to be ~5–10%, which is partly due to the approximations employed in the derivations of the EH itself [6] and partly due to the error associated with the variational nature of the hyperspherical approximation. From this point of view, the overall agreement with the data is quite satisfactory. For example, we get $\frac{1}{2}(N + \Delta)_{\text{theory}} = 1144$ MeV vs. $\frac{1}{2}(N + \Delta)_{\text{exp}} = 1085$ MeV (a 5% increase in α_s would correctly give the $N - \Delta$ center of gravity), $\frac{1}{4}(\Lambda + \Sigma + 1\Sigma^*) = 1242$ MeV vs. experimental value of 1267 MeV. We also find $\Xi_{\text{theory}} = 1336$ MeV (without hyperfine splitting) vs. $\Xi_{\text{exp}}^{1/2} = 1315$ MeV and $\Xi_{c\text{theory}} = 2542$ MeV vs. $\Xi_{c\text{exp}} =$

Table 2

Baryon	m_1	m_2	m_3	E_0	M_B	γ
qqq	0.362	0.362	0.362	1.392	1.144	0.1389
qqs	0.367	0.367	0.407	1.362	1.242	0.1369
qss	0.371	0.411	0.411	1.335	1.336	0.1351
sss	0.415	0.415	0.415	1.307	1.426	0.1333
qqc	0.406	0.406	1.470	1.142	2.464	0.1241
qsc	0.409	0.448	1.471	1.116	2.542	0.1228
ssc	0.452	0.452	1.473	1.090	2.621	0.1214
qqb	0.425	0.425	4.825	1.054	5.823	0.1201
qsb	0.429	0.469	4.826	1.026	5.903	0.1188
ssb	0.471	0.471	4.826	1.000	5.975	0.1177
qcc	0.444	1.494	1.494	0.876	3.659	0.1143
scc	0.485	1.496	1.496	0.851	3.726	0.1134
qcb	0.465	1.512	4.836	0.753	6.969	0.1136
scb	0.505	1.514	4.837	0.729	7.032	0.1128
qbb	0.488	4.847	4.847	0.567	10.214	0.1207
sbb	0.526	4.851	4.851	0.544	10.273	0.1202

For various 3*q* systems in column (1), we display the dynamical quark masses given by Eq. (4), the ground state eigenvalue E_0 in Eq. (10), the baryon masses including the self-energy correction Eq. (5) (all in units of GeV), and the correlation function γ, Eq. (16) (in units of $\mathrm{GeV}^{3/2}$).

Table 3. Comparison of our predictions for ground state masses (in units of GeV) of doubly heavy baryons with other predictions

Baryon	This work	Ref. [12]	Ref. [15]	Ref. [16]	Ref. [17]
Ξ_{cc}	3.66	3.69	3.57	3.69	3.70
Ω_{cc}	3.73	3.86	3.66	3.84	3.80
Ξ_{cb}	6.97	6.96	6.87	6.96	6.99
Ω_{cb}	7.03	7.13	6.96	7.15	7.07
Ξ_{bb}	10.21	10.16	10.12	10.23	10.24
Ω_{bb}	10.27	10.34	10.19	10.38	10.34

2584 MeV. On the other hand, our study shows some difficulties in reproducing, e.g., the Ω-hyperon mass.

In Table 3, we compare the spin-averaged masses (computed without the spin–spin term) of the lowest doubly heavy baryons to the predictions of other models [15–17], as well as variational calculations of [12], for which the center of gravity of nonstrange baryons and hyperons is essentially a free parameter. Most recent predictions were obtained in a light quark–heavy diquark model [15, 16], in which case the spin-averaged values are $M = \frac{1}{3}(M_{1/2} + 2M_{3/2})$. Note that the wave function calculated in the hyperspherical approximation shows marginal diquark clustering in the doubly heavy baryons. This is a principally kinematic effect related to the fact that in this approximation the difference between the various mean values $\bar{r}_{ij}$ in a baryon is due to the factor $\sqrt{1/\mu_{ij}}$, which varies between $\sqrt{2/m_i}$ for $m_i = m_j$ and $\sqrt{1/m_i}$ for $m_i \ll m_j$. In general, in spite of the completely different physical picture, we find a reasonable agreement to within 100 MeV between the different predictions for the ground state masses of the doubly heavy baryons. Our prediction for M_{ccu} is 3.66 GeV with the perturbative hyperfine splitting $\Xi^*_{ccu} - \Xi_{ccu} \sim 40$ MeV. Note that the mass of Ξ^+_{cc} is rather sensitive to the value of the running *c*-quark mass $m_c^{(0)}$ [18].

In conclusion, we have shown that baryon spectroscopy can be unified in a single framework of the effective Hamiltonian, which is consistent with QCD. This picture uses a stringlike picture of confinement and perturbative one-gluon exchange potential. The main

advantage of this work is the demonstration of the fact that it is possible to describe all the baryons in terms of the only two parameters inherent to QCD, namely, σ and α_s.

This work was supported in part by the Russian Foundation for Basic Research (project nos. 00-02-16363 and 00-15-96786).

REFERENCES

1. K. Hagivara, K. Hikasa, K. Nakamura, *et al.*, Phys. Rev. D **66**, 010001 (2002).
2. M. Mattson, G. Alkhazov, A. G. Atamantchouk, *et al.*, Phys. Rev. Lett. **89**, 112001 (2002).
3. V. V. Kiselev and A. K. Likhoded, hep-ph/0208231.
4. See references [111]–[124] in B physics at the Tevatron hep-ph/0201071.
5. Yu. A. Simonov, Nucl. Phys. B **307**, 512 (1988).
6. Yu. A. Simonov, hep-ph/0205334.
7. Yu. S. Kalashnikova, I. M. Narodetskiĭ, and Yu. A. Simonov, Yad. Fiz. **46**, 1181 (1987) [Sov. J. Nucl. Phys. **46**, 689 (1987)].
8. V. L. Morgunov, A. V. Nefediev, and Yu. A. Simonov, Phys. Lett. B **459**, 653 (1999).
9. Yu. A. Simonov, Phys. Lett. B **515**, 137 (2001).
10. Yu. A. Simonov, Yad. Fiz. **3**, 630 (1966) [Sov. J. Nucl. Phys. **3**, 461 (1966)]; A. M. Badalyan and Yu. A. Simonov, Yad. Fiz. **3**, 1032 (1966) [Sov. J. Nucl. Phys. **3**, 755 (1966)].
11. M. Fabre de la Ripelle and Yu. A. Simonov, Ann. Phys. (N.Y.) **212**, 235 (1991).
12. M. Narodetskiĭ and M. A. Trusov, Yad. Fiz. **65**, 949 (2002) [Phys. At. Nucl. **65**, 917 (2002)]; hep-ph/0104019.
13. Yu. S. Kalashnikova and A. Nefediev, Phys. Lett. B **492**, 91 (2000).
14. T. T. Takahashi, H. Matsufuru, Y. Nemoto, and H. Suganuma, Phys. Rev. Lett. **86**, 18 (2002).
15. S. S. Gershtein, V. V. Kiselev, A. K. Likhoded, and A. I. Onishchenko, Phys. Rev. D **62**, 054021 (2000).
16. D. Ebert, R. N. Faustov, V. D. Galkin, and A. P. Matvienko, Phys. Rev. D **66**, 014008 (2002).
17. E. Bagan, H. G. Dosch, P. Gosdzinsky, *et al.*, Z. Phys. C **64**, 57 (1994).
18. I. M. Narodetskii and M. A. Trusov, in *Proceedings of the 5th International Conference BEACH2002, Vancouver, Canada, 2002*; hep-ph/0209044.

JETP Letters, Vol. 77, No. 2, 2003, pp. 63–67. From Pis'ma v Zhurnal Éksperimental'noĭ i Teoreticheskoĭ Fiziki, Vol. 77, No. 2, 2003, pp. 68–72.

Pion Distribution Amplitudes within the Instanton Model of QCD Vacuum¶

A. E. Dorokhov

Bogolyubov Laboratory of Theoretical Physics, Joint Institute for Nuclear Research, Dubna, Moscow region, 141980 Russia

Received December 18, 2002; in final form, December 25, 2002

The pion transition form factor for the process $\gamma^*\gamma^* \longrightarrow \pi^0$ at spacelike values of photon momenta is calculated within the effective quark–meson model with the interaction induced by instanton exchange. The leading and next-to-leading order power asymptotics of the form factor and the relation between the light-cone pion distribution amplitudes of twists 2 and 4 and the dynamically generated quark mass are found. © *2003 MAIK "Nauka/Interperiodica".*

PACS numbers: 13.40.Gp; 12.39.-x

The pion form factor $M_{\pi^0}(q_1^2, q_2^2)$ for the transition process $\gamma^*(q_1)\gamma^*(q_2) \longrightarrow \pi^0(p)$, where q_1 and q_2 are photon momenta, is related to fundamental properties of QCD dynamics at low and high energies. At zero photon virtualities, the observed value of the width for the two-photon decay of the π_0 meson

$$\Gamma(\pi^0 \longrightarrow \gamma\gamma) = \frac{e^2 m_{\pi_0}^3}{64\pi} M_{\pi^0}^2(0, 0) = 7.79(56)\ \text{eV}, \quad (1)$$

is consistent with the theoretical prediction due to the chiral anomaly for π_0

$$M_{\pi^0}(0, 0) = (4\pi^2 f_\pi)^{-1}, \quad (2)$$

where $f_\pi = 92.4$ MeV is the pion weak decay constant.

The existing experimental data from the CELLO [1] and CLEO [2] collaborations on the form factor M_{π^0} for one almost real photon, $q_2^2 \approx 0$, with the virtuality of the other photon scanned up to 8 GeV^2 can be fitted by a monopole form factor:

$$M_{\pi^0}(q_1^2 = -Q^2, q_2^2 = 0)\Big|_{\text{fit}} = \frac{g_{\pi\gamma\gamma}}{1 + Q^2/\Lambda_\pi^2}, \quad (3)$$
$$\Lambda \simeq 0.77\ \text{GeV},$$

where $g_{\pi\gamma\gamma} = 0.275$ GeV^{-1} is the two-photon pion decay constant. The large Q^2 behavior of form factor (3) is in agreement with the lowest order perturbative QCD (pQCD) prediction [3]

$$M_{\pi^0}(q_1^2, q_2^2)\Big|_{Q^2 \to \infty} = J^{(2)}(\omega)\frac{1}{Q^2} + J^{(4)}(\omega)\frac{1}{Q^{(4)}} + O\left(\frac{\alpha_s}{\pi}\right) + O\left(\frac{1}{Q^6}\right), \quad (4)$$

where the leading (LO) and next-to-leading (NLO) order asymptotic coefficients $J(\omega)$ are expressed in terms of the light-cone pion distribution amplitudes (DA), $\varphi_\pi(x)$:

$$J^{(2)}(\omega) = \frac{4}{3} f_\pi \int_0^1 dx \frac{\varphi_\pi^{(2)}(x)}{1 - \omega^2(2x-1)^2},$$
$$J^{(4)}(\omega) = \frac{4}{3} f_\pi \Delta^2 \int_0^1 dx \frac{1 + \omega^2(2x-1)^2}{[1 - \omega^2(2x-1)^2]^2} \varphi_\pi^{(4)}(x). \quad (5)$$

In the above expressions, $Q^2 = -(q_1^2 + q_2^2) \geq 0$ is the total virtuality of the photons and $\omega = (q_1^2 - q_2^2)/(q_1^2 + q_2^2)$ is the asymmetry in their distribution. The distribution amplitudes are normalized as $\int_0^1 dx \varphi_\pi(x) = 1$, and the parameter Δ^2 characterizes the scale of the NLO power corrections. The first perturbative correction to the LO term in (4) was found in [4], and the NLO power corrections were discussed in [5, 6] and more recently in [7] within the light-cone sum rules.

The leading momentum power dependence of form factor (4) is dictated by the scaling property of the pion DA. But the coefficients of the power expansion depend crucially on the internal pion dynamics, which are

¶This article was submitted by the author in English.

parameterized by the nonperturbative pion DAs, $\varphi_\pi(x)$, defined at some normalization scale μ, with x being the fraction of the pion momentum p carried by a quark. At the asymptotically large normalization scale $\mu \longrightarrow \infty$, the DAs are determined in pQCD:

$$\begin{aligned}\varphi^{(2)}_{\pi,\,as}(x) &= 6x(1-x),\\ \varphi^{(4)}_{\pi,\,as}(x) &= 30x^2(1-x)^2.\end{aligned} \tag{6}$$

However, for the description of the experimentally observable hard exclusive processes, one needs to know the DAs normalized at virtuality $\mu^2 \sim 1$ GeV^2. The aim of this letter is to calculate the pion transition form factor in the kinematical region up to moderately large Q^2 and extract from its power expansion in $1/Q^2$ the pion DAs at a normalization scale typical for hadrons. The calculations carried out within the effective model with nonlocal quark–quark interactions are consistent with the chiral anomaly and result in relations between the DAs of twists 2 and 4 and the dynamically generated nonlocal quark mass. The usage of the covariant nonlocal low-energy model based on the Schwinger–Dyson approach to the dynamics of quarks and gluons has many attractive features, such as that the approach preserves gauge invariance, it is consistent with the low-energy theorems, and it takes into account the long-distance dynamics of the bound state. Furthermore, the intrinsic nonlocal structure of the model may be motivated by fundamental QCD interactions induced by the instanton and gluon exchanges.

The effective quark–pion dynamics motivated by the instanton-induced interaction[1] may be summarized in terms of the dressed quark propagator

$$S^{-1}(p) = \hat{p} - M(p^2),$$

the quark–pion vertex

$$\Gamma^a_\pi(k, p, k' = k + p) = \frac{i}{f_\pi}F(k^2, k'^2)\gamma_5\tau^a,$$

$$F(k^2, k'^2) = \sqrt{M(k^2)M(k'^2)},$$

and the quark–photon vertex satisfying the Ward–Takahashi identity

$$\begin{aligned}&\Gamma^\mu(k, q, k' = -k - q)\\ &= eQ[\gamma_\mu - (k + k')_\mu G(k^2, k'^2)],\\ &G(k^2, k'^2) = \frac{M(k'^2) - M(k^2)}{k'^2 - k^2},\end{aligned}$$

where $M(k^2)$ is the dynamically generated quark mass. The dynamical quark mass characterizes the momentum dependence of an order parameter for spontaneous breaking of chiral symmetry and may be expressed in terms of the gauge-invariant nonlocal quark condensate [9]. The inverse size of the nonlocality scale, Λ, is naturally related to the average virtuality of quarks that flow through the vacuum, $\lambda_q^2 \sim \Lambda^2$. The value of λ_q^2 is known from the QCD sum rule analysis, $\lambda_q^2 \approx 0.4 \pm 0.1$ GeV^2 [10], and, within the instanton model, may be expressed through the average instanton size, ρ_c, as $\lambda_q^2 \approx 2\rho_c^{-1}$ [11]. The pion weak decay constant is expressed by the Pagels–Stokar formula

$$f_\pi^2 = \frac{N_c}{4\pi^2}\int_0^\infty du\frac{uM(u)[M(u) - uM'(u)/2]}{D^2(u)}, \tag{7}$$

where $M'(u) = \frac{d}{du}M(u)$ and $D(u) = u + M^2(u)$.

The invariant amplitude for the process $\gamma^*\gamma^* \longrightarrow \pi^0$ is given by

$$\begin{aligned}&A(\gamma^*(q_1, \epsilon_1)\gamma^*(q_2, \epsilon_2) \longrightarrow \pi^0(p))\\ &= -ie^2\varepsilon_{\mu\nu\rho\sigma}\epsilon_1^\mu\epsilon_2^\nu q_1^\rho q_2^\sigma M_{\pi^0}(q_1^2, q_2^2),\end{aligned}$$

where ϵ_i^μ are the photon polarization vectors. In the effective model, one finds the contribution of the triangle diagram to the invariant amplitude to be

$$\begin{aligned}A(\gamma_1^*\gamma_2^* \longrightarrow \pi^0) &= -ie^2\frac{N_c}{3f_\pi}\int\frac{d^4k}{(2\pi)^4}F(k_+^2, k_-^2)\\ &\times\{\mathrm{tr}[i\gamma_5 S(k_-)\hat{\epsilon}_2 S[k - q/2]\hat{\epsilon}_1 S(k_+)]\\ &+ \mathrm{tr}[i\gamma_5 S(k_-)S[k - q/2]\hat{\epsilon}_1 S(k_+)](\epsilon_2, 2k - q_1)\\ &\times G((k - q/2)^2, k_-^2)\\ &+ \mathrm{tr}[i\gamma_5 S(k_-)\hat{\epsilon}_2 S[k - q/2]S(k_+)](\epsilon_1, 2k + q_2)\\ &\times G(k_+^2, (k - q/2)^2)\} + (q_1 \longleftrightarrow q_2;\ \epsilon_1 \longleftrightarrow \epsilon_2),\end{aligned} \tag{8}$$

where $p = q_1 + q_2$, $q = q_1 - q_2$, $k_\pm = k \pm p/2$. In the adopted chiral limit ($p^2 = m_\pi^2 = 0$) with both photons real ($q_i^2 = 0$), one finds the result

$$\begin{aligned}M_{\pi^0}(0, 0) &= \frac{N_c}{6\pi^2 f_\pi}\\ &\times\int_0^\infty du\frac{uM(u)[M(u) - 2uM'(u)]}{D^3(u)} = \frac{1}{4\pi^2 f_\pi},\end{aligned} \tag{9}$$

which is consistent with the chiral anomaly.

The LO behavior of the form factor at large photon virtualities is given by the contribution of the first term in (8), and the NLO power corrections are generated by the second and third terms in (7) and also appear as the

[1] See for a review, e.g., [8].

correction to the first term. Thus, for large $q_1^2 = q_2^2 = -Q^2/2$ and $p^2 = 0$, the form factor has the asymptotics

$$M_{\pi^0}(-Q^2/2, -Q^2/2)\big|_{Q^2\to\infty} = \frac{4f_\pi}{3Q^2}\left(1+\frac{\Delta^2}{Q^2}\right)+O\left(\frac{1}{Q^6}\right), \quad (10)$$

$$\Delta^2 = \frac{N_c}{4\pi^2 f_\pi^2}\int_0^\infty du \frac{u^2 M(u)\left(M(u)+\frac{1}{3}uM'(u)\right)}{D^2(u)}, \quad (11)$$

which is in agreement with expressions (4) and (5) for the asymptotic coefficients at $\omega = 0$. The parameter Δ^2 has an extra power of u in the integral with respect to (7) and thus is proportional to the matrix element $\langle \pi(p)|g_s\bar{d}\tilde{G}_{\alpha\mu}\gamma_\alpha p_\mu u|0\rangle$. The power correction (11) is the sum of the positive contribution coming from the higher Fock states in the pion, effectively taken into account by the second and third terms in (8), and the negative two-particle contribution due to the first term in (8).[2] Note that the model provides the opposite sign of the power correction compared with the QCD sum rule prediction [5].

In the general case, at large Q^2, the model calculations reproduce the QCD factorization result (4), (5) with the DAs given by

$$\varphi_\pi^{(2)}(x) = \frac{N_c}{4\pi^2 f_\pi^2}\int_{-\infty}^{\infty}\frac{d\lambda}{2\pi} \times\int_0^\infty du \frac{F(u+i\lambda\bar{x}, u-i\lambda x)}{D(u-i\lambda x)D(u+i\lambda\bar{x})} \times[xM(u+i\lambda\bar{x})+(x\longleftrightarrow\bar{x})], \quad (12)$$

$$\varphi_\pi^{(4)}(x) = \frac{1}{\Delta^2}\frac{N_c}{4\pi^2 f_\pi^2}\int_{-\infty}^{\infty}\frac{d\lambda}{2\pi} \times\int_0^\infty du \frac{uF(u+i\lambda\bar{x}, u-i\lambda x)}{D(u-i\lambda x)D(u+i\lambda\bar{x})} \times[\bar{x}M(u+i\lambda\bar{x})+(x\longleftrightarrow\bar{x})]. \quad (13)$$

In these expressions, the u variable plays the role of the quark transverse momentum squared, $\vec{k}_\perp^2$, and $\lambda x, -\lambda\bar{x}$ are the longitudinal projections of the quark momentum onto the light cone directions. The model DAs are defined at the normalization scale characterized by the vacuum nonlocality $\mu^2 \sim \Lambda^2$. Concerning the LO DA, $\varphi_\pi^{(2)}(x)$ similar results within the instanton model were derived earlier in [13, 14].

[2] In [12], only part of the NLO power corrections were discussed.

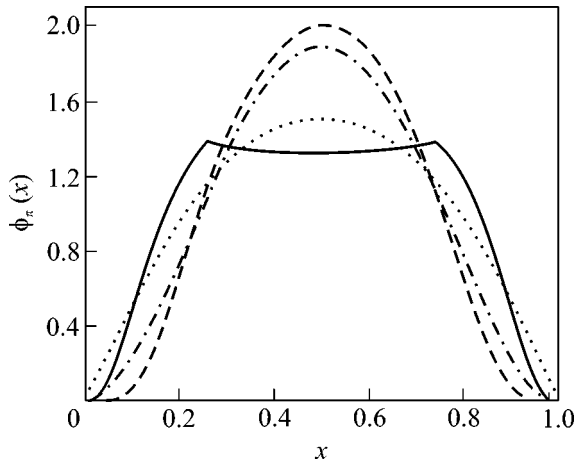

Fig. 1. The pion distribution amplitudes (normalized to unity): the model predictions for twist-2 (solid line) and twist-4 (dashed line) components and the perturbative asymptotic limits of twist-2 (dotted line) and twist-4 (dash-dotted line) amplitudes.

In Fig. 1, the LO and NLO pion DAs, normalized by unity, are illustrated in comparison with perturbative asymptotic DAs. For numerical analysis, the dynamical mass profile is chosen in the Gaussian form $M(k^2) = M_q\exp(-2k^2/\Lambda^2)$, where we take $M_q = 350$ MeV and fix $\Lambda = 1.29$ GeV from the pion constant (7). Then, the value $\Delta^2 \equiv J^{(4)}(\omega = 1)/J^{(2)}(\omega = 1) = 0.205$ GeV^2 is obtained, which characterizes the scale of the power corrections in hard exclusive processes. The mean square radius of the pion for the transition $\gamma^*\pi^0 \longrightarrow \gamma$ is $r_{\pi\gamma}^2 = (0.566\text{ fm})^2$ and is numerically close to the value derived from (3). As is clear from Fig. 1, the predicted pion DAs for a realistic choice of the model parameters are close to the asymptotic DAs. The corresponding conclusion with respect to the LO DA is in agreement with the results obtained in [15, 16], as is seen from comparison of Figs. 1 and 2.

The asymptotic coefficients $J^{(2,4)}(\omega)$ given by (5), (12), and (13) can be identically rewritten in the form

$$J^{(2)}(\omega) = -\frac{1}{\pi^2 f_\pi}\int_0^\infty du u\int_0^\infty dv\left\{\frac{M^{1/2}(z_-)}{D(z_-)}\frac{\partial}{\partial z_+} \times\left(\frac{M^{3/2}(z_+)}{D(z_+)}\right)+(z_-\longleftrightarrow z_+)\right\}, \quad (14)$$

$$J^{(4)}(\omega) = \frac{2}{\pi^2 f_\pi}\int_0^\infty du\int_0^\infty dv v\left\{\frac{M^{1/2}(z_-)}{D(z_-)}\left[\frac{M^{3/2}(z_+)}{D(z_+)} + u\frac{\partial}{\partial z_+}\left(\frac{M^{3/2}(z_+)}{D(z_+)}\right)\right]+(z_-\longleftrightarrow z_+)\right\}, \quad (15)$$

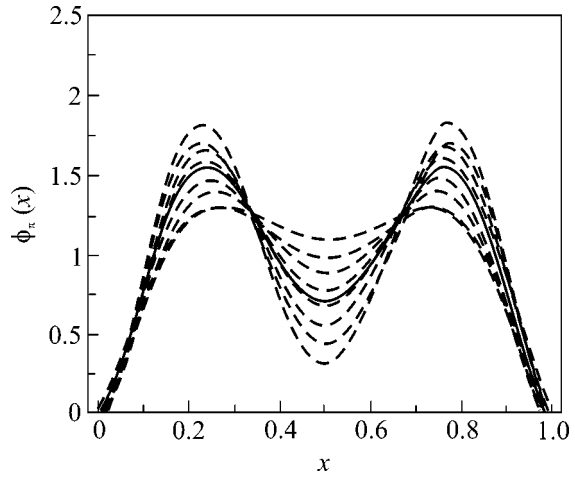

Fig. 2. An admissible set of twist-2 pion distribution amplitudes (dashed lines, the best fit is the solid line) as predicted within the QCD sum rules (from [15b]) with vacuum nonlocality parameter $\lambda_q^2 = 0.4$ GeV^2 defined at $\mu^2 \approx 1$ GeV^2.

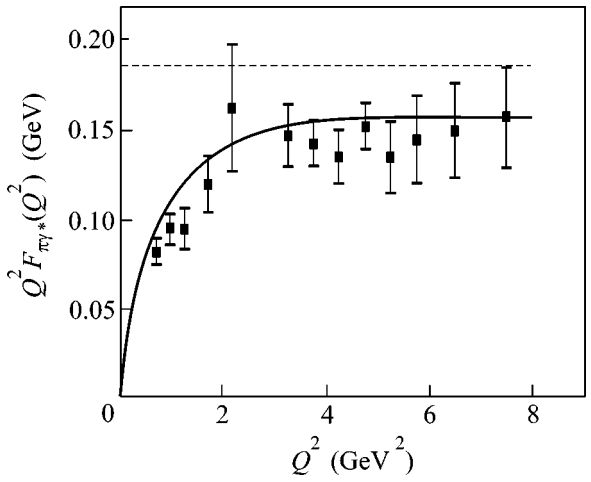

Fig. 3. The pion–photon transition form factor $Q^2F_{\pi\gamma^*}(Q^2)$ (solid line) and its perturbative limit $2f_\pi$ (dotted line). The experimental points ($Q^2F_{\pi\gamma^*\gamma}$) are taken from [2].

where $z_\pm = u + v(1 \pm \omega)$. With the model parameters given above, we find the asymptotic coefficients $J^{(2)}(\omega = 1) = 0.171$ GeV and $J^{(4)}(1)/J^{(2)}(1) = 0.254$ GeV^2 for the process $\gamma\gamma^* \longrightarrow \pi^0$. When the error in the experimental fit is taken into account, the estimate of the LO coefficient, $J^{(2)}(1)$, is in agreement with the fit of CLEO data $J^{(2)}_{\exp}(1) = 0.16 \pm 0.03$ GeV. The NLO power correction, Δ^2, grows by 20% when the kinematics change from equally distributed photon virtualities to an asymmetric distribution.

In Figs. 3 and 4, we plot the model predictions for the form factors $F_{\pi\gamma^*}(Q^2) = M_{\pi^0}(-Q^2, 0)$ and $F_{\pi\gamma^*\gamma^*}(Q^2) = M_{\pi^0}(-Q^2/2, -Q^2/2)$ multiplied by squared momentum Q^2 for the processes $\gamma\gamma^* \longrightarrow \pi^0$ and $\gamma^*\gamma^* \longrightarrow \pi^0$, respectively. In Fig. 3, we also indicate the CLEO data. In the model form factors, the perturbative α_s corrections [4] to the leading twist-2 term are taken into account with the running coupling, $\alpha_s(Q^2)$, which has a zero at zero momentum [17]. With such effective behavior in the infrared region, the perturbative corrections do not influence the chiral anomaly. At high momentum squared, the leading perturbative correction provides a negative contribution to the form factors and compensates the NLO power corrections in the region 2–10 GeV^2. The unknown perturbative corrections to the twist-4 contribution are considered as inessential. The power corrections generated by the twist-3 pion DAs are also negligible, since they are proportional to the small current quark mass.

In conclusion, within the covariant nonlocal model describing quark–pion dynamics, we obtain the $\pi\gamma^*\gamma^*$ transition form factor in the region up to moderately high momentum transfer squared, where the perturbative QCD evolution does not yet reach the asymptotic regime. From comparison of the kinematical dependence of the coefficients of the power expansion in $1/Q^2$ of the transition pion form factor, as it is given by pQCD and the nonperturbative model, the relations (12), (13) between the pion DAs and the dynamical quark mass and quark–pion vertex are derived. The other possible sources of contributions to the form factor arise from inclusion into the model of the low-lying vector and axial-vector mesons. They do not change the result given by the chiral anomaly (9) for the two-gamma pion decay. The contributions of the vector mesons to the leading-order asymptotics of the form factor are expected to be small, but they may be more

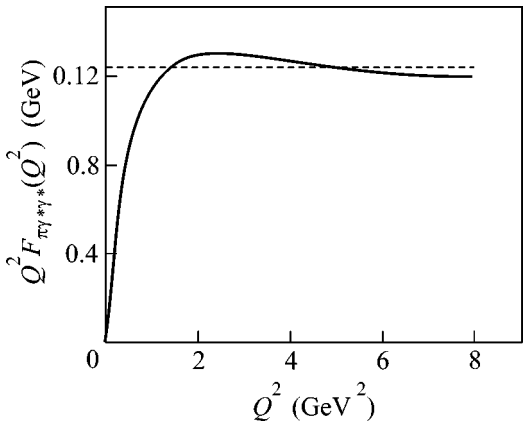

Fig. 4. The pion–photon transition form factor $Q^2F_{\pi\gamma^*\gamma^*}(Q^2)$ (solid line) and its perturbative limit $4f_\pi/3$ (dashed line).

important in treating the twist-4 power corrections and the pion mean radius.

I am grateful to A.P. Bakulev, W. Broniowski, A. Di Giacomo, A.S. Gorski, N.I. Kochelev, S.V. Mikhailov, M.K. Volkov, L. Tomio, and V.L. Yudichev for many useful discussions on topics related to this work. This work was supported by the Russian Foundation for Basic Research (project nos. 01-02-16431 and 02-02-16194) and by INTAS (grant no. 2000-366).

REFERENCES

1. CELLO Collab. (H.-J. Behrend *et al.*), Z. Phys. C **49**, 401 (1991).
2. CELLO Collab. (J. Gronberg *et al.*), Phys. Rev. D **57**, 33 (1998).
3. G. P. Lepage and S. J. Brodsky, Phys. Lett. B **87**, 359 (1979); Phys. Rev. D **22**, 2157 (1980).
4. F. Del Aguila and M. K. Chase, Nucl. Phys. B **193**, 517 (1981); E. Braaten, Phys. Rev. D **28**, 524 (1983); È. P. Kadantseva, S. V. Mikhaĭlov, and A. V. Radyushkin, Yad. Fiz. **44**, 507 (1986) [Sov. J. Nucl. Phys. **44**, 326 (1986)].
5. V. L. Chernyak, A. R. Zhitnitskiĭ, and I. R. Zhitnitskiĭ, Yad. Fiz. **38**, 1074 (1983) [Sov. J. Nucl. Phys. **38**, 645 (1983)]; V. A. Novikov, M. A. Shifman, A. I. Vainshtein, *et al.*, Nucl. Phys. B **237**, 525 (1984).
6. A. S. Gorsky, Yad. Fiz. **50**, 796 (1989) [Sov. J. Nucl. Phys. **50**, 498 (1989)].
7. A. Khodjamirian, Eur. Phys. J. C **6**, 477 (1999); T. Yeh, hep-ph/0107018.
8. I. V. Anikin, A. E. Dorokhov, and L. Tomio, Fiz. Élem. Chastits At. Yadra **31**, 1023 (2000) [Phys. Part. Nucl. **31**, 509 (2000)].
9. A. E. Dorokhov and W. Broniowski, Phys. Rev. D **65**, 094007 (2002).
10. V. M. Belyaev and B. L. Ioffe, Zh. Éksp. Teor. Fiz. **83**, 876 (1982) [Sov. Phys. JETP **56**, 493 (1982)]; A. A. Ovchinnikov and A. A. Pivovarov, Yad. Fiz. **48**, 1135 (1988) [Sov. J. Nucl. Phys. **48**, 721 (1988)].
11. A. E. Dorokhov, S. V. Esaibegian, and S. V. Mikhailov, Phys. Rev. D **56**, 4062 (1997).
12. A. E. Dorokhov, hep-ph/0206088.
13. V. M. Braun and I. E. Filyanov, Z. Phys. C **48**, 239 (1990).
14. S. V. Esaibegyan and S. N. Tamaryan, Yad. Fiz. **51**, 485 (1990) [Sov. J. Nucl. Phys. **51**, 310 (1990)]; A. E. Dorokhov, Nuovo Cimento A **109**, 391 (1996); V. Yu. Petrov and P. V. Pobylitsa, hep-ph/9712203.
15. S. V. Mikhaĭlov and A. V. Radyushkin, Yad. Fiz. **52**, 1095 (1990) [Sov. J. Nucl. Phys. **52**, 697 (1990)]; A. P. Bakulev, S. V. Mikhailov, and N. G. Stefanis, Phys. Lett. B **508**, 279 (2001).
16. P. Kroll and M. Raulfs, Phys. Lett. B **387**, 848 (1996); I. V. Anikin, A. E. Dorokhov, and L. Tomio, Phys. Lett. B **475**, 361 (2000); M. Diehl, P. Kroll, and C. Vogt, Eur. Phys. J. C **22**, 439 (2001).
17. K. Van Acoleyen and H. Verschelde, hep-ph/0203211.

JETP Letters, Vol. 77, No. 2, 2003, pp. 68–73. Translated from Pis'ma v Zhurnal Éksperimental'noĭ i Teoreticheskoĭ Fiziki, Vol. 77, No. 2, 2003, pp. 73–78.

The Spectrum of a Hydrogen Atom in a Superstrong Magnetic Field and the Zeldovich Effect in the Short-Range Coulomb Problem

B. M. Karnakov

Moscow Institute of Engineering Physics, Kashirskoe sh. 31, Moscow, 115409 Russia
e-mail: karnak@theor.mephi.ru

Received November 29, 2002

We derive formulas that describe the energy spectrum of a hydrogen atom in a superstrong magnetic field for states with various magnetic quantum numbers. Comparison with available numerical calculations of the spectrum indicates that the results obtained are highly accurate. These results can be interpreted as a manifestation of the Zeldovich effect regarding the rearrangement of the hydrogen atomic spectrum under the influence of strong Coulomb potential distortion at short distances in the problem under consideration. © *2003 MAIK "Nauka/Interperiodica".*

PACS numbers: 32.30.-r; 03.65.Ge

1. The problem of a hydrogen atom in an extremely strong magnetic field, $H \gg H_0 \equiv e^3m^2c/\hbar^3 = 2.35 \times 10^9$ G, is of great interest in astrophysics and solid-state physics. A large number of studies in which the energy spectrum of such an atom was computed by various numerical methods have been published (see [1] and references therein).

Nevertheless, as far as I know, there are no correct analytic expressions for this spectrum [see, however, the remark after formula (12)]. The standard formula (Elliott and Loudon) for the binding energy of the ground atomic state

$$\varepsilon_0(H) \equiv \frac{\hbar^2\kappa^2}{2m} = \frac{me^4}{2\hbar^2}\ln^2\left(\frac{H}{H_0}\right), \qquad (1)$$

see [2] (§112), even at $H \sim (10^4–10^5)H_0$ (at the validity boundary of the nonrelativistic approximation) gives only order-of-magnitude values of ε_0, which are larger by a factor of 3 than the result of an accurate numerical calculation. Moreover, the inverse of dependence (1)

$$H(\kappa) = H_0 e^{\kappa a_B} \qquad (2)$$

(a_B is the Bohr radius) is unsatisfactory altogether, because it gives an $H(\kappa)$ underestimated by two orders of magnitude (see Table 1 below).

This discrepancy stems from the fact that both the derivation of formula (1) and the general considerations on the properties of the excited atomic state spectrum in [2] require a number of significant refinements. In particular, even and odd (with respect to the reflection of the electron coordinate along the magnetic field) levels are described by distinctly different expressions and are greatly shifted relative to each other. In this case, the Zeldovich effect regarding the possible rearrangement of the atomic hydrogen spectrum, $E_n = -me^4/2\hbar^2n^2$, under the influence of Coulomb potential distortion at short distances, $r \ll a_B$, manifests itself in the even-state spectrum. This effect, which was predicted by Zeldovich [3] in connection with the problem of electron energy levels in an extrinsic semiconductor, imposes stringent requirements on the pattern of this Coulomb potential distortion: for slow particles, it must be resonant. A similar behavior of the levels in the electron spectrum was found [4] in the relativistic problem with a nuclear charge $Z > 137$. In the past, the Zeldovich effect attracted wide attention, because it could manifest itself in hadron atoms (see [5–8]).

2. Choosing the vector potential of the external magnetic field in the form $\mathbf{A} = \frac{1}{2}[\mathbf{Hr}]$ and directing the z axis along $\mathbf{H}$, we have the following Hamiltonian of the system under consideration in the nonrelativistic approximation:[1]

$$\hat{H} = -\frac{1}{2}\Delta_\perp + \frac{1}{8}\left(\frac{H}{c}\right)^2\rho^2 + \frac{H}{2c}(\hat{l}_z + \hat{\sigma}_z)$$
$$-\frac{1}{2}\frac{\partial^2}{\partial z^2} - \frac{1}{\sqrt{\rho^2 + z^2}}.$$

[1] Below, we use the atomic system of units, $e = \hbar = m = 1$, in which the speed of light is $c = \alpha^{-1} = 137$.

0021-3640/03/7702-0068$24.00

Table 1

κ^2	H/c				a_H/a_B
	[1]	Eq. (12)	Eq. (2)	[10]	
47.783	10^5	1.003×10^5	1.0×10^3	1.7×10^5	3.2×10^{-3}
41.159	5×10^4	5.014×10^4	611	9.0×10^4	4.5×10^{-3}
28.282	10^4	9991	204	2.1×10^4	10^{-2}
23.747	5×10^3	4970	131	1.1×10^4	1.4×10^{-2}
18.610	2×10^3	1961	75	5.0×10^3	2.3×10^{-2}
15.325	10^3	962	50	2.7×10^3	3.2×10^{-2}
11.703	4×10^2	368	31	1.3×10^3	5.2×10^{-2}
9.4543	2×10^2	174	22	730	7.6×10^{-2}
7.5796	10^2	80	16	420	0.10

For a superstrong magnetic field, the adiabatic approximation can be used to solve the Schrödinger equation. In this case, the solution can be written as

$$\psi_{nn_\rho m}(\mathbf{r}) = R_{n_\rho m}(\boldsymbol{\rho})\chi_n(z),$$

where $R_{n_\rho m}(\boldsymbol{\rho})$ are the standard functions of the transverse electron motion in a purely magnetic external field [2] (we omitted the spin part of the wave function). The bound-state spectrum of the Hamiltonian can be represented as

$$E_{nn_\rho m\sigma_z} = \left(n_\rho + \frac{|m| + m + 1}{2} + \frac{\sigma_z}{2}\right)\frac{H}{c} - \frac{1}{2}\kappa^2_{n|m|n_\rho}, \quad (3)$$

where $\sigma_z = \pm1$, n is the quantum number for the longitudinal motion, and the last term defines the shift of the corresponding Landau level produced by the Coulomb potential. This shift can be determined from the Schrödinger equation for the longitudinal part of the wave function:

$$\left\{-\frac{1}{2}\frac{\partial^2}{\partial z^2} + U_{\text{eff}}(|z|) + \frac{\kappa^2}{2}\right\}\chi_n(z) = 0, \quad (4)$$

in which the effective potential energy is given by the expression

$$U_{\text{eff}}(|z|) = -\int\int \frac{1}{\sqrt{\rho^2 + z^2}}\left|R_{n_\rho m}(\boldsymbol{\rho})\right|^2 d^2\rho. \quad (5)$$

Note the following properties of this potential (the specific expressions for it depend on the quantum numbers n_ρ and $|m|$ for the transverse motion).

(1) At distances $|z| \le a_H \ll a_B$, $U_{\text{eff}}(|z|) \sim 1/a_H$, where $a_H = \sqrt{\hbar/m\omega_H}$ and $\omega_H = eH/mc$. In this case, $U_{\text{eff}}a_H^2 \sim a_H \ll 1$, so the potential at such distances is a shallow one-dimensional potential well.

(2) At $|z| \gg a_H$, the effective potential is a Coulomb one.

(3) Note also that $U_{\text{eff}}(|z|) + 1/|z| > 0$; i.e., the effective potential energy curve lies above the Coulomb one. The effective potential for the $m = n_\rho = 0$ states is

$$U_{\text{eff}}(|z|) = -\frac{\sqrt{2}}{a_H}\int_0^\infty e^{-\sqrt{2}|z|x/a_H - x^2}dx. \quad (6)$$

The solutions to Eq. (4) have a certain parity, $P = \pm1$, relative to the transformation $z \longrightarrow -z$. We begin with even states, for which $\chi'(0) = 0$. Treating the terms with U_{eff} and κ^2 in Eq. (4) at $|z| \le a_H \ll 1$ as a perturbation, we have in the zero approximation $\chi(z) = 1$ and $\chi'(z) = 0$. A more accurate value of $\chi'(z)$ can be calculated from Eq. (4) if we omit the term with the binding energy, substitute unity for $\chi(z)$ in the term with the effective potential, and integrate the resulting equation over z. As a result, we obtain

$$\chi'(|z|) = 2\int_0^{|z|} U_{\text{eff}}(|z|)dz. \quad (7)$$

For the subsequent analysis, we need $\chi'(|z|)$ only for distances $a_H \ll |z| \ll a_B$, where the effective potential is a Coulomb one. Taking into account the dependence of $R_{n_\rho m}(\boldsymbol{\rho})$ on ρ [the polynomials in ρ^2 multiplied by $\exp(-\rho^2/4a_H^2)$] and using the integral

$$\int_0^\infty x^{s-1}e^{-x}\ln x dx = \Gamma'(s) = \Gamma(s)\psi(s), \quad (8)$$

where $\psi(z)$ is the logarithmic derivative of the gamma function, we find that the derivative $\chi'(|z|)$ at these distances, according to formula (7), takes the form[2]

$$\chi'(|z|) \approx -2\ln\frac{|z|}{a_H} + A_{|m|n_\rho}. \quad (9)$$

Significantly, the term $A_{|m|n_\rho}$ does not depend on H. In particular, for the transverse nodeless states with $n_\rho = 0$, according to Eq. (8), we obtain

$$A_{|m|0} = -\ln 2 + \psi(1 + |m|). \quad (10)$$

Recall that $\psi(1) = -\gamma$, where $\gamma = 0.5772\ldots$ is the Euler constant, and $\psi(n+1) = -\gamma + \sum_{k=1}^{n}\frac{1}{k}$ for integer $n = 1, 2, \ldots$.

At the same time, the solution to Eq. (4) with a purely Coulomb effective potential, which exponentially decreases at large distances, $|z| \longrightarrow \infty$, is described by the Whittaker function:

$$\chi(|z|) = \text{const}\, W_{\nu,\,1/2}(2|z|/\nu)$$

with $\nu = 1/\kappa$. At small distances, $|z| \ll 1$, this solution is

$$\chi(|z|) = \left\{1 - 2|z|\ln(2\kappa|z|)\right. \\ \left. -\left[\kappa + 2\psi\left(1-\frac{1}{\kappa}\right) - 2 + 4\gamma\right]|z| + \ldots\right\} \quad (11)$$

(see [9], formula 9.237); we assume that const $= \Gamma(1-\nu)$. Differentiating this expression and equating to (9), one obtains an equation for the even-state spectrum:

$$\ln\frac{H}{c} \equiv \ln\frac{1}{a_H^2} = \kappa + 2\ln\kappa + 2\psi\left(1-\frac{1}{\kappa}\right) \\ + 4\gamma + 2\ln 2 + A_{|m|n_\rho}. \quad (12)$$

We emphasize that this equation directly defines $H(\kappa)$ for even levels; interestingly, $\exp\{-A_{|m|n_\rho}\}H(\kappa_{n|m|n_\rho})$ is a universal function (for a given n), which is the same for states with different quantum numbers $|m|$ and n_ρ.

The basic properties of this spectrum, i.e., the dependence $\kappa^{(+)}_{n|m|n_\rho}(H)$, can be easily understood if we notice an analogy between Eq. (12) and the equation that defines the s-state spectrum in a three-dimensional attractive Coulomb potential $U(r) = -e^2/r$ distorted at short distances, $r < a_B$, by a strong short-range potential $U_S(r)$, which can itself bind the particle (electron). This equation is [6–8]

$$\frac{1}{a_0} = \kappa + 2\ln\kappa + 2\psi\left(1-\frac{1}{\kappa}\right), \quad (13)$$

where a_0 is the (renormalized) scattering length in the s state in the potential U_S. Comparison of Eqs. (12) and (13) indicates that an analogue of the inverse scattering length is

$$\frac{1}{a_0(H)} \equiv \ln\frac{H}{c} - 4\gamma - 2\ln 2 - A_{|m|n_\rho}, \quad (14)$$

in this case, under the validity conditions $a_H \ll a_0(H)$ for the approach in question, with $a_0(H) > a_B/10$ numerically; thus, for $H/c = 10^4$ at $m = n_\rho = 0$, we have $a_0(H) \approx 0.15$ and $a_H = 0.01$.

Bearing in mind this analogy, we note the following properties of the even-state spectrum:

(1) For each pair of quantum numbers $|m|$ and n_ρ, Eq. (12) has an infinite number of roots $\kappa^{(+)}_{n|m|n_\rho} > 0$. The lowest (with $n = 1$) root with $\kappa^{(+)}_{1|m|n_\rho} \gg 1$ corresponds to the deep level on the atomic scale; cf. Eq. (1).

(2) The remaining roots, with $n \geq 2$, correspond to excited states. The corresponding energy levels are located between the neighboring unshifted Coulomb n_s levels with the principal quantum numbers n' equal to $(n-1)$ and n.

Note that an equation similar to Eq. (12), in which $\psi(1) = -\gamma$ was substituted for $\psi(1 - 1/\kappa)$, was derived in [10] for the lower (deep) $n = 1^+$ level. This equation is definitely inapplicable to excited even states but is still asymptotically exact for $H(\kappa)$ for the lower level. However, the above substitution results in the clear loss of accuracy at large but finite H (limited because of the use of the nonrelativistic approximation); see Table 1.

For a further analysis of the states in the lower part of the energy spectrum, see Section 3.

Let us now discuss the properties of the odd states that follow from Eq. (4). The energy spectrum for the s levels in a three-dimensional potential $U(r)$ is known to match the energy spectrum for the odd levels in a symmetric one-dimensional potential $U(|z|)$ of the same form. Therefore, given the properties of $U_{\text{eff}}(|z|)$ noted above, we can assert that, if the potential in the corresponding three-dimensional problem is written as $U_{\text{eff}}(r) \equiv -1/r + (U_{\text{eff}}(r) + 1/r)$, then the last term can be treated as a small distortion of a purely Coulomb potential and it can be taken into account by using the pertur-

[2] First, we should integrate $1/\sqrt{z^2+\rho^2}$ in the effective potential (see Eq. (5)) over z and pass to the limit $|z| \longrightarrow \infty$, neglecting the decreasing expansion terms. The integral with $\ln|z|$ can then be easily calculated and the z-independent integral with $\ln\rho$ can be expressed in terms of integrals (8). Note also that, although $\chi'(|z|) > 1$ in Eq. (9), we still have $\chi(|z|) \approx 1$.

bation theory. Thus, we can write the following expression for the odd n levels in the potential $U_{\text{eff}}(|z|)$:

$$E^{(-)}_{n|m|n_\rho} \equiv -\frac{1}{2}\left(\kappa^{(-)}_{n|m|n_\rho}\right)^2 = -\frac{1}{2n^2} + \int\left(U_{\text{eff}}(r) + \frac{1}{r}\right)\left|\psi^{(0)}_{ns}(r)\right|^2 d^3r, \quad (15)$$

where $\psi^{(0)}_{ns}(r)$ are the unperturbed wave functions of the ns states in the Coulomb potential. The levels are slightly shifted upward relative to the Coulomb levels [the integrand in Eq. (15) is positive].

When the short-range distortion of the Coulomb potential, $U_{\text{eff}}(r) + 1/r$, decreases with increasing r faster than $\propto 1/r^3$, we can factor $\left|\psi^{(0)}_{ns}(0)\right|^2$ outside the integral sign and derive the following expression:[3]

$$E^{(-)}_{n|m|n_\rho} = -\frac{1}{2n^2} + \int\left(U_{\text{eff}}(r) + \frac{1}{r}\right)d^3r\left|\psi^{(0)}_{ns}(0)\right|^2. \quad (16)$$

This expression describes the shifts of the Coulomb levels with arbitrary n; $\delta E^{(-)}_{n|m|n_\rho} \propto \left|\psi^{(0)}_{ns}(0)\right|^2 = 1/\pi n^3$.

We can obtain an asymptotic expansion for the binding energy of the lower odd level by using expressions (6) and (15) for $m = n_\rho = 0$ and generalize it to the states with arbitrary n by using formula (16):

$$\left(\kappa^{(-)}_{n00}\right)^2 = \frac{1}{n^2} - \frac{4}{n^3}\left\{\frac{c}{H}\ln\frac{H}{2c} + (\gamma + 2)\frac{c}{H} - 2\sqrt{2\pi}\left(\frac{c}{H}\right)^{3/2} + \ldots\right\}. \quad (17)$$

Below, we also generalize this result to the nodeless states with arbitrary $|m|$:

$$E_{n|m|0}(H) = (-1)^{|m|}\frac{1}{|m|!}H^{|m|+1}\frac{d^{|m|}}{dH^{|m|}}\left(\frac{1}{H}E_{n00}(H)\right).$$

3. Let us discuss our results and compare them with available numerical calculations. The hydrogen atomic spectrum for a number of states with m = 0 below the Landau ground level was calculated with a high precision in [1] over a wide H range. Table 1 illustrates the dependence $H(\kappa)$ for the ground atomic state. For the listed values of κ^2, this table compares the corresponding magnetic field strengths taken from [1] and [10], as well as those calculated from formulas (12) and (2). Also given in the table are the a_H/a_B ratios, whose smallness is required for the adiabatic approximation to be applicable.

Table 2

H/c	$n = 2^+$ ($2s$)		$n = 1^-$ ($2p$)	
	$\kappa^2(H)$, [1]	$\kappa^2(H)$, Eq. (12)	$\kappa^2(H)$, [1]	$\kappa^2(H)$, Eq. (17)
10^4	–	0.65525	–	0.99760
3000	–	0.62390	–	0.99356
2000	0.61248	0.61250	0.99119	0.99111
1000	0.59171	0.59207	0.98499	0.98482
400	0.56206	0.56342	0.97073	0.97028
200	0.53794	0.54079	0.95306	0.95235
140	0.52496	0.52888	0.94092	0.94014
100	0.51236	0.51760	0.92723	0.92655
60	0.49261	0.50046	0.90186	0.90192
40	0.47640	0.48696	0.87748	0.87888
20	0.44768	0.46440	0.82676	0.83073
10	0.41790	0.44291	0.76530	0.75298

Note that the dependence $\kappa^2(H)$ of the level binding energy on magnetic field is given by Eq. (12) with a much higher accuracy than its inverse dependence $H(\kappa)$ presented in Table 1. Thus, according to Eq. (12), we have the following binding energies for magnetic field strengths H/c of 10^5, 5×10^3, and 200: 47.755 (6×10^{-4}), 23.783 (1.5×10^{-3}), and 9.84 (4×10^{-2}), respectively; the error in the result obtained is given in parentheses (cf. the data in the table). This difference stems from the fact that the dependence $H(\kappa)$ is sharply exponential, and this circumstance is one of the reasons why formula (2) mentioned in the Introduction is inconsistent.

Note also that, as expected [because $a_0(H) > a_B/10$], the binding energy for the ground level in a strong magnetic field is large on the scale of ordinary atomic energies.

Below, we also present Table 2. It gives the binding energies for the lower excited atomic states with $m = 0$ taken from [1] and calculated from the asymptotic formulas (12) and (17) for the states with the quantum numbers $n = 2^+$, $m = n_\rho = 0$ and $n = 1^-$, $m = n_\rho = 0$ (in [1], these are classified as the $2s$ and $2p$ states with $m = 0$, respectively). We make the following remarks regarding the results presented in this table:

(1) Comparison with the data of Table 1 indicates that, for these states excited in the longitudinal direction of motion, our approach provides a higher accuracy. This circumstance can be easily explained, because the size of the localization region for the wave function increases in the longitudinal direction for the

[3] The integral in this expression, to within the factor $1/2\pi$, defines the scattering length for the distorting potential in the Born approximation. Therefore, recall that the following estimate is valid for the level shift in the nonresonant case: $\Delta\kappa^2_{ns} \equiv 1/n^2 - \kappa^2_{ns} \leq 4a_s/n^3 \leq 4r_S/n^3$, where r_S is the radius of the distorting short-range potential and a_s is the s-scattering length for this potential.

excited states, causing the extension of the validity range for the adiabatic approximation to increasingly low magnetic field strengths.

(2) The results for the odd $n = 1^-$ (or $2p$) state confirm the remarks made after formula (15), and they hardly require any additional comment.

However, the even $n = 2^+$ ($2s$) state is of much greater interest. As we see from Table 2, the corresponding level is strongly shifted relative to the unperturbed Coulomb levels, $E_n = -1/2n^2$, and lies almost halfway between the levels with the principal quantum numbers $n = 1$ and 2 ($\tilde{\kappa}_{12}^2 = 0.625$ corresponds to this level location). The situation for more highly excited even levels is similar. Thus, according to formula (12), we have $\kappa^2 = 0.17471$ and 0.18876 for the $n = 3^+$ level at $H/c = 10^2$ and 10^3, respectively, while $\tilde{\kappa}_{23}^2 = 0.18056$.

Let us discuss the cause of the so different patterns of the shifts in even and odd levels in a one-dimensional symmetric potential $U_{\text{eff}}(|z|)$ and the relation of our results to the Zeldovich effect. As was shown in [3], large *ns*-level shifts in the three-dimensional short-range Coulomb problem are possible only in the case of a strong distorting short-range potential in which there is an intrinsic shallow, real or virtual, *s* level (so that the scattering of slow particles by this potential is resonant). In the remaining cases, the Coulomb level shifts are small even if there are intrinsic deep (on the atomic scale) levels of the discrete spectrum in the distorting potential. In the one-dimensional case, the wave functions of the even and odd states satisfy the same Schrödinger equation (4) on the semi-axis $r \equiv |z| \geq 0$ but different boundary conditions at point $r = 0$: $\chi^{(-)}(0) = 0$ for the odd levels and $\chi^{(+)\prime}(0) = 0$ for the even levels [in this case, $\chi^{(+)}(0) \neq 0$]. The match between the odd-level spectrum in a symmetric one-dimensional potential and the *ns*-level spectrum in the corresponding centrally symmetric three-dimensional potential has already been noted above. The normalized wave functions in these cases are related by $\psi_{ns}(r) = \chi_n^{(-)}(r)/\sqrt{2\pi}\,r$, so $\psi_{ns}(0) < \infty$ and the smallness of the odd-level shifts relative to the Coulomb levels was explained by the weakness of the Coulomb potential distortion.[4]

This analogy does not hold for even states, because now $\tilde{\psi}_{ns}(r) = \chi_n^{(+)}(r)/r \propto 1/r \longrightarrow \infty$ as $r \longrightarrow 0$ and these singular solutions of the Schrödinger equation are usually excluded from the analysis except for the zero-radius three-dimensional potential. Recall that this potential, localized at point $r = 0$, is determined by the superposition of the following boundary condition [11, 12] on the wave function:

$$\frac{d\ln\chi(r)}{dr} = -\kappa_0,$$
$$\text{or } \tilde{\psi}(r) \approx \text{const}\left(\frac{1}{r} - \kappa_0 + o(r)\right), \text{ for } r \longrightarrow 0, \tag{18}$$

where κ_0 defines the energy of the real (for $\kappa_0 > 0$) or virtual (for $\kappa_0 < 0$) *s* level $E_0 = -\hbar^2\kappa_0^2/2m$ that exists in this potential.

It can now easily be seen that the solutions $\tilde{\psi}_{ns}(r) = \chi^{(+)}(r)/\sqrt{2\pi}\,r$ of the three-dimensional Schrödinger equation for the *s* states with the potential $U(r)$ that satisfy the boundary condition (18) with $\kappa_0 = 0$ are uniquely related to the even solutions $\chi_n^{(+)}(|z|)$ of the Schrödinger equation for a symmetric one-dimensional potential $U(|z|)$ for which $\chi_n^{(+)}(0) = \text{const} \neq 0$ and $\chi^{(+)\prime}(0) = 0$. Thus, in this case, the spherically symmetric potential is the superposition of the potential $U(r)$ [in our problem, this is the effective potential $U_{\text{eff}}(r)$] and the zero-radius (at $r = 0$) potential with $\kappa_0 = 0$.

Significantly, the case with $\kappa_0 = 0$ implies that this zero-radius potential models the strong short-range potential at the time when a bound state (with a zero binding energy) emerges in it; the scattering length (nonrenormalized by the effective potential) is $a_0 = \kappa_0^{-1} = \infty$. This property of the short-range potential that distorts the three-dimensional Coulomb potential is required for the Zeldovich effect to arise.[5]

To generalize our results to single-electron ions with a nuclear charge Ze, the substitutions $e \longrightarrow \sqrt{Z}e$ and $H \longrightarrow H/\sqrt{Z}$ should be made in them by writing the corresponding formulas in standard units.

I thank V.S. Popov and V.D. Mur for helpful discussions and remarks. This study was supported in part by the Russian Foundation for Basic Research (project no. 01-02-16850).

REFERENCES

1. Jang-Haur Wang and Chen-Shiung Hsue, Phys. Rev. A **52**, 4508 (1995).
2. L. D. Landau and E. M. Lifshitz, *Course of Theoretical Physics*, Vol. 3: *Quantum Mechanics: Non-Relativistic Theory*, 5th ed. (Fizmatlit, Moscow, 2002; Pergamon, New York, 1977).
3. Ya. B. Zel'dovich, Fiz. Tverd. Tela (Leningrad) **1**, 1637 (1959) [Sov. Phys. Solid State **1**, 1497 (1959)];

[4] As we noted, $U_{\text{eff}}(|z|) + 1/|z| > 0$, so the distorting potential is repulsive and, hence, it cannot be resonant.

[5] A weak distortion of the Coulomb potential in $U_{\text{eff}}(r)$ does not change the resonant pattern of the interaction associated with the zero-radius potential.

Ya. B. Zel'dovich, *Selected Papers. Particles, Nuclei, Universe* (Nauka, Moscow, 1985).

4. V. S. Popov, Zh. Éksp. Teor. Fiz. **60**, 1228 (1971) [Sov. Phys. JETP **33**, 665 (1971)].
5. A. E. Kudryavtsev, V. E. Markushin, and I. S. Shapiro, Zh. Éksp. Teor. Fiz. **74**, 432 (1978) [Sov. Phys. JETP **47**, 225 (1978)].
6. A. E. Kudryavtsev and V. S. Popov, Pis'ma Zh. Éksp. Teor. Fiz. **29**, 311 (1979) [JETP Lett. **29**, 280 (1979)].
7. V. S. Popov, A. E. Kudryavtsev, and V. D. Mur, Zh. Éksp. Teor. Fiz. **77**, 1727 (1979) [Sov. Phys. JETP **50**, 865 (1979)]; Zh. Éksp. Teor. Fiz. **80**, 1271 (1981) [Sov. Phys. JETP **53**, 650 (1981)].
8. B. M. Karnakov, A. E. Kudryavtsev, V. D. Mur, and V. S. Popov, Zh. Éksp. Teor. Fiz. **94**, 65 (1988) [Sov. Phys. JETP **67**, 1333 (1988)].
9. I. S. Gradshteĭn and I. M. Ryzhik, *Table of Integrals, Series, and Products*, 4th ed. (GIFML, Moscow, 1962; Academic, New York, 1980).
10. H. Hasegawa and R. E. Howard, J. Phys. Chem. Solids **21**, 179 (1961).
11. A. I. Baz', Ya. B. Zel'dovich, and A. M. Perelomov, *Scattering, Reactions and Decays in Nonrelativistic Quantum Mechanics*, 2nd ed. (Nauka, Moscow, 1971; Israel Program for Scientific Translations, Jerusalem, 1966).
12. Yu. N. Demkov and V. N. Ostrovskiĭ, *Zero-Range Potentials and Their Applications in Atomic Physics* (Leningr. Gos. Univ., Leningrad, 1975; Plenum, New York, 1988).

Translated by V. Astakhov

JETP Letters, Vol. 77, No. 2, 2003, pp. 74–79. Translated from Pis'ma v Zhurnal Éksperimental'noĭ i Teoreticheskoĭ Fiziki, Vol. 77, No. 2, 2003, pp. 79–84.

The Zeldovich Effect in a Superstrong Magnetic Field

V. S. Popov

Institute for Theoretical and Experimental Physics, ul. Bol'shaya Cheremushkinskaya 25, Moscow, 117218 Russia
e-mail: markina@heron.itep.ru

Received December 24, 2002

It follows from the analysis of the precision numerical calculations of the energy spectrum of a hydrogen atom in a static magnetic field that the Zeldovich effect (rearrangement of the atomic spectrum) in the spectrum of atomic levels is observed at superstrong magnetic fields $B \gtrsim 5 \times 10^{11}$ G. Magnetic fields of such strengths are reached in neutron stars and magnetic white dwarfs. We established a lower bound $B_{\min}$ for the fields required for this effect to occur. © *2003 MAIK "Nauka/Interperiodica".*

PACS numbers: 32.30.-r; 03.65.Ge

1. The specific properties of the discrete spectrum in a Coulomb field distorted at short ($0 < r < r_0$) distances were first considered by Zeldovich [1] in connection with the problem of electron energy levels in an impurity semiconductor with a dielectric constant $\varepsilon \gg 1$. It was shown that at the time ($g = g_0$) when a bound s level emerges in a short-range potential $V_s(r) = -gv(r)$ or if there is a resonance in the scattering of low-energy particles (i.e., a virtual level with a nearly zero energy), a rearrangement of the atomic spectrum occurs: the Coulomb E_{ns} level rapidly drops to $E_{n-1,s}$ ($n = 2, 3, \ldots$), while the ground E_{1s} level falls deeply downward. The width of the rearrangement region (in strong-potential constant g) is $\Delta g/g_0 \sim r_0/a_B \ll 1$.

A similar behavior of the s and p levels in the electronic spectrum was found [2] in the relativistic Coulomb problem with a nuclear charge $Z > 137$, when the $1s_{1/2}$ level disappears from the discrete spectrum into the lower continuum $E < -mc^2$ (Dirac sea) at a critical value of $Z = Z_{cr} \approx 170$. It was pointed out in [3] that this effect could manifest itself in nuclear level shifts of the lightest hadron atoms ($\bar{p}p$, K^-p, and others). It was noted that the level shift could be positive ($\Delta E_{ns} > 0$; i.e., the level is forced upward), although the short-range potential V_s that produces these shifts is attractive. The following specific model potentials V_s were used in these calculations: a square potential well $v(r) = \theta(r_0 - r)$ [1–3], a parabolic potential corresponding to a constant electric-charge volume density inside the nucleus [2], and separable finite-rank potentials [4–7]. The general pattern of this phenomenon, which can occur in all systems for which the interaction potential breaks down into two (short- and long-range) parts with highly incommensurable ranges of action and weakly depends on the specific inner potential $V_s(r)$, was outlined in [3, 8] and, in more detail, in the review article [6].

In [9], the Zeldovich effect was considered by using the model-independent equation[1]

$$\lambda + 2[\ln\lambda r_0 + \psi(1 - \lambda^{-1}) + c_0] = a_B/a_s. \qquad (1)$$

This equation defines the ns-level locations for the Coulomb long-range part of the potential ($r > r_0$). Here, $l = 0$, $E = -\lambda^2/2$ is the level energy, $\psi(z) = \Gamma'(z)/\Gamma(z)$ is the logarithmic derivative of the gamma function [12], $c_0 = \ln 2 + 2\gamma = 1.848$, $\gamma = 0.5772$ is the Euler constant, r_0 is the matching point, a_B is the Bohr radius, a_s is the s-scattering length for the potential V_s acting in the range $r < r_0$, and small terms on the order of r_0 and $r_0 \ln r_0$ were omitted in Eq. (1). The validity condition for Eq. (1) is

$$r_0 \ll a_B = \hbar^2/me^2 \qquad (2)$$

(below, $\hbar = m = e = 1$, $c = \alpha^{-1} = 137$, Hartree atomic units). In the problem considered by Zeldovich [1], the fact that $a_B = \varepsilon m/m_{\text{eff}} \gg r_0 \sim 1$ (here, m is the electron mass, $m_{\text{eff}} \ll m$ is the effective electron mass in the lattice, and r_0 is the ion radius) ensures that this condition is satisfied.

Equation (1) shows that the ns-level energies are rigidly coupled to each other and can be expressed in terms of the energy of one of them without requiring the solution of the Schrödinger equation. The properties of Eq. (1) were analyzed in detail by Popov *et al.* [13] in connection with the then available evidence for a large $1s$-level shift in the proton–antiproton atom. In this case, according to Eq. (1), a shallow deuteron-type bound state could exist in the $\bar{p}p$ system, which would be of great interest in nuclear physics. However, it subsequently has become clear that the experimental

[1] See also [10, 11]. Note that the term "Zeldovich effect" was proposed in [6]. The term "rearrangement of the atomic spectrum" is also used.

results [14] are incorrect, the level shifts in the $\bar{p}p$ atom are small, and interest in the Zeldovich effect (at least in the field of nuclear physics) fell sharply.

Recently, Karnakov [15] considered the problem of a hydrogen atom in a superstrong magnetic field $B \gg B_a$, where $B_a = m^2e^3c/\hbar^3 = 2.35 \times 10^9$ G is the atomic unit of magnetic field. This problem is of considerable interest in astrophysics and solid-state physics. Such a field compresses the atom, whose characteristic size in the direction transverse to the field is equal to the Landau radius $a_H = \sqrt{\hbar/m\omega_H} = \sqrt{c\hbar/eB}$. In this case, $a_H/a_B = 1/\sqrt{\mathcal{H}}$, where we introduce the reduced field $\mathcal{H} = B/B_a$ and a_H for $\mathcal{H} \gg 1$ acts as the cutoff radius of the Coulomb potential, which is small compared to the Bohr radius a_B. Therefore, it is not surprising that, in this limit, an equation of type (1) is obtained for the energy spectrum of hydrogen atom, in which the specific relation between r_0 and a_B depends on the quantum numbers n_ρ and m [16, 17] for the electron motion in a uniform magnetic field. In particular, for the $n_\rho = m = 0$ states, we have

$$\frac{r_0}{a_B} = \exp\left(-\frac{1}{2}(\ln 2 + \gamma)\right)\frac{a_H}{a_B} = 0.5298/\sqrt{\mathcal{H}}, \quad (3)$$

Eq. (1) takes the form [15]

$$\lambda + 2[\ln\lambda + \psi(1 - \lambda^{-1})] = \ln\mathcal{H} - (3\gamma + \ln 2) \equiv \xi, \quad (4)$$

and condition (2) is satisfied if $\mathcal{H} \gg 1$. The Hamiltonian spectrum is described by the formula [16]

$$E_{n_\rho n_f m \sigma_z} = \left[n_\rho + \frac{1}{2}(m + |m| + 1 + \sigma_z)\right]\mathcal{H} - \frac{1}{2}\lambda^2, \quad (5)$$

where $n_f = 0, 1, \ldots$ is the quantum number for the longitudinal (along $\mathcal{H}$) electron motion, $\sigma_z = \pm 1$, $\lambda = \lambda_{n_\rho n_f |m|}$, the term $-\lambda^2/2$ in Eq. (5) gives the binding energy reckoned from the corresponding Landau level and due to the action of the attractive Coulomb potential, and the field B is directed along the z axis. An equation of type (4) with a constant dependent on n_ρ and $|m|$ is obtained for determining λ.

This equation determines the level energy in a given field $\mathcal{H}$ or (more importantly, e.g., for astrophysics) the magnetic field strength via the measured level shift. It is identical to the corresponding equation in the theory of a $\bar{p}p$ atom [13], in which $\xi = a_B/a_{cs}$, where a_{cs} is the nuclear Coulomb low-energy $\bar{p}p$-scattering length. This shows that the Zeldovich effect must be observed in the hydrogen atomic level spectrum for $\mathcal{H} \gg 1$. The physical cause of this effect is clear: the ground 1*s* level of the atomic spectrum that fell deeply downward (its binding energy for $\mathcal{H} > 500$ exceeds the ionization potential of the hydrogen atom by several orders of magnitude) acts as a quasinuclear state *Qs* perturbing the Coulomb spectrum (see Fig. 1 in [9]).

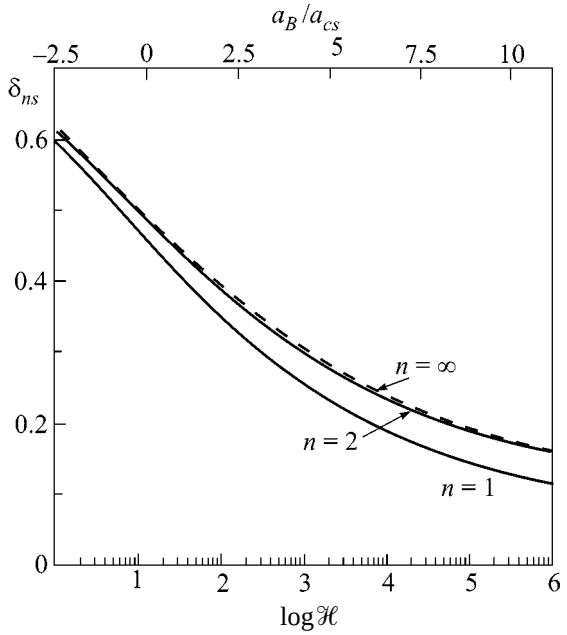

Fig. 1. Quantum defects for *ns* levels versus $\xi = a_B/2a_{cs}$ or versus reduced magnetic field $\mathcal{H}$. The solid curves are for the lower levels with $n = 1$ and 2; the dashed curves are for $n \gg 1$.

2. The following question arises: what can be said about the Zeldovich effect on the basis of available experimental data? Magnetic fields $B \gg B_a$ are encountered in astrophysics (magnetic white dwarfs, neutron stars), but here we must wait for the opinion of specialists. In addition, there are numerous studies in which the Schrödinger equation for a hydrogen atom in a uniform magnetic field was solved on a computer with a high accuracy (up to 10 decimal digits) for $\mathcal{H} \leq 10^5$ or $B \lesssim 2 \times 10^{14}$ G. The results of these computations are in close agreement (see [18, 19] and references therein). We use these data by treating them as the results of a numerical experiment. First, however, a few words should be said about some distinguishing properties of the Zeldovich effect.

Previously, it has already been noted [9] that the most suitable variable for describing the Zeldovich effect is not the energy E or momentum of the bound state $\lambda = \sqrt{-2E}$ but the quantity

$$\nu = Z/\lambda = \sqrt{Z^2me^4/2\hbar^2|E|} \quad (6)$$

(if the potential $V(r) = -Z/r$ for $r > r_0$). In atomic physics, this variable is called the effective principal quantum number and is denoted by n^*. A characteristic property of the Zeldovich effect is that the values of ν_n for the entire series of atomic *ns* levels are highly periodic in n. This can be seen from Fig. 1, which shows the

Table 1

n	$\xi = 0$ ($\mathcal{H} = 11.3$)			$\mathcal{H} = 3120$	
	ν_n	δ_1/δ_∞	ρ_n	ν_n	ρ_n
1	0.46957	0.9391	–	0.2179	–
2	1.49637	0.9927	0.738	1.2649	0.500
3	2.49867	0.9973	0.641	2.2668	0.399
4	3.49932	0.9986	0.606	3.2672	0.359
5	4.49958	0.9992	0.583	4.2674	0.337
10	9.49991	0.9998	0.539	9.2676	0.300
$n \longrightarrow \infty$	$n - 1/2$	1.0000	0.500	$n - 0.732$	0.271

quantum defects $\delta_n = \nu_n - (n-1)$, $n = 1, 2, \ldots$ calculated from Eqs. (4) and (1). The change in δ_n from $n = 2$ to $n = \infty$ (for a given $\mathcal{H}$) does not exceed 1%, which characterizes the degree of ν_n periodicity in the atomic spectrum range, i.e., at $\nu > 1$. At the same time, for the ground 1*s* level, which falls arbitrarily deep with increasing $\mathcal{H}$, this change is larger. Thus, the δ_1/δ_∞ ratio changes from 0.95 to 0.75 as $\mathcal{H}$ changes from 100 to 10^5; see Table 1 that refers to the exact resonance $a_{cs} = \infty$ (the level formation time with allowance made for the Coulomb interaction), which corresponds to $\xi = 0$ or $\mathcal{H} \approx 11.3$. In this case, when $n \longrightarrow \infty$, $\nu_n = n - 1/2$ and $\delta_n = 1/2$. Table 1 also gives the ν_n and ρ_n values for $\rho_2 = 1/2$; i.e., the binding energy of the 2*s* level is $\varepsilon_{2s} = 5/16$ a.u. = 8.5 eV.

The ν_n periodicity can be easily explained if we write Eq. (1) or (4) in the following form by using the identity $\psi(1-z) = \pi\cot\pi z + \psi(z)$ [12]:

$$\cot\pi\nu - d(\nu) = \frac{\xi}{2\pi} = \frac{1}{2\pi}(\ln\mathcal{H} - 2.425). \qquad (7)$$

The function $d(\nu)$ is numerically small in the range of the atomic spectrum:

$$d(\nu) = \frac{1}{\pi}\left[\ln\nu - \psi(\nu) - \frac{1}{2\nu}\right] = \begin{cases} 0.0246, & \nu = 1 \\ 0.0065, & \nu = 2 \\ 1/12\pi\nu^2, & \nu \longrightarrow \infty. \end{cases}$$

Hence, for $n \gg 1$,

$$\delta_n = \delta_\infty - \frac{\sin^2\pi\delta_\infty}{12\pi^2 n^2} + \ldots, \quad \delta_\infty = \frac{1}{\pi}\operatorname{arccot}\xi \qquad (8)$$

($0 < \delta_\infty < 1$), suggesting a ν_n periodicity for large *n*. As we see from Fig. 1, this periodicity extends up to $n = 2$.

Occasionally, it is suggested that the rearrangement of the atomic spectrum shows up most clearly in level shifts. Of course, this is qualitatively true, but quantitatively the atomic level shifts do not obey such a simple law as do ν_n and δ_n. Indeed, consider the relative shift of the *ns* level

$$\rho_n = \frac{E_{ns} - E_{n-1}^{(0)}}{E_n^{(0)} - E_{n-1}^{(0)}} = \frac{n^2(2n-2+\delta_n)}{(2n-1)(n-1+\delta_n)^2}\delta_n, \quad n \geq 2 \qquad (9)$$

($E_n^{(0)} = -Z^2/2n^2$). In contrast to δ_n, the dependence of ρ_n on the level number is significant, as can be seen from Table 1. Similarly, if $\rho_n = 1/2$, i.e., if the *ns* level is exactly halfway between the neighboring Coulomb levels, then the quantum defect δ_n for it is by no means equal to 0.5:

$$\delta_n = (n-1)\left[n\sqrt{\frac{2}{2n^2-2n+1}} - 1\right] = \begin{cases} 0.265, & n = 1 \\ 0.353, & n = 3 \end{cases} \qquad (10)$$

and $\delta_n = 1/2 - 3/8n + \ldots$ for $n \gg 1$. Only for highly excited states are ρ_n and δ_n close to each other:

$$\rho_n = \delta_n + \frac{3\delta_n(1-\delta_n)}{2n} + O\left(\frac{1}{n^2}\right), \quad n \gg 1, \qquad (9')$$

with $\delta_n < \rho_n < 1$.

Thus, the constancy of the quantum defects δ_n, $2 \leq n < \infty$, is a reliable indicator of the Zeldovich effect in the atomic level spectrum (in a short-range Coulomb field).

Note that our definition of the quantum defect slightly differs from that in atomic physics, where it is commonly assumed that $\nu_n = n - \Delta_l$ (the Rydberg correction Δ_l is virtually independent of the principal quantum number *n*). In our case, it is convenient to reckon δ_{nl} not from the initial level *n* in a free ($\mathcal{H} = 0$) atom but from the limiting value of n_f to which ν tends as $\mathcal{H} \longrightarrow \infty$ in the Schrödinger equation (which corresponds to the level number in a one-dimensional Coulomb potential [17]).

The quantum defects δ_{nl} can easily be calculated by using the binding energies ε_{nl} from [18, 19]. Following [19], when classifying the states, we number them by the quantum numbers n and l for a free ($\mathcal{H} = 0$) atom. However, n_ρ, m, n_f, and P, where n_ρ and m describe the rapid motion around the magnetic field, n_f is the level number in a one-dimensional Coulomb potential (the slow electron motion along $\mathcal{H}$), and $P = \pm 1$ is the wavefunction parity about the reflection $z \longrightarrow -z$, are good quantum numbers for $\mathcal{H} \gg 1$. In this case,

$$n_f = \lim_{\mathcal{H}\to\infty} \nu_{nl}(\mathcal{H}), \quad \delta_{nl} = \nu_{nl} - n_f. \tag{11}$$

Next, we assume that $n_\rho = m = 0$, because the energies of only these states were calculated in [19].

There is the following correspondence between the quantum numbers (n, l) and n_f^P: $1s \longrightarrow 0^+$, $2s \longrightarrow 1^+$, $3d \longrightarrow 2^+$, and $3s \longrightarrow 3^+$ for even states and $2p \longrightarrow 1^-$, $3p \longrightarrow 2^-$, $4f \longrightarrow 3^-$, etc., for odd states with increasing magnetic field. With the exception of the $3s$ state (see below), the relation $n_f = n - 1$ holds.

The δ_{nl} values are shown in Fig. 2. Its comparison with Fig. 1 indicates that the Zeldovich effect occurs at $\mathcal{H} > \mathcal{H}_{\min} \sim 100$ for even states and, starting from $\mathcal{H}_{\min} \approx 1$, for odd states. The dashed line in Fig. 1 indicates the limiting curve $n \longrightarrow \infty$ constructed from Eq. (8). The difference between this curve and the curve for the $2s$ level closely corresponds to Fig. 1. At the same time, for $\mathcal{H} < \mathcal{H}_{\min}$, even the arrangement of the $\delta_{nl}(\mathcal{H})$ curves differs sharply from the arrangement shown in Fig. 1 and characteristic of the Zeldovich effect. Note that for the ns levels, $\delta_n \propto 1/\ln(\mathcal{H}/\ln^2\mathcal{H})$ when $\mathcal{H} \longrightarrow \infty$.

A comment is required on the $3s$ and $3d$ states. In the absence of a magnetic field, the three degenerate[2] $3s$, $3p$, and $3d$ levels, of which $3p$ has a negative parity and does not interact with the other two states, while $3s$ and $3d$ are the states with identical symmetry, correspond to the principal quantum number $n = 3$. These terms mutually pull apart (see Fig. 3), because their crossing would be in conflict with the Wigner–Neumann theorem.[3] As we see from Fig. 3, the numerical calculations brought only to $\mathcal{H} = 10$ in this case [19] are in satisfactory agreement with the asymptotic equation (4), confirming that $n_f = n - 1 = 2$ for the $3d$ state and $n_f = n = 3$ for the $3s$ state. That the $3d$ level lies below the $3s$ level probably stems from the fact that its radial wave function has no nodes ($l = n - 1$). For clarity, we would like to continue numerical calculations of the energies ε_{3s} and ε_{3d} at least up to $\mathcal{H} = 100$.

[2] This is the so-called random degeneracy due to the hidden symmetry group $SO(4)$ of the Coulomb field.

[3] See §79 in [16]. Similarly, one might expect that the $4s$, $4d$ (even) and $4p$, $4f$ (odd) levels interact with one another. Indeed, the $\delta_{4f}(\mathcal{H})$ curve in Fig. 2 clearly shows some feature.

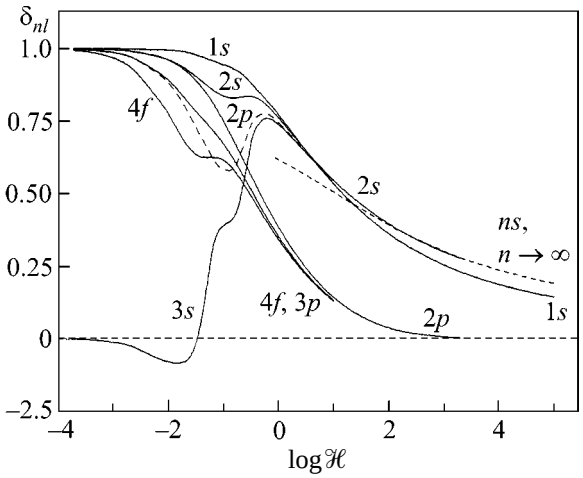

Fig. 2. The numerically calculated quantum defects are represented by the solid curves. The hydrogen atomic states, according to their classification in the absence of a magnetic field, are indicated near these curves (the dashed curve refers to the $3d$ state).

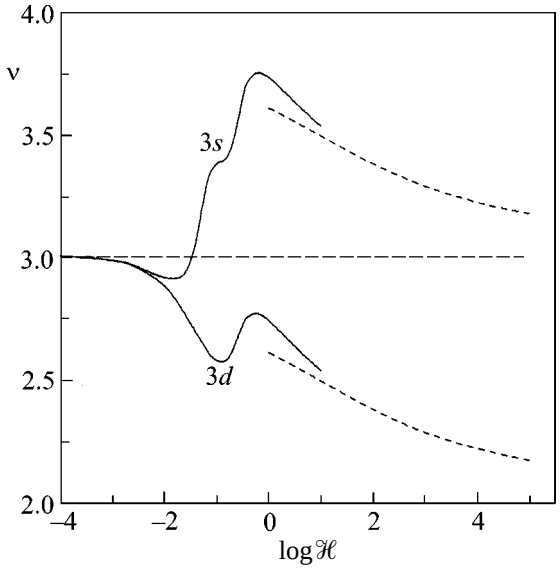

Fig. 3. $\nu = Z/\lambda$ versus magnetic field for the $3s$ and $3d$ states: the solid curves were recalculated from the data in [19] and the dashed curves were recalculated from the asymptotic equation (4).

The quantum defect δ_{1s} for the ground level differs markedly from the remaining δ_{ns} (see Fig. 1). This quantity can also be used as a kind of test for the Zeldovich effect. Consider the ratio

$$R_{12} = \delta_1/\delta_2 = \left(\sqrt{\varepsilon_1/\varepsilon_2} - \sqrt{2\varepsilon_1}\right)^{-1}, \tag{12}$$

where $\varepsilon_{1,2}$ are the binding energies of the two lower $1s$ and $2s$ levels in atomic units $me^4/\hbar^2 = 27.121$ eV. In Fig. 4, curve *1* was recalculated from the numerical

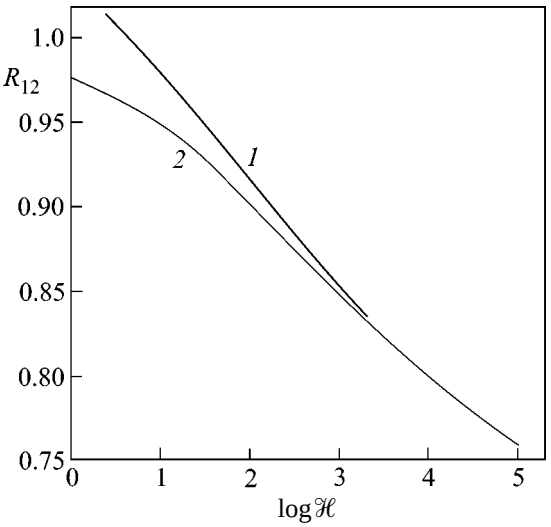

Fig. 4.

data [19] and curve *2* corresponds to the solution to Eq. (4). These curves approach each other at $\mathcal{H} \gtrsim 100$, where a small parameter $r_0/a_B < 1/20$ appears in the problem. In this range, the shift of the atomic 2*s* level is related to the location of the ground 1*s* level by the expression specific to the Zeldovich effect. This fact can be used to analyze astrophysical data. If necessary, one can also turn to the ratios $R_{1n} = \delta_1/\delta_n$, the formulas for which are similar to (12).

The $\delta_{nl}(\mathcal{H})$ curves shown in Fig. 2 for three odd states indicate that the Zeldovich effect can exist for them in the range $1 \lesssim \mathcal{H} \lesssim 10^3$. In this case, there is no deep quasinuclear (or 1*s*, as in the case of even states) level in the system. However, 2*p*, which drags higher-lying levels with a negative parity while dropping with increasing $\mathcal{H}$, acts as this level. In the above $\mathcal{H}$ range, the quantum defects for the 2*p*, 3*p*, and 4*f* states are close, resulting in a characteristic ν_{nl} periodicity. However, for $\mathcal{H} > 1000$, the shifts of these levels are very small. Thus, for the 2*p* level at $\mathcal{H} = 2000$, we have $\varepsilon_{2p} = 0.991189\ldots$ (in rydbergs; see Table II in [19]) and $\delta_{2p} = \varepsilon_{2p}^{-1/2} - 1 = 0.00443$. In this case, the 2*p*-level shift accounts for only 1.2% of the separation between the unperturbed levels with $n = 1$ and 2, while, for $\mathcal{H} > 10^4$, it is even smaller and can hardly be measured experimentally.

3. Below, we make several concluding remarks.

(1) Table 2 gives the binding energies of the first two *s* levels, their quantum defects, and ratios (12). We took ε_1 from [19] and calculated ε_2 from Eq. (4)—a procedure that is inverse to that used previously in [9, 13]. In this case, the relative shift of the 2*s* level (9) changes from $\rho_2 = 0.584$ at $\mathcal{H} = 400$ to 0.393 at $\mathcal{H} = 10^5$. For $\varepsilon_2 = 8.5$ eV ($\mathcal{H} \approx 3100$), this level lies halfway between the unshifted $E_n^{(0)}$ levels with $n = 1$ and 2.

(2) There is a significant difference in the Zeldovich effects for three-dimensional local potentials and in the problem with a magnetic field. In the former case, the rearrangement of the spectrum can be repeated several times as the coupling constant g increases: thus, for a square potential well, this occurs at $g \approx g_N = (2N + 1)^2\pi^2\hbar^2/8r_0^2$, $N = 0, 1, 2, \ldots$. In the latter case, only the ground 1*s* level can become deep with increasing $\mathcal{H}$, while the remaining levels lie in the range $\nu > 1$ (a typical property of a one-dimensional Coulomb potential [17]). Therefore, only one cycle of spectrum rearrangement occurs in a magnetic field (however, there is a cycle for each pair of quantum numbers n_ρ and $|m|$).

(3) For $\mathcal{H} \gg 1$, the size of the atom in the direction transverse to the field is equal to the Landau radius a_H, and the wave function in the longitudinal direction can be expressed in terms of the Whittaker function:

$$\chi_\lambda(z) = \sigma \mathrm{const} W_{\nu,\,1/2}(2\lambda|z|), \quad -\infty < z < \infty, \qquad (13)$$

where $\nu = 1/\lambda$ and $\sigma = 1$ for even and $\sigma = \mathrm{sgn} z$ for odd states, respectively. Since the integrals in the normalization and in the expression for the rms radius $a_\parallel = \langle z^2 \rangle^{1/2}$ were calculated in [13], we can derive an analytic formula for $a_\parallel$; this formula was omitted here because it is cumbersome. Note only that the ratio $s =$

Table 2

$\mathcal{H}$	B, G	ε_1	ε_2	δ_1	δ_2	R_{12}
400	9.4(11)	159.2	7.64	0.2923	0.3339	0.875
1000	2.35(12)	208.4	8.05	0.2554	0.3001	0.851
2000	4.70(12)	253.1	8.33	0.2318	0.2783	0.833
5000	1.18(13)	323.0	8.67	0.2052	0.2524	0.813
1.0(4)	2.35(13)	384.6	8.91	0.1880	0.2354	0.798
5.0(4)	1.18(14)	559.8	9.41	0.1559	0.2025	0.770
1.0(5)	2.35(14)	649.8	9.59	0.1447	0.1907	0.759

Note: ε_1 and ε_2 are the binding energies of the 1*s* and 2*s* levels (for $n_\rho = m = 0$) in eV and $\delta_{1,\,2}$ are their quantum defects. Notation: $a(b) \equiv a \times 10b$.

$a_\parallel/a_H$, which characterizes the shape of the atom (the electron localization region), is, respectively, $s = 7.1$, 15.6, and 37 at $\mathcal{H} = 1000$, 10^4, and 10^5 for the 1*s* level and $s = 90$, 255, 760 for the 2*s* level. Thus, the atom is cigar-shaped (for 1*s* at $\mathcal{H} \lesssim 10^4$) or even needle-shaped (for *ns* states, $n \geq 2$). Its longitudinal size decreases with increasing $\mathcal{H}$, particularly for the 1*s* level, for which $a_\parallel/a_B = 0.225$, 0.156, and 0.116 at the above strengths of the reduced field $\mathcal{H}$. For excited states, $a_\parallel \propto n^2$.

(4) For $\mathcal{H} \sim 10^4$–10^5, the Landau level energy exceeds the electron rest energy:

$$\hbar\omega_H/mc^2 = B/B_{\rm cr},$$
$$a_H = \frac{\lambda_e}{2\pi}\sqrt{\frac{B_{\rm cr}}{B}}, \quad \lambda_e = \frac{2\pi\hbar}{mc}, \tag{14}$$

where $B_{\rm cr} = m^2c^3/e\hbar$ is the critical or Schwinger field characteristic of quantum electrodynamics (numerically, $B_{\rm cr} = 4.41 \times 10^{13}$ G or $\mathcal{H}_{\rm cr} = 1.88 \times 10^4$). Therefore, relativistic corrections should be applied to the level energies for $\mathcal{H} \gtrsim 10^4$.

Thus, the quantum defects of *ns* levels extracted from previous numerical calculations suggest that the Zeldovich effect must manifest itself in the energy spectrum of a hydrogen atom in superstrong magnetic fields, $\mathcal{H} \gtrsim 100$ or $B \gtrsim 10^{11}$ G. Figures 2–4 clearly show how this effect occurs with increasing $\mathcal{H}$; we see that the effect is essentially observable (in numerical experiment). A confirmation of this result by direct astrophysical observations would be of great interest.

I thank B.M. Karnakov for information on the paper [15] and for helpful remarks, S.I. Blinnikov and V.D. Mur for discussions, and S.G. Pozdnyakov for help in the numerical calculations. I am also grateful to M.I. Vysotskiĭ, Yu.A. Simonov, and K.A. Ter-Martirosyan for a discussion of the results. This study was supported in part by the Russian Foundation for Basic Research (project no. 01-02-16850).

REFERENCES

1. Ya. B. Zeldovich, Fiz. Tverd. Tela (Leningrad) **1**, 1637 (1959) [Sov. Phys. Solid State **1**, 1497 (1959)].
2. V. S. Popov, Zh. Éksp. Teor. Fiz. **60**, 1228 (1971) [Sov. Phys. JETP **33**, 665 (1971)].
3. A. E. Kudryavtsev, V. E. Markushin, and I. S. Shapiro, Zh. Éksp. Teor. Fiz. **74**, 432 (1978) [Sov. Phys. JETP **47**, 225 (1978)].
4. H. van Haeringen, C. V. M. van der Mee, and R. van Wageningen, J. Math. Phys. **18**, 941 (1977).
5. H. van Haeringen and L. P. Kok, Phys. Rev. C **24**, 1827 (1981).
6. A. M. Badalyan, L. P. Kok, M. I. Polikarpov, and Yu. A. Simonov, Phys. Rep. **82**, 31 (1982).
7. L. P. Kok, J. W. de Maag, H. H. Brower, and H. van Haeringen, Phys. Rev. **26**, 2381 (1982).
8. D. A. Kirzhnits and F. M. Pen'kov, Zh. Éksp. Teor. Fiz. **82**, 657 (1982) [Sov. Phys. JETP **55**, 393 (1982)].
9. A. E. Kudryavtsev and V. S. Popov, Pis'ma Zh. Éksp. Teor. Fiz. **29**, 311 (1979) [JETP Lett. **29**, 280 (1979)].
10. T. L. Trueman, Nucl. Phys. **26**, 57 (1961).
11. A. I. Nikishov and V. I. Ritus, Zh. Éksp. Teor. Fiz. **52**, 223 (1967) [Sov. Phys. JETP **25**, 145 (1967)].
12. H. Bateman and A. Erdelyi, *Higher Transcendental Functions* (McGraw-Hill, New York, 1953), Vol. 1.
13. V. S. Popov, A. E. Kudryavtsev, and V. D. Mur, Zh. Éksp. Teor. Fiz. **77**, 1727 (1979) [Sov. Phys. JETP **50**, 865 (1979)]; Zh. Éksp. Teor. Fiz. **80**, 1271 (1981) [Sov. Phys. JETP **53**, 650 (1981)].
14. M. Izycki, G. Bakenstoss, *et al.*, Z. Phys. A **297**, 1 (1980).
15. B. M. Karnakov, Pis'ma Zh. Éksp. Teor. Fiz. (in press).
16. L. D. Landau and E. M. Lifshitz, *Course of Theoretical Physics*, Vol. 3: *Quantum Mechanics: Non-Relativistic Theory*, 3rd ed. (Nauka, Moscow, 1974; Pergamon, New York, 1977).
17. V. M. Galitskiĭ, B. M. Karnakov, and V. I. Kogan, *Problems on Quantum Mechanics* (Nauka, Moscow, 1992).
18. S. P. Goldman and Z. Chen, Phys. Rev. Lett. A **67**, 1403 (1991); Phys. Rev. A **45**, 1722 (1992).
19. Jang-Haur Wang and Chen-Shiung Hsue, Phys. Rev. A **52**, 4508 (1995).

Translated by V. Astakhov

JETP Letters, Vol. 77, No. 2, 2003, pp. 80–83. Translated from Pis'ma v Zhurnal Éksperimental'noĭ i Teoreticheskoĭ Fiziki, Vol. 77, No. 2, 2003, pp. 85–88.

Smoothing of Interfacial Micron-Scale Roughness in a Ni/C X-ray Multilayer Mirror

N. V. Kovalenko[1], S. V. Mytnichenko[2]*, and V. A. Chernov[3]

[1] *Budker Institute of Nuclear Physics, Siberian Division, Russian Academy of Sciences, Novosibirsk, 630090 Russia*

[2] *Institute of Solid-State Chemistry and Mechanochemistry, Siberian Division, Russian Academy of Sciences, Novosibirsk, 630128 Russia*

**e-mail: s.v.mytnichenko@inp.nsk.su*

[3] *Boreskov Institute of Catalysis, Siberian Division, Russian Academy of Sciences, Novosibirsk, 630090 Russia*

Received November 25, 2002

Correlation between the roughness of neighboring interfaces (roughness cross correlation) in a Ni/C X-ray multilayer mirror (XMM) prepared by laser ablation was studied by measuring X-ray diffuse scattering (XDS). The XDS intensities in the vicinity of the first Bragg reflection were measured at different photon energies: slightly below (8.325 keV) and slightly above (8.350 keV) the nickel photoabsorption K edge. The effective screening of the contribution from the deep layers to the XDS cross section due to the strong damping of the wave field at a photon energy higher than the photoabsorption edge allowed information on the character of the in-depth roughness cross correlation in the sample to be obtained. In particular, the characteristic lateral correlation length of the roughness was 0.35 μm at a photon energy of 8.325 keV (the contribution to the XDS cross section of the entire XMM volume), and it increased to 0.4 μm at a photon energy of 8.350 keV (predominantly the contribution from the upper layers). These data give direct evidence for the mechanism of smoothing of the interfacial roughness in the process of Ni/C XMM growth on anomalously large (up to micron) spatial scales. It was found that only rough large-scale defects with sizes of ≥10 μm are reproduced reasonably well from layer to layer. The processes of viscous flow and (or) reevaporation of high-energy target ions during deposition, which is characteristic of the laser method of XMM preparation, may serve as a possible explanation of the observed phenomenon. © *2003 MAIK "Nauka/Interperiodica".*

PACS numbers: 68.55.Jk; 61.10.Eq

The possibility of smoothing the interfacial roughness in the process of growth of multilayer thin films, in particular, an X-ray multilayer mirror (XMM), is a well-known fact. Moreover, if this smoothing were impossible, the problem of fabricating an XMM with more or less acceptable diffraction characteristics would become much more complicated. The smoothing of the interfacial roughness in an XMM can be observed in magnetron [1] and laser [2] sputtering, as well as in thermal sputtering with the use of additional ion polishing [3–6].

The most consistent phenomenological model of the evolution of interfaces in the process of XMM growth was proposed in [7], where the amplitude of roughness of the mth interface in the reciprocal space f_m was expressed in terms of the amplitude of the antecedent interface f_{m-1} as follows:

$$f_m(s) = h_m(s) + a_m(s) f_{m-1}(s), \quad (1)$$

where $a_m(s)$ is a replication factor of roughness with a spatial frequency s, and $h_m(s)$ is the amplitude of the intrinsic roughness of the mth interface. Note that the intrinsic roughnesses of different layers do not correlate with each other, $\langle h_m h_n \rangle = \delta_{mn} \langle h_m^2 \rangle$. It is evident that the short-wavelength roughness components must be suppressed more efficiently ($a_m(s) \longrightarrow 0$ at $s \longrightarrow \infty$), whereas very large-scale roughness must be completely replicated from layer to layer ($a_m(s) \longrightarrow 1$ at $s \longrightarrow 0$). Thus, it is physically reasonable to choose the replication factor in the form

$$a_m(s) = \exp(-M(s)), \quad (2)$$

where $M(s)$ is a certain polynomial whose form and coefficients are determined by possible physical and chemical processes that proceed during the XMM growth. In [8], it was taken into account that an atom in the "soft" deposition process can be displaced to a certain distance that coincides with its sizes in the order of magnitude. In [7, 9, 10], this approach was developed mathematically, and the following equation was obtained for $a_m(s)$:

$$a_m(s) = \exp(-\nu d_m s^2), \quad (3)$$

where d_m is the layer thickness for the mth interface and ν is the diffusion length. The characteristic range of ν is 10^{-3}–1 nm. Hence, according to these works, the smoothing of roughness must occur in the short-wavelength region. Terms proportional to s and s^4 were intro-

duced into $M(s)$ in [11]. As in the previous works, smoothing, according to this work, must occur in the short-wavelength region of the roughness spectrum, except for the smoothing associated with the term $\sim s$, which in any case describes viscous flow in the polishing by ions with high kinetic energies (200–1300 eV). In [12, 13], it was taken into account, by introducing a constant ($\sim s^0$) into $M(s)$, that the adsorbed atoms can travel very long distances over the surface, which results in uniform smoothing everywhere over the spectral region. According to these works, the replication factor does not tend to unity at $s \longrightarrow 0$.

The question of the correctness of particular physical models for the description of the effect of roughness smoothing in the process of XMM growth can be solved if experiments are carried out that allow the replication function $a(s)$ to be measured directly. In spite of the fact that the potentialities of X-ray diffuse scattering (XDS) in studying roughness cross correlation through modeling of angular intensity distributions are widely postulated in the literature, the actual possibility of calculating the $a(s)$ function from XDS data is rather conjectural at least in the case of using conventional experimental schemes. The problems arising are due to the fact that the coherent reproduction of rough interfaces from layer to layer leads to a resonant amplification of XDS, giving rise to a so-called "quasi-Bragg sheet" [7, 14–17] when the modified Bragg condition

$$\lambda = \Lambda(\sin\theta_0 + \sin\theta_1) = 2\Lambda\sin\theta_B,$$

is fulfilled, where λ is the wavelength of the X-ray photon; Λ is the multilayer period; θ_0 and θ_1 are, respectively, the incoming and outgoing angles with respect to the lateral planes; and θ_B is the Bragg angle. Hence, the contribution to the XDS cross section from layer-to-layer correlated roughness is proportional to N^2 (N is the number of bilayers in XMM), and the contribution from the uncorrelated roughness is proportional to N. As a consequence, violations of the complete roughness cross correlation have only a little effect on the intensity of diffuse scattering.

The articles [18, 19], in which XDS was studied in the vicinity of Kiessig modulations, can be mentioned as examples of efforts made to overcome the difficulty indicated above. Because the maximum difference in the behavior of interfaces is reached between the XMM surface and the XMM–substrate interface, this approach provides an increase in the sensitivity of XDS to violations of the complete roughness cross correlation. Giving this approach credit, one should note that both the surface and the XMM–substrate interface are of a unique character, and their behavior may differ significantly from the behavior of internal interfaces. Another possibility of obtaining more reliable data on the character of roughness cross correlation is offered by studying XMM with a small number of layers, where the amplification of diffuse scattering due to coherent reproduction of interfaces is small [20]. It is natural that the class of objects available for investigation becomes strongly restricted in this case.

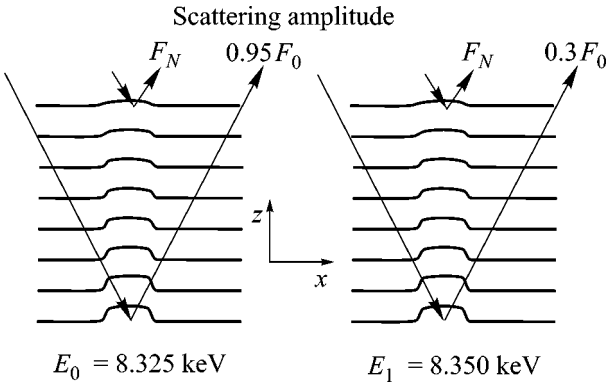

Fig. 1. Comparison of the diffuse scattering amplitude from a Ni/C XMM at photon energies below (8.325 keV) and above (8.350 keV) the nickel atom absorption K edge: in the second case, the contribution to the amplitude of diffuse scattering from rough defects of the lower layers is markedly lower because of effective screening under conditions of hard photoabsorption.

In this work, we used another modification of XDS that, in our opinion, considerably enhances the possibilities of studying the behavior of roughness cross correlation for interfaces in an XMM. The approach proposed is based on a comparative measurement of the intensity of diffuse scattering at photon energies slightly below and slightly above the photoabsorption edge of atoms entering into the XMM composition. Whereas the amplitudes of diffuse scattering from rough interfaces in the first case are approximately equal over the entire XMM volume, the lower interfaces are effectively screened in the second case because of strong photoabsorption (Fig. 1). Measurements of the relative difference in the XDS intensities for the first and the second cases considerably increase the sensitivity of the experiment to violations of the complete roughness cross correlations. In addition, if these measurements are carried out depending on the projection of the momentum transfer in the lateral direction, the behavior of cross correlation can be investigated as a function of lateral spatial scales of roughness.

The Ni/C XMM studied in this work was prepared by laser ablation [2, 21] onto a fused silica substrate with a high degree of polishing with nanodiamonds [22]. A preliminary study of the substrate by X-ray reflectometry ($\lambda = 0.154$ nm) gave a roughness dispersion of ~0.5–0.6 nm. The optical XMM parameters were obtained by modeling the X-ray reflectometry data in the dynamical approximation [23]: the period $\Lambda \approx 5.2$ nm; the ratio of the thickness of nickel layers to period $\beta \approx 0.4$; the density of nickel and carbon layers, respectively, $\rho_{Ni} \approx 8.2$ g/cm^3 and $\rho_C \approx 2.3$ g/cm^3; and the roughness dispersion $\sigma \sim 0.4$–0.5 nm. It should be noted that the roughness dispersion of the XMM

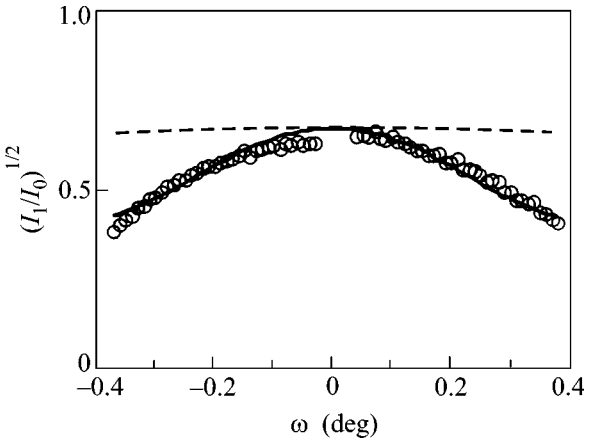

Fig. 2. Experimental data (circles) and theoretical DWBA calculations for the cases of the complete roughness cross correlation (dashed line) and the roughness smoothing (solid line).

proved to be lower than that of the original substrate.[1] Moreover, our previous studies demonstrated [21, 24, 25] that the above value of the XMM roughness dispersion reflects both the true roughness and the presence of mixed layers. An estimation of the true roughness gave a value of ~0.1–0.2 nm [26].

Diffraction experiments were carried out on a triple-axis diffractometer[2] with the use of synchrotron radiation of a VEPP-3 storage ring [27]. The measurements of the XDS intensity were performed at two photon energies (E_0 = 8.325 keV and E_1 = 8.350 keV) with the use of transverse scan (ω scan) through the first Bragg reflection.

The ω profiles obtained experimentally differed in angular width, which corresponds to different lateral characteristic correlation lengths ~0.35 μm at a photon energy of 8.325 keV and ~0.40 μm at a photon energy of 8.350 keV. With regard to the fact that the contribution to diffuse scattering in the first case was due to the interface roughnesses in the entire XMM volume and that the interfaces of the upper layers predominantly work in the second case, the values obtained point to the smoothing of roughness in the sample. The experimental data obtained are presented in Fig. 2 (circles) as the ratios $(I_1/I_0)^{1/2}$ (I_0 and I_1 are the intensities of diffuse scattering at the corresponding photon energies) depending on the diffraction asymmetry angle $\omega = (\theta_0 - \theta_1)/2$, which is directly proportional to the momentum transfer q_x in the lateral direction ($q_x \approx 2k\theta_B\omega$). It is clearly seen in the figure that the experimental data markedly deviate from the theoretical curve (dashed line) calculated in the framework of the distorted-wave Born approximation (DWBA) [17]. The complete roughness cross correlation is assumed to occur in this case. The sign of the deviation corresponds to a decrease in the roughness amplitudes in the process of XMM growth, and the larger the momentum transfer, the stronger the deviation magnitude.

With regard to the fact that the range of lateral sizes of rough defects lies in our measurements in small limits from fractions of micron to several tens of microns, the difference in the characteristic correlation lengths is indicative of smoothing off spatial scales as large as a micron scale. This is clearly seen in Fig. 2, where the solid line represents model calculations in which Eq. (3) is formally used for the replication factor and the intrinsic roughness $h_m(s)$ is neglected. In spite of the apparently good agreement, the obtained parameter $\nu \sim 0.5$ μm exceeds the value expected in [7–10] by three orders of magnitude. At the same time, though smoothing on very large spatial scales is predicted in theoretical works [12, 13], this smoothing must be uniform over the entire roughness spectrum, which also contradicts our experiment. In fact, the ratio of XDS intensities at various photon energies in the close vicinity of the specular Bragg reflection corresponds to the full layer-to-layer reproducibility of rough large-scale defects with sizes of ≥10 μm.

As was already mentioned above, the mechanism of roughness smoothing-out due to viscous flow when polishing by high-kinetic-energy ions was considered in [11]. It was shown that this process leads to smoothing-out on sufficiently large spatial scales. Though the kinetic energy of atoms deposited in laser ablation is significantly lower than the ion energy in polishing, an analogous process of viscous flow can still take place. The possible processes of reevaporation of target atoms during deposition may serve as another variant of explanation of the roughness smoothing on a micron scale. “Splattering” of atoms over the XMM surface may result, on the one hand, in the healing of “valleys” and, on the other hand, in the effective leveling off of “hills” on the XMM surface.

In summary, the structural method of studying the cross correlation of XMM roughness proposed in this work allowed us to observe roughness smoothing on an anomalously large micron scale.

We are grateful to V.A. Bushuev for useful consultations, the personnel of the Siberian Center of Synchrotron Radiation headed by G.N. Kulipanov, and experimenters of the VEPP-3 storage ring for attention and support.

[1] An interesting fact from our experience of fabricating Ni/C XMMs by laser ablation can be mentioned. Although, according to X-ray reflectometry data, the roughness dispersion of original substrates can vary over wide limits, the optical quality of the fabricated Ni/C XMM remains approximately equal. This fact gives clear evidence in favor of strong smoothing of roughness in the process of sputtering.

[2] It can be noted that the use of a secondary collimating crystal in the measurements above the Ni absorption K edge allowed us to avoid a distortion of the experimental data through the excitation of fluorescence radiation. Thus, the fluorescence background measured experimentally was found to be ~10–20 Hz, whereas the desired signal was no less than several kHz.

REFERENCES

1. T. W. Barbee, Opt. Eng. **25**, 893 (1986).
2. S. V. Gaponov, F. V. Garin, S. A. Gusev, *et al.*, Nucl. Instrum. Methods Phys. Res. **208**, 227 (1983).
3. E. Spiller, A. Segmuller, J. Rife, *et al.*, Appl. Phys. Lett. **37**, 1048 (1980).
4. E. Spiller, Appl. Phys. Lett. **54**, 2293 (1989).
5. M. P. Bruijn, P. Chakraborty, H. W. van Essen, *et al.*, Proc. SPIE **563**, 36 (1985).
6. E. J. Puik, M. J. van der Wiel, H. Zeijlemarker, *et al.*, Rev. Sci. Instrum. **63**, 1415 (1992).
7. D. G. Stearns, J. Appl. Phys. **71**, 4286 (1992).
8. S. F. Edwards and D. R. Wilkinson, Proc. R. Soc. London, Ser. A **381**, 17 (1982).
9. D. G. Stearns, Appl. Phys. Lett. **62**, 1745 (1993).
10. E. Spiller, D. Stearns, and M. Krumrey, J. Appl. Phys. **74**, 107 (1993).
11. R. Schlatmann, J. D. Shindler, and J. Verhoeven, Phys. Rev. B **54**, 10880 (1996).
12. V. A. Bushuev and V. V. Kozak, Kristallografiya **42**, 809 (1997) [Crystallogr. Rep. **42**, 742 (1997)].
13. V. A. Bushuev and V. V. Kozak, Poverkhnost', No. 2, 96 (1999).
14. A. V. Andreev, A. G. Michette, and A. Renwick, J. Mod. Opt. **35**, 1667 (1988).
15. A. Bruson, C. Dufour, B. George, *et al.*, Solid State Commun. **71**, 1045 (1989).
16. D. E. Savage, N. Schimke, Y.-H. Phang, *et al.*, J. Appl. Phys. **71**, 3283 (1992).
17. V. Holy and T. Baumbach, Phys. Rev. B **49**, 10668 (1994).
18. I. Pape, T. P. A. Hase, B. K. Tanner, *et al.*, Physica B (Amsterdam) **253**, 278 (1998).
19. H. Laidler, I. Pape, C. I. Gregory, *et al.*, J. Magn. Magn. Mater. **154**, 165 (1996).
20. V. E. Asadchikov, A. Yu. Karabekov, V. V. Klechkovskaya, *et al.*, Kristallografiya **43**, 119 (1998) [Crystallogr. Rep. **43**, 110 (1998)].
21. V. A. Chernov, N. I. Chkhalo, M. V. Fedorchenko, *et al.*, J. X-Ray Sci. Technol. **5**, 65 (1995).
22. A. I. Volokhov, É. P. Kruglyakov, and N. I. Chkhalo, Poverkhnost', No. 1, 130 (1999).
23. L. G. Parratt, Phys. Rev. **95**, 359 (1954).
24. V. A. Chernov, N. I. Chkhalo, M. V. Fedorchenko, *et al.*, J. X-Ray Sci. Technol. **5**, 389 (1995).
25. V. A. Chernov, N. I. Chkhalo, and S. G. Nikitenko, J. Phys. IV **7**, C2-699 (1997).
26. V. A. Chernov, E. D. Chkhalo, N. V. Kovalenko, *et al.*, Nucl. Instrum. Methods Phys. Res. A **448**, 276 (2000).
27. *Brief Description of the SR Experimental Station*, Preprint No. 90-92 (Novosibirsk Inst. of Nuclear Physics, Siberian Div., USSR Academy of Sciences, 1990).

Translated by A. Bagatur'yants

JETP Letters, Vol. 77, No. 2, 2003, pp. 84–87. Translated from Pis'ma v Zhurnal Éksperimental'noĭ i Teoreticheskoĭ Fiziki, Vol. 77, No. 2, 2003, pp. 89–92.

Atomic "Needles" and "Bullets" in Bose–Einstein Condensate and the Formation of Nanosized Structures

N. N. Rosanov*, Yu. V. Rozhdestvenskiĭ, V. A. Smirnov, and S. V. Fedorov

Scientific Research Institute of Laser Physics, St. Petersburg, 199034 Russia

** e-mail: rosanov@ilph.spb.su*

Received December 15, 2002

The Gross–Pitaevski equation modified through the inclusion of a term accounting for the nonlocality of interatomic interaction was used to demonstrate the occurrence of extremely narrow two- and three-dimensional solitonic states in atomic Bose–Einstein condensates. The estimates of the sizes of these states gave a value of ~20–60 nm (atomic "needles" and "bullets") for lithium atoms. The soliton lifetimes caused by two- and three-particle collisions were estimated. The limiting possibilities of the formation of nanostructures using needles and bullets were compared with the possibilities of other nanolithographic methods. © *2003 MAIK "Nauka/Interperiodica".*

PACS numbers: 03.75.Lm; 81.16.Nd

For atomic Bose–Einstein condensates (BECs) described by the Gross–Pitaevski equation [1], only one-dimensional solitonic states are possible, which were recently observed in the experiments with lithium atoms [2, 3]. It is generally believed (see, e.g., [4]) that two- and three-dimensional condensate solitons do not exist, because a condensate containing many atoms collapses. This situation is close to radiation self-focusing in media with cubic (Kerr) nonlinearity, which is described in optics by the nonlinear Schrödinger equation [5]. However, there are some factors in optics that restrict collapse, e.g., the nonparaxiality effects. Due to them, the final self-focusing stage of beams of supercritical power may consist in the formation of a spatial soliton with width less than the light wavelength ("optical needles") [6, 7]. It is natural to assume that taking into account any additional factors will make it possible to obtain two- and three-dimensional BEC solitons, including those with sizes substantially smaller than the de Broglie wavelength (atomic needles and bullets, respectively). It should be noted that solitons of atomic condensate with sizes as small as those are not only of general physical interest but are also of importance to applications in atomic nanolithography.

In the Gross–Pitaevski equation for the condensate wave function, the nonlinearity caused by interatomic interaction has a local character, although in the original Bogoliubov equation [8] the nonlinearity is described by the integral with respect to coordinates. The nonlocal nonlinearity can, basically, restrict collapse [9]. In [10], a modified Gross–Pitaevski equation with the corresponding correction term was derived in the approximation of weak nonlinearity, and it was shown that this equation provides rather wide stable two-dimensional solitons.

In this work, we examine the possibility of forming extremely narrow quasi-two-dimensional (atomic needles) and three-dimensional (atomic bullets) solitonic condensate states by the example of ^{7}Li in the (2, 2) state (the first number is the total atomic spin and the second is its projection) within the framework of the Gross–Pitaevski equation with the nonlocal nonlinearity [10] modified by the inclusion of a more complete form of the interatomic interaction potential. The choice of the lithium (2, 2) state is motivated by the fact that the parameters of atomic collisions for this state are well known. We will show that the cross-sectional dimension of atomic needles and the radius of atomic bullets are determined only by the characteristic spatial scale of interatomic potential and the total number of atoms in BEC. By changing the atomic scattering length (which is also determined by the parameters of interaction potential) in a magnetic field (Feishbach effect), one can control the sizes of these solitonic BEC states.

The modified Gross–Pitaevski equation for the one-particle condensate wave function has the form [10]

$$i\hbar\frac{\partial\Phi(\boldsymbol{\rho}, t)}{\partial t} = \left[-\frac{\hbar}{2M}\Delta_\rho + N_p(B_0|\Phi|^2 + B_2\Delta_\rho|\Phi|^2)\right]\Phi, \quad (1)$$

where M is the atomic mass and N_p is the number of atoms in the condensate. The coefficients $B_{0,2}$ are expressed through the interatomic potential $V(r)$, which is assumed to be spherically symmetric:

$$B_0 = \int V(r)d^3r = \frac{4\pi\hbar^2 a}{M}, \quad B_2 = \frac{1}{6}\int r^2 V(r)d^3r. \quad (2)$$

In Eq. (2), a is the S-wave scattering amplitude in the Born approximation. The second nonlinear term in Eq. (1) accounts for the interaction nonlocality. The wave function is normalized as

$$\int |\Phi|^2 d^3\rho = 1. \quad (3)$$

For two-dimensional structures, the number of atoms N_p in Eq. (1) should be replaced by the linear number of atoms N_p/L, where L is the soliton length. This allows the unit normalization of the two-dimensional distribution in the cross-sectional plane to be retained.

It is convenient to introduce the dimensionless variables $\rho' = \rho/\rho_c$ and $t' = t/t_c$, where $t_c = \sqrt{2M\rho_c/\hbar}$, and to seek stationary solutions to Eq. (1) in the form

$$\Phi_d(\rho, t) = \frac{1}{\sqrt{U_d}\rho_c} A_d(\rho') \exp(ikt'), \quad (4)$$

where the index $d = 2$ or 3 defines the dimensionality of the problem (one-dimensional geometry $d = 1$ can be considered in a similar way), $U_2 = 8\pi|a|N_p/L$, and $U_3 = 8\pi|a|N_p$. Equation (1) reduces to

$$[\Delta_{\rho'} - k + A_d^2 + s\Delta_{\rho'}A_d^2]A_d = 0, \quad (5)$$

where $s = B_2/B_0\rho_c^2$. The nonlinearity sign is chosen so that the scattering length a is negative; then Eq. (5) has solitonic solutions (specifically, bright solitons). Note that, for $s = 0$ (local nonlinearity), the scaling factor ρ_c is arbitrary, reflecting the scale invariance of the solution. For $s > 0$, the problem reduces to the case $s = 1$ by introducing the scaling factor

$$\rho_c = \sqrt{B_2/B_0}. \quad (6)$$

The solitonic (localized) solutions to Eq. (5) for the two-dimensional ($d = 2$) and three-dimensional ($d = 3$) cases were found numerically. The dependence of the quantity N_d (which is proportional to the number of atoms N_p) on the soliton parameter k

$$N_2(k) = \int_0^\infty |A_2(\rho')|^2 d^2\rho' = \frac{8\pi|a|N_p}{L},$$
$$N_3 = \int_0^\infty |A_3(\rho')|^2 d^3\rho' = \frac{8\pi|a|N_p}{\rho_c} \quad (7)$$

is demonstrated in Fig. 1. One can see that the Vakhitov–Kolokolov criterion $\partial N/\partial k > 0$ for soliton stability is met in the two- and three-dimensional cases. Recall that, for the local nonlinearity $s = 0$, this criterion is satisfied neither for the two-dimensional nor for the three-dimensional solitons ($N_2 = N_2^c = 8\pi|a|N_p^c/L = 11.7$, $dN_2/dk = 0$, $dN_3/dk < 0$). The obtained dependences confirm that the two-dimensional soliton is stable (this was proved analytically for small k in [10]) and show

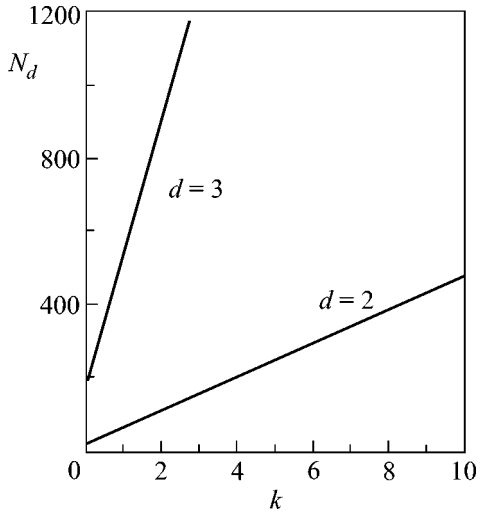

Fig. 1. Dependence of N_d (proportional to the number of atoms) on the soliton parameter k for the two-dimensional ($d = 2$) and three-dimensional ($d = 3$) solitons.

that the nonlocality stabilizes three-dimensional spherically symmetric solitons as well. The N_d dependence of the dimensionless effective halfwidth

$$w_d^2 = \int_0^\infty \rho'^2 |A(\rho')|^2 d^d\rho'/N_d \quad (8)$$

of the two- and three-dimensional solitons is shown in Fig. 2. The vertical dashed line corresponds to the local nonlinearity in the two-dimensional geometry. The horizontal dotted line shows the asymptotic value at N_d, $k \longrightarrow \infty$ for the nonlocal nonlinearity. It can be shown that the soliton profile is described by the zero-order Bessel function J_0 ($s = 1$):

$$A(\rho') = \begin{cases} k^{1/2}\sqrt{1 - J_0(\rho')/J_0(\rho_1')}, & \rho' < \rho_1', \\ 0, & \rho' > \rho_1'. \end{cases} \quad (9)$$

The quantity $\rho_1' = 3.837$ is determined from the condition $J_1(\rho_1') = 0$. The asymptotic dimensionless halfwidth is $w_2(\infty) = 1.83$.

To pass to dimensional quantities, one should use the coefficients $B_{0,2}$ defined in Eqs. (2). However, for the standard interatomic potentials of the Lennard-Jones type, both integrals in Eqs. (2) formally diverge at small r, so that one should take into account that the distance of closest approach in particle collisions cannot be smaller than a certain radius which is determined by the repulsive part of potential and the collision energy. The simplest way to overcome this difficulty amounts to the introduction of a finite truncation radius r_{tr}, whose value can be determined by the first of Eqs. (2) using the known scattering length a.

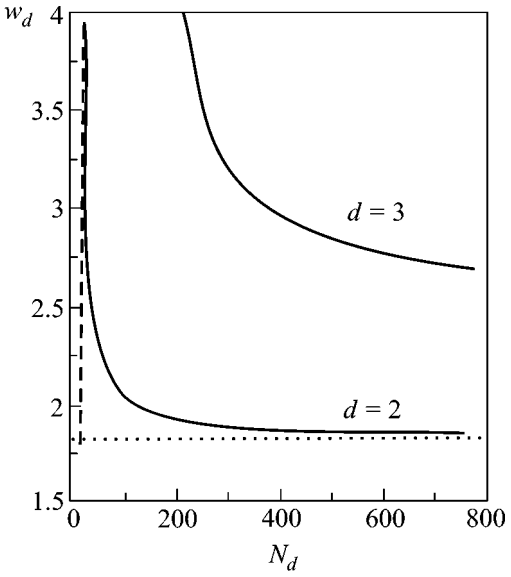

Fig. 2. Dependence of the dimensionless effective soliton halfwidth w_d on N_d for the two-dimensional ($d = 2$) and three-dimensional ($d = 3$) solitons. The vertical dashed line corresponds to the approximation of local nonlinearity for $d = 2$. The horizontal dotted straight line shows the asymptotic value of halfwidth $w_2(\infty) = 1.83$ ($d = 2$).

Let us consider the triplet collision of lithium atoms. The Lennard-Jones potential has the form

$$V(r) = D\left(\frac{1}{r^{12}} - \frac{1}{r_0^6 r^6}\right), \qquad (10)$$

where the distance at which the potential turns into zero is $r_0 = 6.4$ au, and $D/r_0^6 = 1.39 \times 10^3$ au [12]. The first of Eqs. (2) gives the following relation:

$$\int_{r_{tr}}^{\infty} V(r) r^2 dr = \frac{D}{9}\left(\frac{1}{r_{tr}^9} - \frac{3}{r_{tr}^3}\right) = \frac{\hbar^2}{M} a. \qquad (11)$$

By introducing the variable $x = (r_0/r_{tr})^3$, we arrive at the cubic equation

$$x^3 - 3x = \frac{9 r_0^9 \hbar^2 a}{MD} = -3.6 \times 10^{-3}. \qquad (12)$$

The constant on the right-hand side of this equation was calculated using the scattering length $a = -27$ au. From Eq. (12) it is seen that the truncation radius

$$r_{tr} \approx \frac{r_0}{3^{1/6}} = 0.83 r_0 = 5.32 \text{ au} \qquad (13)$$

only weakly depends on the scattering length. At the same time, the scattering length changes drastically upon a slight change in the interatomic potential. The root of Eq. (12) corresponding to large r_{tr} has no physical meaning, because the distance of closest approach in the S scattering is $\sim r_0$. The excess of kinetic energy, which permits the colliding particles to attain distances $t_{tr} < r_0$, arises due to the fact that the distance of closest approach is finite [4].

We are now in position to calculate the scaling factor ρ_c defined by Eq. (6):

$$I_2 = \int_{r_{tr}}^{\infty} r^4 V dr = D\left(\frac{1}{7 r_{tr}^7} - \frac{1}{r_0^6 r_{tr}}\right) = -143 \text{ au} \qquad (14)$$

and

$$\rho_c^2 = \frac{I_2 M}{6\hbar^2 |a|} = 1.1 \times 10^4 \text{ a.e.} \qquad (15)$$

Therefore, $\rho_c = 100$ au = 53 A. Note that the integral I_2 depends weakly on the scattering length, so that the scaling factor is $\rho_c \sim 1/|a|^{1/2}$.

With these parameters, the minimal halfwidth of a two-dimensional soliton in the condensate of ^{7}Li (2, 2) atoms (Fig. 2) is $w_\rho \approx 1.83\rho_c \approx 100$ A = 10 nm. One can control the value of N_2 by varying the scattering (see Eq. (7)) by a static magnetic field. It is seen from Fig. 2 that a rather small width is achieved at $N_2 \geq 100$. For the practically minimal narrowing, a cigar-shaped condensate of length 100 μm should contain 3×10^5 atoms, so that the atomic concentration $n \approx 1.3 \times 10^{19}$ cm^{-3}. For concentrations as high as this, the number of condensed particles rapidly decreases because of the spin flip in pair collisions. The characteristic time of condensate decay is

$$\tau_r = \left|\frac{1}{n}\frac{dn}{dt}\right|^{-1} = (2n\langle\sigma V\rangle)^{-1} = 8 \text{ μs}. \qquad (16)$$

Here, $\langle\sigma V\rangle = 5 \times 10^{-15}$ cm^3/s is the decay rate calculated in [13]. Such a short lifetime of the solitonic state may present problems in its experimental implementation. The situation is cardinally changed in the condensate of ^{7}Li (1, 1) atoms. The scattering length in this case is $|a| = 1.6 \times 10^{-8}$ cm [2]. Although the corresponding minimal beam halfwidth is ~30 nm, the characteristic time of atomic loss is now determined by the three-particle collisions, because the pair collisions are associated with the transitions to the excited hfs states and so they are energetically impossible. According to [14], this time is equal to

$$\tau_r' = (1.44 V r_c^5 n^2)^{-1}, \qquad (17)$$

where V is the mean atomic velocity and r_c is the effective radius of three-particle collision. By setting $r_c \approx |a|$, we obtain $\tau_r \sim 40$ s.

The almost limiting narrowing of the three-dimensional solitonic ^{7}Li (2, 2) condensates can be achieved with appreciably lower atomic concentrations. Indeed, one can see from Fig. 2 that the soliton halfwidth for $N_3 = 250$ is $w_3\rho_c = 18$ nm (minimal halfwidth equals 13 nm). The corresponding soliton contains ~40 atoms,

and the atomic concentration is $n = 1.4 \times 10^{18}$ cm^{-3}, which is an order of magnitude lower than the concentration in the two-dimensional soliton. Accordingly, the condensate decay time caused by the pair collisions is $\tau_r = 80$ μs.

Thus, the cross-sectional size of the two- and three-dimensional solitons in the Bose–Einstein condensates of alkali-earth atoms can be as small as ~20–60 nm, rendering the atomic needles and bullets promising for use in atomic nanolithography. Indeed, the minimal size of the structures obtained by optical photolithography is ~120–150 nm, and only the vacuum ultraviolet technique could possibly reduce it to 80 nm. At the same time, the use of other methods, such as focusing of the preliminarily cooled atoms in the nodes of a standing light wave [15] or scattering of the atomic wave packets by a periodic potential [16], provides a strictly periodic character of the formed structure. Hence, these methods of forming periodic profile are, generally speaking, of interest not in nanolithography as such but in the formation of superlattices with strictly periodic doping. In contrast, the suggested variant of nanolithography with the use of atomic needles and bullets allows one to obtain any arbitrary pattern at the sample surface, while the simplest estimates of the exposure time show that a repetition rate of ~10^2 soliton/s is enough for the practical use of this method. The possibility of forming a sequence of solitons of the Li condensate was demonstrated experimentally in [2].

We are grateful to W. Firth and A. Aspect for helpful and stimulating discussions. This work was supported by the INTAS Foundation (grant no. 2001-0855), the Russian Foundation for Basic Research (project nos. 01-02-17242, 02-02-17686), and UR.01.01.040.

REFERENCES

1. L. P. Pitaevskiĭ, Usp. Fiz. Nauk **168**, 641 (1998) [Phys. Usp. **41**, 569 (1998)].
2. K. E. Strecker, G. B. Partridge, A. G. Truscott, and R. G. Hulet, Nature **417**, 150 (2002).
3. T. Bourdel, L. Khaykovich, F. Schreck, *et al.*, *Technical Digest of IQEC'2002* (Moscow, 2002), p. 54.
4. K. Burnett, M. Edwards, and C. W. Clark, Phys. Today **52**, 37 (1999).
5. S. N. Vlasov and V. I. Talanov, *Self-Focusing of Waves* (Inst. Prikl. Fiz. Ross. Akad. Nauk, Nizhni Novgorod, 1997).
6. V. E. Semenov, N. N. Rozanov, and N. V. Vysotina, Zh. Éksp. Teor. Fiz. **116**, 458 (1999) [JETP **89**, 243 (1999)].
7. N. N. Rozanov, N. V. Vysotina, and A. G. Vladimirov, Zh. Éksp. Teor. Fiz. **118**, 1307 (2000) [JETP **91**, 1130 (2000)].
8. N. N. Bogolyubov, Izv. Akad. Nauk SSSR, Ser. Fiz. **11**, 77 (1947).
9. S. K. Turitsyn, Teor. Mat. Fiz. **64**, 226 (1985).
10. N. N. Rosanov, A. G. Vladimirov, D. V. Skryabin, and W. J. Firth, Phys. Lett. A **293**, 45 (2002).
11. N. G. Vakhitov and A. A. Kolokolov, Izv. Vyssh. Uchebn. Zaved., Radiofiz. **16**, 1020 (1973).
12. R. Cote, A. Dalgarno, and M. J. Jamieson, Phys. Rev. A **50**, 399 (1994).
13. A. J. Moerdijk and B. J. Verhaar, Phys. Rev. A **53**, R19 (1996).
14. F. T. Smith, J. Chem. Phys. **36**, 248 (1962).
15. W. R. Anderson, C. C. Bradley, J. J. McClelland, and R. J. Celotta, Phys. Rev. A **59**, 2476 (1999).
16. *Atom Interferometry*, Ed. by P. R. Berman (Academic, New York, 1997).

Translated by V. Sakun

JETP Letters, Vol. 77, No. 2, 2003, pp. 88–93. Translated from Pis'ma v Zhurnal Éksperimental'noĭ i Teoreticheskoĭ Fiziki, Vol. 77, No. 2, 2003, pp. 93–98.

Thermo- and Galvanomagnetic Properties of Lead Chalcogenides at High Pressures up to 20 GPa

V. V. Shchennikov and S. V. Ovsyannikov*

Institute of Metal Physics, Ural Division, Russian Academy of Sciences, ul. S. Kovalevskoĭ 18, Yekaterinburg, 620219 Russia

** e-mail: sergey_v_o@imp.uran.ru*

Received December 3, 2002; in final form, December 15, 2002

The Nernst–Ettingshausen (NE) effect in the initial NaCl and high-pressure GeS phases was studied at a high pressure P for n-PdTe, p-PbSe, and p-PbS to estimate the mobility μ and the charge-carrier scattering parameter r. It was found that the transverse and longitudinal NE effects in PbTe and PbSe increase with pressure, indicating the transition to the gapless state near $P \approx 3$ GPa. The sign of the transverse NE effect changes because of the change in the electron scattering mechanism in the GeS phase. The experimentally observed weakening of the NE and magnetoresistance effects at high P gives evidence for the indirect energy gap E_g in the high-pressure phases with GeS structure. © *2003 MAIK "Nauka/Interperiodica".*

PACS numbers: 72.20.My; 72.20.Pa

Experimental investigations of the electrophysical properties of materials subjected to ultrahigh pressures are an efficient method of studying the electronic structure and charge-carrier parameters; the observation of metallic and superconducting oxygen states at $P \approx$ 96 GPA is among the most expressive recent examples [1]. Up to now, only the electrical resistivity ρ [1], the thermoelectric power S [2, 3], and the transverse magnetoresistance (MR) [4] have been measured at ultrahigh pressures. The efficiency of the MR method was most conspicious in the studies of semimetal–semiconductor phase transitions at ultrahigh P values for HgX samples (X = Te, Se, S, O), in which the MR sign was found to be inverted reversibly. The estimated values of electron mobility μ were found to correspond to bulk crystals at $P = 0$ [4]. This method of measuring MR was also proposed in [5] for estimating electron mobility and concentration in semiconductor microstructures—infrared detectors of sizes ~$100 \times 50 \times 8$ μm.

The main difficulty in electric measurements under ultrahigh P in diamond anvil chambers [1–4] is caused by small sample sizes, which are comparable with the sizes of semiconductor microstructures [5]. For this reason, attempts are being undertaken to solve the problem of taking electrical probes to the samples by using modern semiconductor technologies, to form at the surface of a diamond anvil (by ion-implantation techniques, etc.) thin (~1 μm) conducting layers insulated by a diamond film [6]. Such diamond anvils are now used in studying the $S(P)$ dependence, true enough, below 10 GPA [7], where more correct results are obtained in large-volume chambers with a compressible capsule [8].

Measurements of the thermomagnetic (TM) effects that carry direct information on μ and r [9] were performed in the range from 0 to 3 GPa, where only a little work has been done [10]. Due to the use of synthetic diamond anvils, the P range was extended to 30 GPa in the study of elementary Group VI semiconductors Te and Se [11, 12]. However, it was still unclear whether one can apply the TM method [11, 12] in studying more complex semiconductors, where not one but several bands make a contribution to the conductivity and where the phase transitions are induced by pressure [13].

In this work, the TM effects were studied under ultrahigh pressure P in direct-gap IV–VI semiconductors PbX (X = Te, Se, and S) with, respectively, $E_g \approx$ 0.29, 0.27, and 0.41 eV at the L point of the Brillouin zone [14]. This class of materials was chosen as a suitable object for developing the TM measurement technique at ultrahigh P, because it was well studied under ambient conditions [14] and because E_g in PbX tends to zero twice: in the initial NaCl phase [14–16] and in the high-pressure GeS-type phase [14, 19–22], which is formed, respectively, above ~2.5, ~4.0, and ~4.5–6 GPa [17, 18] near the transition to the metallic CsCl phase at $P \approx$ 12–21 GPa [17, 18, 20]. The study of PbX crystals is also of independent interest, because they are widely used in electronics in the fabrication of photoresisters, as model materials for studying quantum dots [23], and because they are most efficient in the fabrication of thermogenerators in the moderate temperature range 600–1000 K [14]. Up to now, TM studies in PbX have been performed only at atmospheric pressure P for bulk samples [9] and films [24, 25]. As to the microscopic

samples, the TM effects have been investigated neither for PbX nor for other materials. Our studies were carried out with *n*-PbTe, *p*-PbSe, and *p*-PbS single crystals. The electron (hole) concentration was equal to 1.5×10^{18}, 1.1×10^{18}, and 1×10^{18} cm^{-3}, respectively.

The purpose of this work was to determine the mobility and scattering mechanisms for charge carriers in PbX using TM measurements at an ultrahigh pressure *P* up to 20 GPa.

The high-pressure TM measurements were made by a method corresponding to the one described in [11, 12]. High quasi-hydrostatic pressure *P* was generated using synthetic diamond chambers [3, 11]. The diamond anvils were used as heat sinks [3, 11]. To produce a temperature gradient, one of the anvils was heated by a heater, and the temperature was measured at fixed anvil points [3, 11, 26]. The value of *S* was derived from the linear dependence of the thermoelectric power on the temperature difference in the sample (insert in Fig. 1). The samples were disc-shaped with thicknesses ranging from ~0.05 to 0.02 mm and a diameter of 0.3 mm. The MR and *S* signals were detected using pressed platinum–silver 5 μm-thick contacts or well-conducting diamond anvils [3, 11, 18] with allowance for the error introduced in the thermoelectric power [3, 18, 26]. The pressure in a solid pressure-transmitting medium (Catlinite) was estimated with an accuracy of ±10% from the force calibration curve that was constructed using the observed phase transformations in the Bi, ZnS, GaP, etc., reference materials for each chamber [13, 26].

Measurements of *S* and MR were performed at fixed *P* in a magnetic field *B* lower than 2 T produced in an armored electromagnet. The MR and *S*(*B*) effects were not observed for closed anvils (without sample). Because of the asymmetric arrangement of the contacts, the even and odd field effects, e.g., the contribution to MR from the Hall effect, are ordinarily present in semiconducting samples [27]. This fact was used in our experiments for measuring the longitudinal and transverse Nernst–Ettingshausen (NE) effects by rotating the chamber about its axis in the magnetic field [11, 12]. The setup allowed one to detect and store the magnetic field strength, the temperature difference, the current, and the electrical signals from the sample, followed by transmission of the data to a computer [11, 18].

The electrical resistivity and the thermoelectric power of the *p*-PbS, *p*-PbSe, and *n*-PbTe crystals decreased with the pressure buildup because of a decrease in E_g (with a coefficient of ~0.08 eV/GPa for all PbXs) [14–16], whereupon they increased jumpwise in the GeS phase (above ~2.5–5 GPa; Fig. 1), where, according to the estimates made in [18], semiconductor gaps of ~0.6, ~0.4, and ~0.1 eV opened. "Smearing" of the structural transitions in PbX (Fig. 1) was also observed in Raman scattering upon hydrostatic compression; in PbTe, the spectra typical of the GeS phase appeared at $P \sim 3$ GPa (below the structural transition [20]) and persisted up to ~20 GPa (above the transition point $P_t \approx 15$ GPa in the CsCl lattice [20–22]). In the GeS phase, *S* again decreased because of a decrease in E_g [18] (Fig. 1).

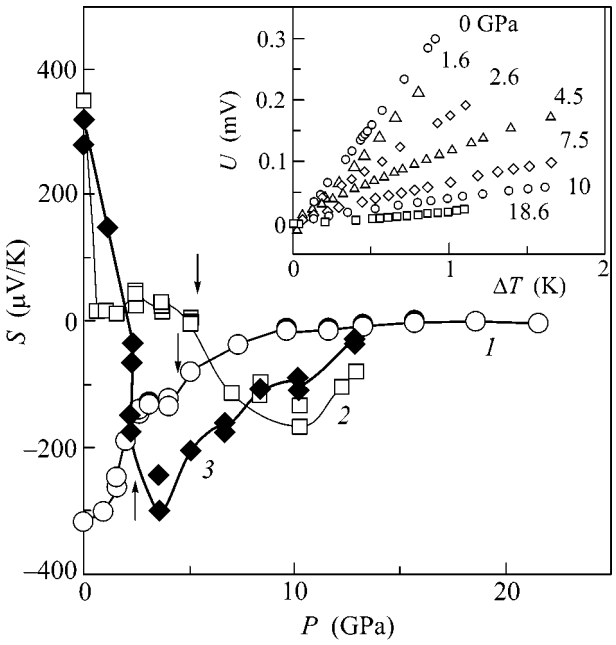

Fig. 1. Pressure dependence of the thermoelectric power for the (*1*) *n*-PbTe, (*2*) *p*-PbSe, and (*3*) *p*-PbS samples at T = 295 K. Arrows indicate the onset of phase transitions to the GeS phase. Insert: the dependence of thermoelectric voltage U on the temperature difference ΔT for the *n*-PbTe sample at T = 295 K and fixed pressures P (in GPa; shown in the graph).

The typical behavior of *S* caused by the variation of magnetic induction *B* upon the rotation of the chamber with a sample in a magnetic field is shown in Fig. 2. The function *S*(*B*) was the sum of terms linear and quadratic in *B*, which were related to the transverse and longitudinal NE TM effects, respectively [9, 11, 27]. The contribution from the longitudinal NE effect to the transverse effect was observed for almost all chamber positions (Figs. 2–4). The coefficient *Q* of the transverse NE effect was derived from the linear portion of the *S*(*B*) curve. The longitudinal (quadratic in *B*) NE effect was observed when the chamber with the sample was turned through an angle of 90°; the residual contribution linear in *B* was subtracted (Figs. 2–4).

The sign of *S* changed with pressure, indicating a change in the predominant type of charge carriers (Fig. 1). The expressions for MR and the coefficient *Q* of the transverse NE effect, which describe the transition from hole to electronic conduction (in weak mag-

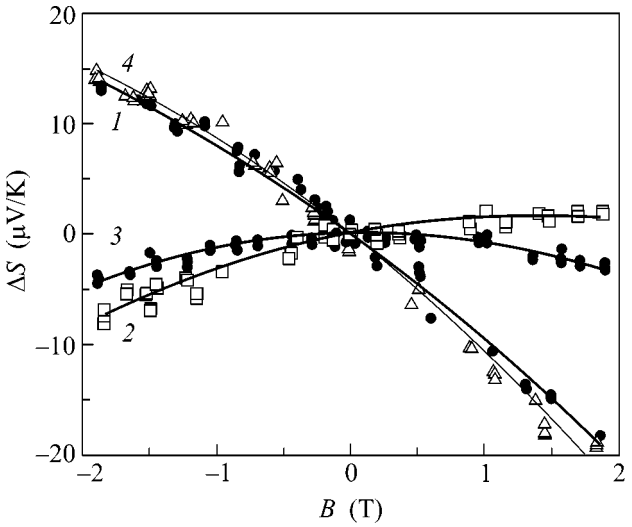

Fig. 2. Thermopower variations for the *n*-PbTe sample at $T = 295$ K and pressure $P = 2.4$ GPa upon sequential rotations of a chamber with the sample in a magnetic field: (*1*) transverse NE effect, (*2*) mixed effect, (*3*) longitudinal NE effect, and (*4*) reversion to the initial state (transverse NE effect).

netic fields $\mu B < 1$) [9, 27], have the form

$$\frac{\Delta\rho}{\rho} = B^2 b_r\left[\left(\frac{\sigma_n}{\sigma}\mu_n^2 + \frac{\sigma_p}{\sigma}\mu_p^2\right) - \left(\frac{\sigma_n}{\sigma}\mu_n - \frac{\sigma_p}{\sigma}\mu_p\right)^2\frac{a_r^2}{b_r}\right], \quad (1)$$

$$Q = \frac{k_o}{e}a_r\left[r\left(\frac{\sigma_n}{\sigma}\mu_n - \frac{\sigma_p}{\sigma}\mu_p\right) + \frac{\sigma_n\sigma_p}{\sigma^2}(\mu_n + \mu_p)\left(2r + 5 + \frac{E_g}{kT}\right)\right], \quad (2)$$

where ρ is the resistivity; k is the Boltzmann constant; and a_r and b_r are constants depending on the scattering parameter r, which determines the dependence of relaxation time τ on electron energy ε: $\tau(\varepsilon) \sim \varepsilon^r$. For zero electronic conductivity σ_n or hole conductivity σ_p, Eqs. (1) and (2) transform to the single-band expressions, which were used for an analysis of the experimental data; in this case, the signs of the coefficients $\Delta\rho/\rho$ and Q do not change [9, 27]. On the contrary, the longitudinal NE effect (a change in S in the transverse magnetic field) depends on the charge-carrier sign [27]:

$$\Delta S_{\parallel} = \frac{k_0}{e}(\mu B)^2 A_2. \quad (3)$$

In the presence of two charge-carrier groups, the coefficient A_2 in Eq. (3) is replaced by a function depending on r, E_g, μ_n/μ_p, and σ_n/σ_p [27]. If charge carriers are scattered by lattice acoustic vibrations ($r = -1/2$) and charged centers ($r = 3/2$), the constant A_2 takes the

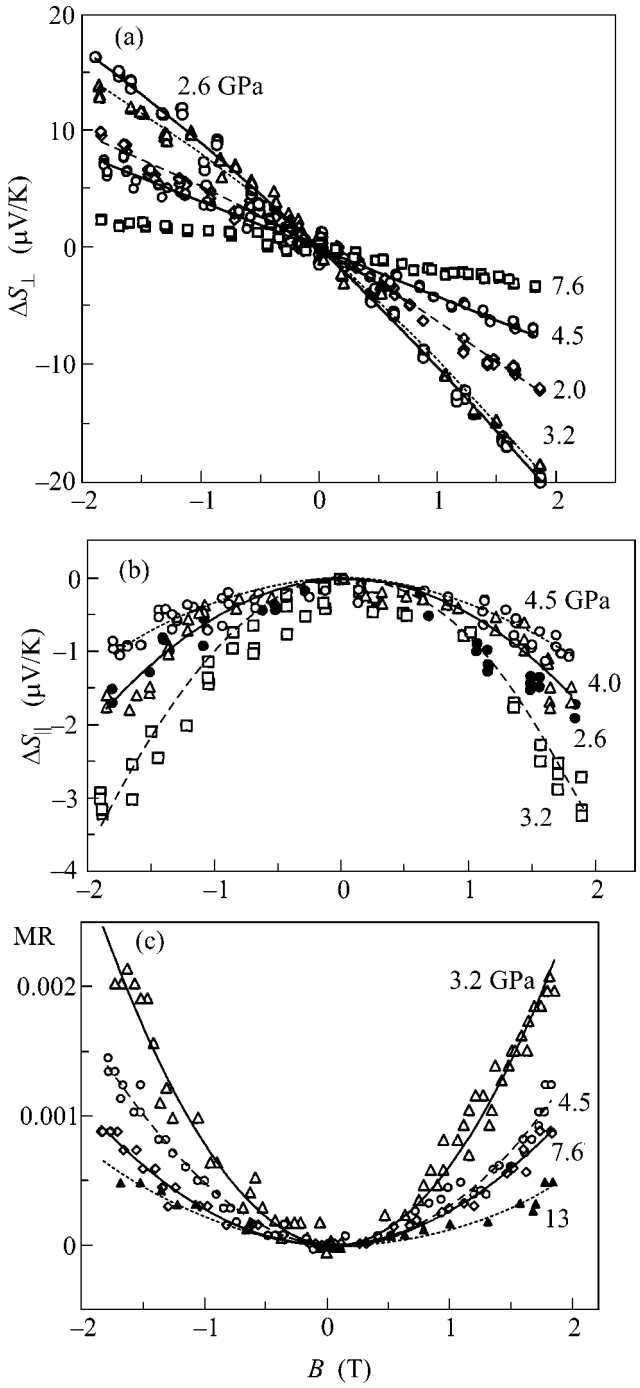

Fig. 3. Thermopower variations: (a) transverse NE effect, (b) longitudinal NE effect, and (c) magnetoresistance effect in a magnetic field for the *n*-PbTe sample at $T = 295$ K and fixed pressures P (in GPa; shown in the graphs).

approximate values +1 and –30, respectively, and the value of S must increase or decrease in a magnetic field [27].

The following voltages are measured in the experiment: $\Delta U_{\parallel}(B) = \Delta S_{\parallel}(B)\Delta T$ and $\Delta U_{\perp}(B) = BQ\Delta T(\Delta y/\Delta x)$, where Δy and Δx are, respectively, the distances

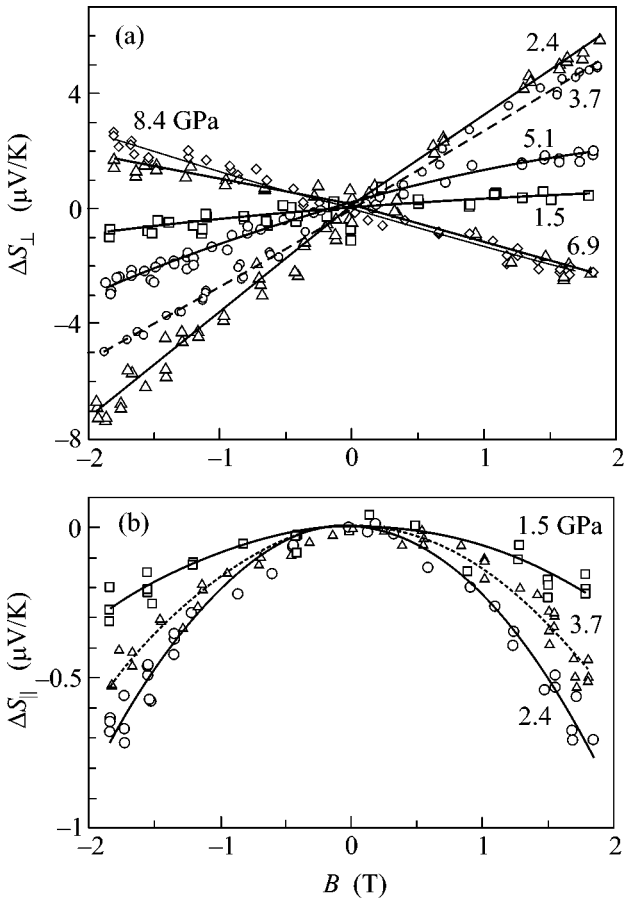

Fig. 4. Thermopower variations in a magnetic field: (a) transverse NE effect and (b) longitudinal NE effect for the *p*-PbSe at $T = 295$ K and fixed pressures P (in GPa; shown in the graphs).

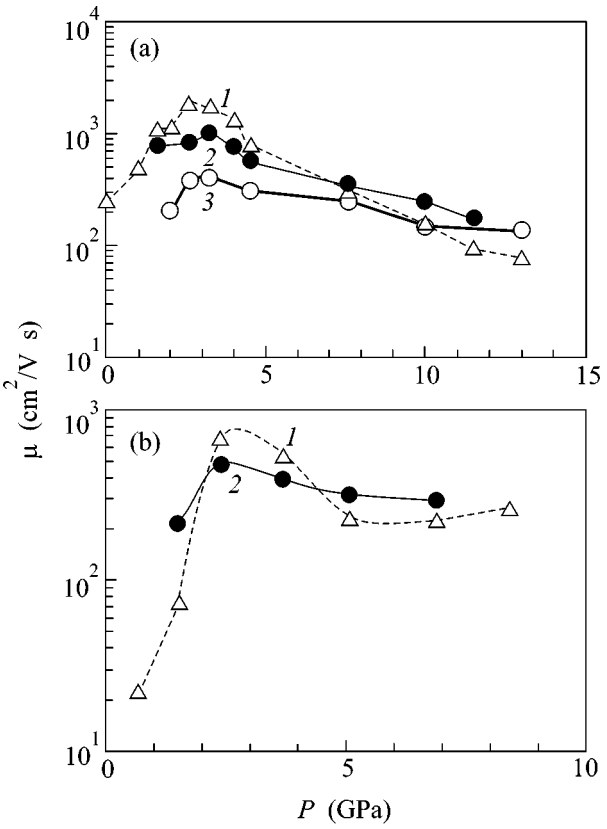

Fig. 5. Pressure dependences of mobilities for the (a) *n*-PbTe and (b) *p*-PbSe samples, as estimated from (*1*) transverse NE effect, (*2*) longitudinal NE effect, and (*3*) MR at $T = 295$ K.

between the cold and hot sample edges and between the potential contacts in the Hall direction [11]. For this reason, the measured signal for the transverse NE effect is proportional not only to the coefficient Q but also to $\Delta y/\Delta x \sim 1$.

In the *n*-PbTe sample, the magnitude of S increases in a magnetic field (Figs. 2, 3), which corresponds to the scattering parameter $r = -1/2$; the same values were obtained for r from the TM measurements at $P = 0$ [9, 14]. For PbSe, the field-induced change in S has the same sign (Fig. 4), but S has a small positive value (Fig. 1). The fact that $S(P)$ in the PbSe sample decreases drastically in its initial NaCl phase (Fig. 1) indicates that the electronic contribution to the conductivity increases. It is thus natural to assume that the longitudinal NE effect in PbSe is caused by electrons, whose mobility is higher than for holes [14], so that the scattering parameter for it should also be $r = -1/2$. The greatest contribution to the effects quadratic in B comes from the most mobile charge carriers [27], in our case electrons. Above 5 GPa, the transverse (Fig. 4b) and longitudinal (not shown in figure) NE effects in the GeS phase of PbSe change their signs. This indicates that r changes sign and that the electron scattering by charged centers ($r = 3/2$) or optical lattice vibrations ($r = 1$) [27] likely becomes dominant. The parameter r can increase in the presence of lattice structural defects, as was observed in thin films of triple lead chalcogenides [24, 25].

With an increase in P, both TM and MR effects in the PbTe and PbSe samples increased and achieved their greatest magnitudes at the same pressures (Figs. 3, 4). The NE effects in PbSe were observed below ~8 GPa, after which the signal became comparable to the experimental error, whereas in PbTe the signal was observed up to the transition to the metallic phase. As P was reduced to 2–3 GPa, the TM effects in PbSe and PbTe again increased, while the transverse NE effect in PbSe again changed its sign (not shown in Fig. 4). No tangible changes in the thermoelectric power and electrical resistivity were observed for PbS in a magnetic field. The magnitudes of the TM and MR effects in the PbX samples correlate with their mobilities: $\mu(\text{PbS}) < \mu(\text{PbSe}) < \mu(\text{PbTe})$ [14].

The behavior of the MR and NE effects is representative of the pressure-induced changes in m and μ (Fig. 5). The maxima observed at $P \sim 3$ GPa for these effects and for the calculated $\mu(P)$ values can naturally

be associated with the PbX transition to the gapless state (GS), where the mobilities $\mu \sim e\tau/m \sim 1/E_g$ should be the highest [14, 27]. Analogous maxima were observed for MR and μ in the region of GS transition at helium temperatures and at $P < 1.8$ GPa for PbSe and for the PbSnX compounds [14, 28, 29]. Judging from the literature data, the PbX transition to the gapless state has not been observed at room temperature so far. The low-P mobilities estimated for PbSe and PbTe are somewhat lower than in single-crystal films at $P = 0$ [9, 14, 28, 30] but are higher in the GS (Fig. 5a). In the case of two-band conduction, the values of μ (Fig. 5) correspond to the effective "mobility" that includes the contributions from different bands (in semimetals, e.g., $\mu = (\mu_n\mu_p)^{1/2}$ [27]). Since the NE and MR effects decrease with increasing P in the high-pressure phase (Figs. 2–4), one can conclude that the relation $m \sim E_g$ does not hold and, hence, E_g is indirect, contrary to the NaCl phase.

According to the theoretical model [31, 32], the NaCl structure of the PbX crystals with metallic conduction is unstable against the Peierls distortion, which doubles the lattice spacing if the energy gain due to the opening of a semiconducting gap at the Fermi level exceeds the lattice deformation energy. It follows from the results of this work that the gapless state in PbTe and PbSe (electronic structure of metallic type) arises at ~3 GPa; i.e., it precedes the structural transition with the doubling of lattice parameter [14, 21, 22]. Judging from the values of E_g and dE_g/dP in PbS [14–16], the structural transition at 2.5 GPa should proceed after the GS transition. However, one can see from the experimental $S(P)$ and $\rho(P)$ dependences [18] that all three PbX compounds reach the near-metallic state before the onset of structural transition.

Thus, measurements of TM effects have made it possible to observe the PbX transition to the gapless state at room temperature and to estimate the charge-carrier mobility and scattering parameter over a wide range of P values. Analysis of the behavior of E_g in the high-pressure NaCl and GeS phases of PbX indicates that the gap in the second phase is indirect. This gives evidence for the obvious merits of the TM method in studying microsamples at ultrahigh pressures.

The temperature lowering should result in a sizable increase of the TM effects because of a strong increase in the electron and hole mobilities in PbX [14]. Compared to the conventional method of thermoelectric cooling based on the Peltier effect, the TM effects seem to be much more promising [33], while the diamond anvils used in the experiment serve as a real thermoelectric device, because their heat conductivity is several times higher than in copper. For this reason, the method of studying the TM effects under pressure in a diamond chamber may find useful practical applications [13].

This work was supported by the Russian Foundation for Basic Research, project no. 01-02-17203.

REFERENCES

1. K. Shimizu, K. Suhara, M. Ikumo, *et al.*, Lett. Nature **393**, 767 (1998).
2. N. Sakai, K. Takemura, and K. Tsuji, J. Phys. Soc. Jpn. **51**, 1811 (1982).
3. I. M. Tsidil'kovskiĭ, V. V. Shchennikov, and N. G. Gluzman, Fiz. Tekh. Poluprovodn. (Leningrad) **17**, 958 (1983) [Sov. Phys. Semicond. **17**, 604 (1983)].
4. V. V. Shchennikov, Fiz. Tverd. Tela (St. Petersburg) **35**, 783 (1993) [Phys. Solid State **35**, 401 (1993)].
5. J. R. Lowney, W. R. Thurber, and D. G. Seiler, Appl. Phys. Lett. **64**, 3015 (1994).
6. S. T. Weir, J. Akella, C. A. Ruddle, *et al.*, Appl. Phys. Lett. **77**, 3400 (2000).
7. J. F. Meng, N. V. Chandra Shekar, D.-Y. Chung, *et al.*, in *Advances on High Pressure Science and Technology*, Ed. by A. K. Bandyopadhyay, D. Varandani, and K. Lal (Alpha, New Delhi, 2001), p. 321.
8. L. G. Khvostantsev, L. F. Vereshchagin, and N. M. Uliyanitskaya, High Temp.–High Press. **5**, 261 (1973).
9. I. M. Tsidil'kovskiĭ, *Thermomagnetic Effects in Semiconductors* (Fizmatgiz, Moscow, 1960; Academic, New York, 1962).
10. M. M. Akselrod, K. M. Demchuk, and I. M. Tsidilkovskii, Phys. Status Solidi **27**, 249 (1968).
11. V. V. Shchennikov and S. V. Ovsyannikov, Pis'ma Zh. Éksp. Teor. Fiz. **74**, 546 (2001) [JETP Lett. **74**, 486 (2001)].
12. V. V. Shchennikov and S. V. Ovsyannikov, Solid State Commun. **121**, 323 (2002).
13. S. V. Ovsyannikov and V. V. Shchennikov, Physica E (Amsterdam) (2002) (in press).
14. Yu. I. Ravich, B. A. Efimov, and I. A. Smirnov, *Semiconducting Lead Chalcogenides* (Nauka, Moscow, 1968; Plenum, New York, 1970).
15. A. A. Averkin, S. Kasimov, and E. D. Nensberg, Fiz. Tverd. Tela (Leningrad) **4**, 3669 (1962) [Sov. Phys. Solid State **4**, 2683 (1962)].
16. A. A. Averkin, B. Ya. Moĭzhes, and I. A. Smirnov, Fiz. Tverd. Tela (Leningrad) **3**, 1859 (1961) [Sov. Phys. Solid State **3**, 1354 (1961)].
17. N. B. Brandt, D. V. Gitsu, N. S. Popovich, *et al.*, Pis'ma Zh. Éksp. Teor. Fiz. **22**, 225 (1975) [JETP Lett. **22**, 104 (1975)].
18. V. V. Shchennikov, S. V. Ovsyannikov, and A. Yu. Derevskov, Fiz. Tverd. Tela (St. Petersburg) **44**, 1762 (2002) [Phys. Solid State **44**, 1845 (2002)].
19. G. A. Samara and H. G. Drickamer, J. Chem. Phys. **37**, 1159 (1962).
20. T. Chattopadhyay, H. G. Von Schnering, W. A. Grosshans, and W. A. Holzapfel, Physica B & C (Amsterdam) **139–140**, 356 (1986).
21. S. Ves, Yu. A. Pusep, K. Syassen, and M. Cardona, Solid State Commun. **70**, 257 (1989).
22. M. Baleva and M. Momtchilova, Phys. Rev. B **50**, 15056 (1994).
23. G. D. Smith, S. Firth, R. J. H. Clark, and M. Cardona, J. Appl. Phys. **92**, 4375 (2002).

24. A. N. Kovalev, V. V. Ostroborodova, V. I. Paramonov, *et al.*, Fiz. Tekh. Poluprovodn. (Leningrad) **23**, 2039 (1989) [Sov. Phys. Semicond. **23**, 1260 (1989)].
25. L. V. Bochkareva, S. P. Zimin, and A. A. Sizyk, Fiz. Tekh. Poluprovodn. (Leningrad) **21**, 1594 (1987) [Sov. Phys. Semicond. **21**, 966 (1987)].
26. V. V. Shchennikov and A. V. Bazhenov, Rev. High Pressure Sci. Technol. **6**, 657 (1997).
27. K. Seeger, *Semiconductor Physics* (Springer, Berlin, 1974; Mir, Moscow, 1977).
28. E. S. Itskevich, L. M. Kashirskaya, I. V. Kucherenko, *et al.*, Pis'ma Zh. Éksp. Teor. Fiz. **43**, 303 (1986) [JETP Lett. **43**, 391 (1986)].
29. I. V. Kucherenko, L. M. Kashirskaya, K.-P. Mellman, *et al.*, Fiz. Tekh. Poluprovodn. (Leningrad) **23**, 1784 (1989) [Sov. Phys. Semicond. **23**, 1105 (1989)].
30. N. B. Brandt, O. N. Belousova, and V. P. Zlomanov, Fiz. Tverd. Tela (Leningrad) **19**, 437 (1977) [Sov. Phys. Solid State **19**, 250 (1977)].
31. B. A. Volkov, O. A. Pankratov, and A. V. Sazonov, Zh. Éksp. Teor. Fiz. **85**, 1395 (1983) [Sov. Phys. JETP **58**, 809 (1983)].
32. B. A. Volkov, O. Pankratov, and S. V. Pakhomov, Zh. Éksp. Teor. Fiz. **86**, 2293 (1984) [Sov. Phys. JETP **59**, 1336 (1984)].
33. G. A. Ivanov, E. K. Iordanishvili, V. L. Naletov, *et al.*, in *Low-Temperature Thermoelectric Materials*, Ed. by D. V. Gitsu (Akad. Nauk Mold. SSR, Kishinev, 1970).

Translated by V. Sakun

JETP Letters, Vol. 77, No. 2, 2003, pp. 94–98. From Pis'ma v Zhurnal Éksperimental'noĭ i Teoreticheskoĭ Fiziki, Vol. 77, No. 2, 2003, pp. 99–103.

Chemomagnetism, Magnetoconcentration Effect, and "Fishtail" Anomaly in Chemically Induced Granular Superconductors¶

S. A. Sergeenkov

Unitá di Ricerca INFM, Universitá di L'Aquila, Localitá Monteluco, 67040 Roio Poggio, Italy
Laboratory of Theoretical Physics, Joint Institute for Nuclear Research, Dubna, Moscow region, 141980 Russia

Received November 25, 2002; in final form, December 16, 2002

Within a 2D model of Josephson junction arrays (created by a 2D network of twin boundary dislocations with strain fields acting as an insulating barrier between hole-rich domains in underdoped crystals), a few novel effects expected to occur in intrinsically granular material are predicted, including (i) Josephson chemomagnetism (chemically induced magnetic moment in zero applied magnetic field) and its influence on a low-field magnetization (chemically induced paramagnetic Meissner effect) and (ii) the magnetoconcentration effect (creation of oxygen vacancies in applied magnetic field) and its influence on a high-field magnetization (the chemically induced analogue of the "fishtail" anomaly). The conditions under which these effects can be experimentally measured in nonstoichiometric high-T_c superconductors are discussed. © *2003 MAIK "Nauka/Interperiodica".*

PACS numbers: 74.25.Ha; 74.50.+r; 74.72.-h; 61.72.Mm

1. Recent STM-based imaging of the granular structure in underdoped $Bi_2Sr_2CaCu_2O_{8+\delta}$ crystals [1] revealed an apparent segregation of its electronic structure into superconducting domains (on the order of a few nanometers) located in an electronically distinct background. In particular, it was found that, at low levels of hole doping ($\delta < 0.2$), the holes become concentrated at certain hole-rich domains. (In this regard, it is interesting to mention the somewhat similar phenomenon of "chemical localization" that takes place in materials composed of atoms of only metallic elements exhibiting metal–insulator transitions [2].) Tunneling between such domains leads to intrinsic granular superconductivity (GS) in high-T_c superconductors (HTSs). Probably one of the first examples of GS was observed in $YBa_2Cu_3O_{7-\delta}$ single crystals in the form of the so-called "fishtail" anomaly of magnetization [3]. The granular behavior has been related to 2D clusters of oxygen defects forming twin boundaries (TBs) or dislocation walls within the CuO plane that restrict supercurrent flow and allow excess flux to enter the crystal. Indeed, there are serious arguments to consider the TBs in HTS as insulating regions of the Josephson SIS-type structure. The average distance between boundaries is substantially less than the grain size. In particular, networks of localized grain boundary dislocations with the spacing ranging from 10 to 100 nm which produce effectively continuous normal or insulating barriers at the grain boundaries have been observed [3]. It was also verified that the processes of oxygen ordering in HTSs leads to the continuous change of the lattice period along TBs with the change of the oxygen content. Additionally, the destruction of bulk superconductivity in these nonstoichiometric materials with increasing oxygen deficiency parameter μ was found to follow a classical percolation theory [4].

In addition to their importance for understanding the underlying microscopic mechanisms governing HTS materials, the above experiments provide rather versatile tools for designing chemically controlled atomic scale Josephson junctions (JJs) and their arrays (JJAs) with preselected properties needed for manufacturing modern quantum devices [5, 6]. Moreover, as we shall see below, GS-based phenomena can shed some light on the origin and evolution of the so-called paramagnetic Meissner effect (PME), which manifests itself both in high-T_c and conventional superconductors [7, 8] and is usually associated with the presence of π junctions and/or unconventional (*d*-wave) pairing symmetry. Recently, much attention has been given to both experimental and theoretical study of PME-related effects using specially designed SFS-type junctions [9, 10].

In this letter, within a 2D model of JJAs (created by a regular 2D network of TB dislocations), we discuss the possibility of a few novel interesting effects that are expected to occur in an intrinsically granular nonstoichiometric material. In particular, we shall consider (i) Josephson chemomagnetism (chemically induced magnetic moment in zero applied magnetic field) and

¶This article was submitted by the author in English.

its influence on low-field magnetization (chemically induced PME) and (ii) magnetoconcentration effect (the creation of extra oxygen vacancies in an applied magnetic field) and its influence on a high-field magnetization (the chemically induced analogue of the "fish-tail" anomaly).

2. The scenario. As is well known, the presence of a homogeneous chemical potential μ through a single JJ leads to the AC Josephson effect with time-dependent phase difference $\partial\phi/\partial t = \mu/\hbar$. In this paper, we will consider some effects in dislocation-induced JJ caused by a local variation of excess hole concentration $c(\mathbf{x})$ under chemical pressure (described by inhomogeneous chemical potential $\mu(\mathbf{x})$) equivalent to the presence of the strain field of 2D dislocation array $\epsilon(\mathbf{x})$ forming this Josephson contact.

To understand how GS manifests itself in nonstoichiometric crystals, let us invoke an analogy with the previously discussed dislocation models of grain boundary Josephson junctions (GBJJs) (see, e.g., [11, 12] and references therein). Recall that, under plastic deformation, grain boundaries (GBs) (which are the natural sources of weak links in HTSs) move rather rapidly via the movement of the grain boundary dislocations (GBDs) comprising these GBs. Using the above evidence, in the previous paper [12], we studied numerous piezomagnetic effects in granular superconductors under mechanical loading. At the same time, regular 2D dislocation networks of oxygen-depleted regions (generated by the dissociation of $\langle 110\rangle$ twinning dislocations) with the size d_0 of a few Burgers vectors, observed [1, 3, 13–15] in HTS single crystals and forming a triangular lattice with a spacing $d \geq d_0$ ranging from 10 to 100 nm, can provide quite a realistic possibility for the existence of a 2D Josephson network within the CuO plane. Recall furthermore that, in a *d*-wave orthorhombic YBCO crystal, TBs are represented by tetragonal regions (in which all dislocations are equally spaced by d_0 and have the same Burgers vectors **a** parallel to the *y* axis within the CuO plane), which produce screened strain fields [14] $\epsilon(\mathbf{x}) = \epsilon_0 e^{-|\mathbf{x}|/d_0}$ with $|\mathbf{x}| = \sqrt{x^2 + y^2}$.

Though in $YBa_2Cu_3O_{7-\delta}$ the ordinary oxygen diffusion $D = D_0 e^{-U_d/k_BT}$ is extremely slow even near T_c (due to the rather high value of the activation energy U_d in these materials, typically $U_d \simeq 1$ eV), in underdoped crystals (with oxygen-induced dislocations), there is a real possibility to facilitate oxygen transport via the so-called osmotic (pumping) mechanism [16, 17], which relates a local value of the chemical potential (chemical pressure) $\mu(\mathbf{x}) = \mu(0) + \nabla\mu \cdot \mathbf{x}$ with a local concentration of point defects as $c(\mathbf{x}) = e^{-\mu(\mathbf{x})/k_BT}$. Indeed, when in such a crystal there exists a nonequilibrium concentration of vacancies, a dislocation is moved an atomic distance *a* by adding excess vacancies to the extraplane edge. The produced work is simply equal to the chemical potential of the added vacancies. It is important that this mechanism allows us to explicitly incorporate the oxygen deficiency parameter δ into our model by relating it to the excess oxygen concentration of vacancies $c_v \equiv c(0)$ as $\delta = 1 - c_v$. As a result, the chemical potential of the single vacancy is $\mu_v \equiv \mu(0) = -k_BT\log(1-\delta) \simeq k_BT\delta$. Remarkably, the same osmotic mechanism was used by Gurevich and Pashitskii [14] to discuss the modification of oxygen vacancy concentration in the presence of the TB strain field. In particular, they argue that the change of $\epsilon(\mathbf{x})$ under an applied or chemically induced pressure results in a significant oxygen redistribution, producing a highly inhomogeneous filamentary structure of oxygen-deficient nonsuperconducting regions along GBs [15] (for underdoped superconductors, the vacancies tend to concentrate in the regions of compressed material). Hence, assuming the following connection between the variation of mechanical and chemical properties of planar defects, namely, $\mu(\mathbf{x}) = K\Omega_0\epsilon(\mathbf{x})$ (where Ω_0 is the effective atomic volume of the vacancy and *K* is the bulk elastic modulus), we can study the properties of TB-induced JJs under intrinsic chemical pressure $\nabla\mu$ (created by the variation of the oxygen doping parameter δ). More specifically, a single SIS-type junction (comprising a Josephson network) is formed around TBs due to a local depression of the superconducting order parameter $\Delta(\mathbf{x}) \propto \epsilon(\mathbf{x})$ over distance d_0, thus producing a weak link with (oxygen deficiency δ dependent) Josephson coupling $J(\delta) = \epsilon(\mathbf{x})J_0 = J_0(\delta)e^{-|\mathbf{x}|/d_0}$, where $J_0(\delta) = \epsilon_0 J_0 = (\mu_v/K\Omega_0)J_0 \simeq (k_BTJ_0/K\Omega_0)\delta$ (here, $J_0 \propto \Delta_0/R_n$ with R_n being the resistance of the junction). Thus, the model considered here indeed describes chemically induced GSs in underdoped systems (with $\delta \neq 0$) because, in accordance with the observations, for the stoichiometric situation (when $\delta \longrightarrow 0$), the Josephson coupling $J(\delta) \longrightarrow 0$ and the system loses its explicitly granular signature.

3. The model. To adequately describe the chemomagnetic properties of an intrinsically granular superconductor, we employ the model of a 2D overdamped Josephson junction array, which is based on the well-known tunneling Hamiltonian

$$\mathcal{H}(t) = \sum_{ij}^{N} J_{ij}[1 - \cos\phi_{ij}(t)] \qquad (1)$$

and introduces a short-range (nearest-neighbor) interaction between *N* junctions (which are formed around oxygen-rich superconducting areas with phases $\phi_i(t)$), arranged in a two-dimensional (2D) lattice with coordinates $\mathbf{x_i} = (x_i, y_i)$. The areas are separated by oxygen-poor insulating boundaries (created by TB strain fields $\epsilon(\mathbf{x}_{ij})$) producing a short-range Josephson coupling $J_{ij} = J_0(\delta)e^{-|\mathbf{x}_{ij}|/d}$. Thus, typically for granular superconductors, the Josephson energy of the array varies exponen-

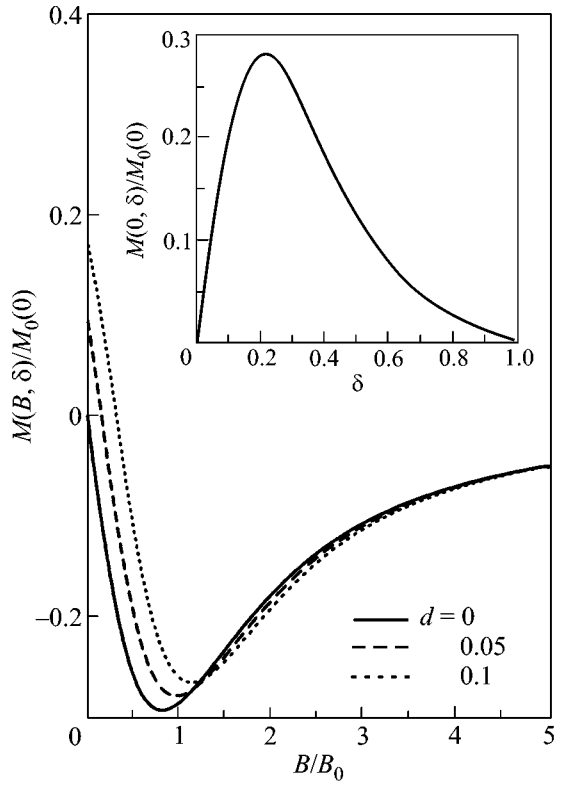

Fig. 1. The magnetization $M(B, \delta)/M_0(0)$ as a function of applied magnetic field B/B_0, according to Eq. (5), for different values of oxygen deficiency parameter: $\delta = 0$ (solid line), $\delta = 0.05$ (dashed line), and $\delta = 0.1$ (dotted line). Inset: δ induced magnetization $M(0, \delta)/M_0(0)$ in a zero applied magnetic field (chemomagnetism).

tially with the distance $\mathbf{x}_{ij} = \mathbf{x}_i - \mathbf{x}_j$ between neighboring junctions (with d being the average junction size).

If, in addition to chemical pressure $\nabla\mu(\mathbf{x}) = K\Omega_0\nabla\epsilon(\mathbf{x})$, the network of superconducting grains is under the influence of an applied frustrating magnetic field $\mathbf{B}$, the total phase difference through the contact is

$$\phi_{ij}(t) = \phi_{ij}^0 + \frac{\pi w}{\Phi_0}(\mathbf{x}_{ij} \wedge \mathbf{n}_{ij}) \cdot \mathbf{B} + \frac{\nabla\mu \cdot \mathbf{x}_{ij} t}{\hbar}, \qquad (2)$$

where ϕ_{ij}^0 is the initial phase difference (see below), $\mathbf{n}_{ij} = \mathbf{X}_{ij}/|\mathbf{X}_{ij}|$ with $\mathbf{X}_{ij} = (\mathbf{x}_i + \mathbf{x}_j)/2$, and $\omega = 2\lambda_L(T) + l$ with λ_L being the London penetration depth of the superconducting area and l being the insulator thickness (which, in the scenario discussed here, is simply equal to the TB thickness [17]).

To neglect the influence of self-field effects in a real material, the corresponding Josephson penetration length $\lambda_J = \sqrt{\Phi_0/2\pi\mu_0 j_c w}$ must be larger than the junction size d. Here, j_c is the critical current density of the superconducting (hole-rich) area. As we shall see below, this condition is rather well satisfied for HTS single crystals.

4. Chemomagnetism. Within our scenario, the sheet magnetization M of 2D granular superconductor is defined via the average Josephson energy of the array

$$\langle \mathcal{H} \rangle = \int_0^\tau \frac{dt}{\tau} \int \frac{d^2x}{s} \mathcal{H}(\mathbf{x}, t) \qquad (3)$$

as follows:

$$\mathbf{M}(\mathbf{B}, \delta) \equiv -\frac{\partial \langle \mathcal{H} \rangle}{\partial \mathbf{B}}, \qquad (4)$$

where $s = 2\pi d^2$ is the properly defined normalization area, τ is a characteristic Josephson time, and we have made the usual substitution

$$\frac{1}{N}\sum_{ij} A_{ij}(t) \longrightarrow \frac{1}{s}\int d^2x A(\mathbf{x}, t)$$

valid in the long-wavelength approximation [18].

To capture the very essence of the superconducting analogue of the chemomagnetic effect, in what follows we assume for simplicity that a *stoichiometric sample* (with $\delta = 0$) does not possess any spontaneous magnetization at zero magnetic field (that is, $M(0, 0) = 0$) and that its Meissner response to a small applied field B is purely diamagnetic (that is, $M(B, 0) \simeq -B$). According to Eq. (4), this condition implies $\phi_{ij}^0 = 2\pi m$ for the initial phase difference with $m = 0, \pm 1, \pm 2, \ldots$.

Taking the applied magnetic field along the c axis (and normal to the CuO plane), that is, $\mathbf{B} = (0, 0, B)$, we obtain finally

$$M(B, \delta) = -M_0(\delta)\frac{b - b_\mu}{(1 + b^2)(1 + (b - b_\mu)^2)} \qquad (5)$$

for the chemically induced sheet magnetization of the 2D Josephson network.

Here, $M_0(\delta) = J_0(\delta)/B_0$ with $J_0(\delta)$ defined earlier, $b = B/B_0$, and $b_\mu = B_\mu/B_0 \simeq (k_B T\tau/\hbar)\delta$, where $B_\mu(\delta) = (\mu_\nu(\delta)\tau/\hbar)B_0$ is the chemically induced contribution (which disappears in optimally doped systems with $\delta = 0$) and $B_0 = \Phi_0/wd$ is a characteristic Josephson field.

Figure 1 shows changes of the initial (stoichiometric) diamagnetic magnetization M/M_0 (solid line) with oxygen deficiency δ. As is seen, even relatively small values of the δ parameter render a low-field Meissner phase strongly paramagnetic (dotted and dashed lines). The inset of Fig. 1 presents a true *chemomagnetic* effect with concentration-deficiency-induced magnetization $M(0, \delta)$ in zero magnetic field. According to Eq. (5), the initially diamagnetic Meissner effect turns paramagnetic as soon as the chemomagnetic contribution $B_\mu(\delta)$ exceeds the applied magnetic field B. To see whether this can actually happen in a real material, let us estimate the magnitude of the chemomagnetic field B_μ. Typically [3, 14], for HTS single crystals, $\lambda_L(0) \approx 150$ nm

and $d \simeq 10$ nm, leading to $B_0 \simeq 0.5$ T. Using $\tau \simeq \hbar/\mu_v$ and $j_c = 10^{10} A/m^2$ as a pertinent characteristic time and the typical value of the critical current density, respectively, we arrive at the following estimate of the chemomagnetic field: $B_\mu(\delta) \simeq 0.5B_0$ for $\delta = 0.05$. Thus, the predicted chemically induced PME should be observable for applied magnetic fields $B \simeq 0.5B_0 \simeq 0.25$ T (which are actually much higher than the fields needed to observe the previously discussed [12] piezomagnetism and stress-induced PME in high-T_c ceramics). Notice that, for the above set of parameters, the Josephson length $\lambda_J \simeq 1$ μm, which means that the small-junction approximation assumed in this paper (with $d \ll \lambda_J$) is valid and the so-called "self-field" effects can be safely neglected.

5. Magnetoconcentration effect. So far, we have neglected the possible field dependence of the chemical potential μ_v of oxygen vacancies. However, in high enough applied magnetic fields B, the field-induced change of the chemical potential $\Delta\mu_v(B) \equiv \mu_v(B) - \mu_v(0)$ becomes tangible and must be taken into account. As is well known [19, 20], in a superconducting state, $\Delta\mu_v(B) = -M(B)B/n$, where $M(B)$ is the corresponding magnetization and n is the relevant carrier number density. At the same time, within our scenario, the chemical potential of a single oxygen vacancy μ_v depends on the concentration of oxygen vacancies (through the deficiency parameter δ). As a result, two different effects are possible, related, respectively, to the magnetic field dependence of $\mu_v(B)$ and to its dependence on magnetization $\mu_v(M)$. The former is nothing but a superconducting analogue of the so-called *magnetoconcentration* effect (which was predicted and observed in inhomogeneously doped semiconductors [21]) with field-induced creation of oxygen vacancies $c_v(B) = c_v(0)\exp(-\Delta\mu_v(B)/k_BT)$, while the latter (as we shall see in the next section) results in "fishtail" behavior of the magnetization. Let us start with the magnetoconcentration effect. Figure 2 depicts the predicted field-induced creation of oxygen vacancies $\delta(B) = 1 - c_v(B)$ using the magnetization $M(B, \delta)$ obtained above (see Fig. 1 and Eq. (5)). We also assumed, for simplicity, the complete stoichiometry of the system in zero magnetic field (with $\delta(0) = 1 - c_v(0) = 0$). Notice that $\delta(B)$ exhibits a maximum at $\delta_c \simeq 0.23$ for applied fields $B = B_0$ (in agreement with the classical percolative behavior observed in nonstoichiometric $YBa_2Cu_3O_{7-\delta}$ samples [3, 4, 15]). Finally, let us show that in underdoped crystals the above-discussed osmotic mechanism of oxygen transport is indeed much more effective than traditional diffusion. Using typical YBCO parameters [14], $\epsilon = 0.01$, $\Omega_0 = a_0^3$ with $a_0 = 0.2$ nm, and $K = 115$ GPa, we have $\mu_v(0) = \epsilon K\Omega_0 \simeq 1$ meV for a zero-field value of the chemical potential in HTS crystals, which leads to the creation of excess vacancies with concentration $c_v(0) = e^{-\mu_v(0)/k_BT} \simeq 0.7$ (equivalent to a deficiency value of $\delta(0) \simeq 0.3$) at $T = T_c$, while the probability of oxygen diffusion in these materials (governed by the rather high activation energy $U_d \simeq 1$ eV) is extremely slow under the same conditions, because $D \propto e^{-U_d/k_BT_c} \ll 1$. On the other hand, the change of the chemical potential in an applied magnetic field can reach as much as [20] $\Delta\mu_v(B) \simeq 0.5$ meV for $B = 0.5$ T, which is quite comparable with the above-mentioned zero-field value of $\mu_v(0)$.

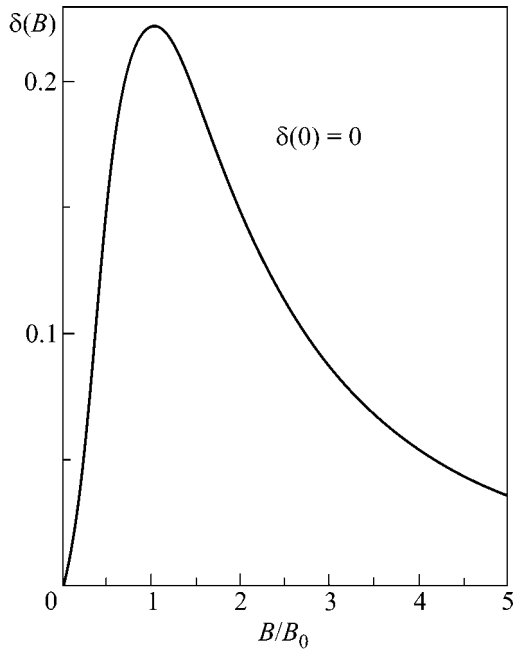

Fig. 2. Magnetic field dependence of the oxygen deficiency parameter $\delta(B)$ (magnetoconcentration effect).

6. Analogue of "fishtail" anomaly. Let us turn now to the second effect related to the magnetization dependence of the chemical potential $\mu_v(M(B))$. In this case, in view of Eq. (2), the phase difference will acquire an extra $M(B)$-dependent contribution, and, as a result, the r.h.s. of Eq. (5) will become a nonlinear functional of $M(B)$. The numerical solution of this implicit equation for the resulting magnetization $m_f = M(B, \delta(B))/M_0(0)$ is shown in Fig. 3 for the two values of zero-field deficiency parameter $\delta(0)$. As is clearly seen, m_f exhibits a field-induced fishtail-like behavior typical for underdoped crystals with intragrain granularity (for symmetry and a better visual effect, we also plotted $-m_f$ in the same figure). The extra extremum of the magnetization appears when the applied magnetic field B matches the intrinsic chemomagnetic field $B_\mu(\delta(B))$ (which now also depends on B via the above-discussed magnetoconcentration effect). Notice that the fishtail structure of m_f manifests itself even at zero values of field-free deficiency parameter $\delta(0)$ (solid line in Fig. 3), thus confirming the field-induced nature of intrinsic granu-

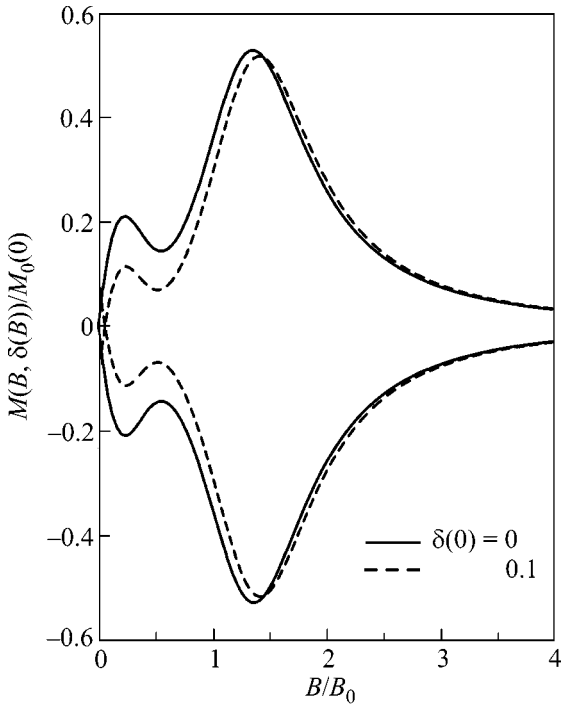

Fig. 3. The fishtail-like behavior of magnetization $m_f = M(B, \delta(B))/M_0(0)$ in applied magnetic field B/B_0in the presence of magnetoconcentration effect (with field-induced oxygen vacancies $\delta(B)$, see Fig. 2) for two values of field-free deficiency parameter: $\delta(0) = 0$ (solid line) and $\delta(0) = 0.1$ (dashed line).

larity [1, 3, 13–15]. At the same time, even a rather small deviation from the zero-field stoichiometry (with $\delta(0) = 0.1$) immediately brings about a paramagnetic Meissner effect at low magnetic fields. Thus, the present model predicts the appearance of two interrelated phenomena: Meissner paramagnetism at low fields and a "fishtail" anomaly at high fields. It would be very interesting to verify these predictions experimentally in nonstoichiometric superconductors with pronounced networks of planar defects.

I thank G. Rotoli and G. Filatrella for hospitality and interesting discussions on the subject. This work was done during my stay in L'Aquila and was funded by the Italian Institute for the Physics of Matter (INFM).

REFERENCES

1. K. M. Lang, V. Madhavan, J. E. Hoffman, *et al.*, Nature **415**, 412 (2002).
2. V. F. Gantmakher, Usp. Fiz. Nauk **172**, 1283 (2002) [Phys. Usp. **45** (2002)].
3. M. Daeumling, J. M. Seuntjens, D. C. Larbalestier, *et al.*, Nature **346**, 332 (1990); I. M. Babich and G. P. Mikitik, Pis'ma Zh. Éksp. Teor. Fiz. **64**, 538 (1996) [JETP Lett. **64**, 586 (1996)].
4. V. F. Gantmakher, A. M. Neminskii, and D. V. Shovkun, Pis'ma Zh. Éksp. Teor. Fiz. **52**, 1214 (1990) [JETP Lett. **52**, 630 (1990)].
5. See, e.g., *Mesoscopic and Strongly Correlated Electron Systems-II*, Ed. by M. V. Feigel'man, V. V. Ryazanov, and V. B. Timofeev; Phys. Usp. (Suppl.) **44** (10) (2001).
6. L. B. Ioffe, M. V. Feigel'man, A. Ioselevich, *et al.*, Nature **415**, 503 (2002).
7. V. Kataev, N. Knauf, W. Braunisch, *et al.*, Pis'ma Zh. Éksp. Teor. Fiz. **58**, 656 (1993) [JETP Lett. **58**, 636 (1993)]; A. K. Geim, S. V. Dubonos, J. G. S. Lok, *et al.*, Nature **396**, 144 (1998).
8. C. De Leo and G. Rotoli, Phys. Rev. Lett. **89**, 167001 (2002).
9. V. V. Ryazanov, V. A. Oboznov, A. Yu. Rusanov, *et al.*, Phys. Rev. Lett. **86**, 2427 (2001).
10. A. A. Golubov, M. Yu. Kupriyanov, and Ya. V. Fominov, Pis'ma Zh. Éksp. Teor. Fiz. **75**, 709 (2002) [JETP Lett. **75**, 588 (2002)].
11. E. Z. Meĭlikhov, Zh. Éksp. Teor. Fiz. **110**, 1453 (1996) [JETP **83**, 803 (1996)].
12. S. Sergeenkov, Pis'ma Zh. Éksp. Teor. Fiz. **70**, 36 (1999) [JETP Lett. **70**, 36 (1999)].
13. G. Yang, P. Shang, S. D. Sutton, *et al.*, Phys. Rev. B **48**, 4054 (1993).
14. A. Gurevich and E. A. Pashitskii, Phys. Rev. B **56**, 6213 (1997).
15. B. H. Moeckley, D. K. Lathrop, and R. A. Buhrman, Phys. Rev. B **47**, 400 (1993).
16. L. A. Girifalco, *Statistical Physics of Materials* (Wiley, New York, 1973).
17. S. Sergeenkov, J. Appl. Phys. **78**, 1114 (1995).
18. S. Sergeenkov, Pis'ma Zh. Éksp. Teor. Fiz. **76**, 204 (2002) [JETP Lett. **76**, 170 (2002)].
19. A. A. Abrikosov, *Fundamentals of the Theory of Metals* (Nauka, Moscow, 1987; Elsevier, Amsterdam, 1988).
20. S. Sergeenkov and M. Ausloos, Zh. Éksp. Teor. Fiz. **116**, 257 (1999) [JETP **89**, 140 (1999)].
21. A. A. Akopyan, S. S. Bolgov, A. P. Savchenko, *et al.*, Fiz. Tekh. Poluprovodn. (Leningrad) **24**, 1875 (1990) [Sov. Phys. Semicond. **24**, 1167 (1990)].

JETP Letters, Vol. 77, No. 2, 2003, pp. 99–103. From Pis'ma v Zhurnal Éksperimental'noĭ i Teoreticheskoĭ Fiziki, Vol. 77, No. 2, 2003, pp. 104–108.

Behavior of Fermi Systems Approaching the Fermion Condensation Quantum Phase Transition from the Disordered Phase¶

V. R. Shaginyan

St. Petersburg Nuclear Physics Institute, Russian Academy of Sciences, Gatchina, 188300 Russia
CTSPS, Clark Atlanta University, Atlanta, 30314 Georgia, USA
e-mail: vrshag@thd.pnpi.spb.ru

Received December 23, 2002

The behavior of Fermi systems that approach the fermion condensation quantum phase transition (FCQPT) from the disordered phase is considered. We show that the quasiparticle effective mass M^* diverges as $M^* \propto 1/|x - x_{FC}|$, where x is the system density and x_{FC} is the critical point at which FCQPT occurs. Such behavior is of general form and takes place in both three-dimensional (3D) and two-dimensional (2D) systems. Since the effective mass M^* is finite, the system exhibits the Landau Fermi liquid behavior. At $|x - x_{FC}|/x_{FC} \lll 1$, the behavior can be viewed as highly correlated, because the effective mass is large and strongly depends on the density. In the case of electronic systems, the Wiedemann–Franz law is valid and the Kadowaki–Woods ratio is preserved. Beyond the region $|x - x_{FC}|/x_{FC} \lll 1$, the effective mass is approximately constant and the system becomes a conventional Landau Fermi liquid. © *2003 MAIK "Nauka/Interperiodica".*

PACS numbers: 71.10.Hf; 71.27.+a; 71.10.Ay

It is widely believed that the unusual properties of the strongly correlated liquids observed in high-temperature superconductors, heavy-fermion metals, 2D ^{3}He, etc., are determined by quantum phase transitions. Any quantum phase transition occurs at temperature $T = 0$ and is driven by a control parameter other than temperature, for instance, by pressure, magnetic field, or the density x. A quantum phase transition occurs at the quantum critical point. As any phase transition, the quantum phase transition is related to the order parameter that induces a broken symmetry. Therefore, direct experimental studies of relevant quantum phase transitions are of crucial importance for understanding the physics of high-temperature superconductivity and strongly correlated systems.

In the case of high-temperature superconductors, these experiments are difficult to carry out, because at low temperatures all the corresponding area is occupied by the superconductivity. On the other hand, experimental data on the behavior of different Fermi liquids when systems approach the critical point from the disordered phase can help to illuminate both the nature of this point and the nature of the control parameter by which this phase transition is driven. Experimental facts on high-density 2D ^{3}He [1, 2] show that the effective mass diverges when the density at which the 2D ^{3}He liquid begins to solidify is approached [2]. Then a sharp increase of the effective mass in a metallic 2D electron system is observed when the density tends to the critical density of the metal–insulator transition point. This transition occurs at sufficiently low densities [3]. Note that there is no ferromagnetic instability in either Fermi system, and the relevant Landau amplitude $F_0^a > -1$ [2, 3], in accordance with the almost localized fermion model [4].

Recent measurements for nonsuperconducting $La_{1.7}Sr_{0.3}CuO_4$ have shown that the resistivity ρ exhibits T^2 behavior, $\rho = \rho_0 + \Delta\rho$, with $\Delta\rho = AT^2$, which the Wiedemann–Franz (WF) law is verified to hold perfectly, and that the Kadowaki–Woods ratio, A/γ_0^2 [5], is enhanced compared with heavy-fermion metals [6]. Here, γ_0 is the linear specific heat coefficient, $C = \gamma_0 T$. These data demonstrate the behavior of the Fermi liquid located above the critical point or on the side of the disordered phase.

In this letter, we study the behavior of Fermi systems that approach the fermion condensation quantum phase transition (FCQPT) [7] from the disordered phase and show that the outlined experimental data can be explained within the framework of our approach. We analyze the appearance of FCQPT in different 2D and 3D Fermi liquids and show that at $T \longrightarrow 0$ FCQPT manifests itself in the divergence of the quasiparticle effective mass M^* as the density x of a system approaches the critical point x_{FC} at which FCQPT takes place, so that $M^* \propto 1/|x - x_{FC}|$. Since the effective mass M^* is finite, the system exhibits Landau Fermi liquid

¶This article was submitted by the author in English.

(LFL) behavior at low temperatures. At sufficiently high temperatures, the system has non-Fermi liquid (NFL) behavior. At $|x - x_{FC}|/x_{FC} \ll 1$, this behavior can be viewed as highly correlated, because the effective mass strongly depends on the density and is large. We show that, in the case of electronic systems, the WF law is valid, and the Kadowaki–Woods ratio is preserved. Beyond the region $|x - x_{FC}|/x_{FC} \ll 1$, the effective mass is approximately constant and the system becomes a conventional Landau Fermi liquid.

A new state of Fermi liquid with the fermion condensate (FC) [8, 9], which takes place beyond the critical point x_{FC}, is defined by the equation [8]

$$\frac{E[n(p)]}{\delta n(\mathbf{p})} - \mu = \varepsilon(\mathbf{p}) - \mu = 0, \quad \text{if } 0 < n(\mathbf{p}) < 1; \quad p_i \le p \le p_f \in L_{FC}. \tag{1}$$

Here, $E[n(p)]$ is the Landau functional of the ground state energy, $n(\mathbf{p})$ is the quasiparticle distribution function, $\varepsilon(\mathbf{p})$ is the single-particle energy of the quasiparticles, and μ is the chemical potential [10]. At $T = 0$, Eq. (1) defines a new state of Fermi liquid with the FC for which the modulus of the superconducting order parameter $|\kappa(\mathbf{p})|$ has finite values in the L_{FC} range of momenta $p_i \le p \le p_f$ occupied by FC. At the same time, the superconducting gap can be infinitely small, $\Delta_1 \longrightarrow 0$ in L_{FC}, provided that the corresponding pairing interaction is also small [7, 8]. Such a state can be considered as superconducting, with an infinitely small value of Δ_1, so that the entropy of this state is equal to zero. This state, created by the quantum phase transition, disappears at $T > 0$. FCQPT can be considered as a "pure" quantum phase transition, because it cannot take place at finite temperatures. Therefore, the corresponding quantum critical point does not represent the end of a line of continuous phase transitions at $T = 0$. Nonetheless, FCQPT has a strong impact on the system's properties up to temperature T_f, above which FC effects become insignificant [7, 8]. FCQPT does not violate any rotational symmetry or translational symmetry, being characterized by the order parameter $\kappa(\mathbf{p}) = \sqrt{n(\mathbf{p})(1 - n(\mathbf{p}))}$. It follows from Eq. (1) that the quasiparticle system splits into two quasiparticle subsystems: the first one, in L_{FC} range, is occupied by quasiparticles with the effective mass $M^*_{FC} \propto 1/\Delta_1$, while the second by quasiparticles with finite mass M^*_L and momenta $p < p_i$. Note that the existence of such a state can be revealed experimentally. Since the order parameter $\kappa(\mathbf{p})$is suppressed by a magnetic field B, when $B^2 \sim \Delta_1^2$, a weak magnetic field B will destroy the state, with FC converting the strongly correlated Fermi liquid into a normal Landau Fermi liquid.

Equation (1), possessing solutions at some density $x = x_{FC}$, determines the critical point of FCQPT. It is also evident from Eq. (1) that the effective mass diverges when $x \longrightarrow x_{FC}$, $M^*_L (x \longrightarrow x_{FC}) \longrightarrow \infty$. Let us assume that FC has just taken place, $p_i \longrightarrow p_f \longrightarrow p_F$, and the deviation $\delta n(p)$ is small. Expanding functional $E[n(p)]$ in a Taylor series with respect to $\delta n(p)$ and retaining the leading terms, one obtains

$$\mu = \varepsilon(\mathbf{p}, \sigma) = \varepsilon_0(\mathbf{p}, \sigma) + \sum_{\sigma_1} \int F_L(\mathbf{p}, \mathbf{p}_1, \sigma, \sigma_1) \delta n(\mathbf{p}_1, \sigma_1) \frac{d\mathbf{p}_1}{(2\pi)^2}; \quad p_i \le p \le p_f \in L_{FC}. \tag{2}$$

In Eq. (2), $F_L(\mathbf{p}, \mathbf{p}_1, \sigma, \sigma_1) = \delta^2 E/\delta n(\mathbf{p}, \sigma)\delta n(\mathbf{p}_1, \sigma_1)$ is the Landau interaction [10], and σ denotes the spin states. Both the Landau interaction and the single-particle energy $\varepsilon_0(p)$ are calculated at $n(p) = n_F(p)$. Here, $n_F(p) = \theta(p_F - p)$ and $\theta(p - p_F)$ is the Fermi–Dirac distribution at $T = 0$. Equation (2) has solutions when the Landau amplitude F_L is positive and sufficiently large, so that the integral on the right-hand side of Eq. (2) defining the potential energy is large, and therefore the potential energy prevails over the kinetic energy $\varepsilon_0(\mathbf{p})$ [8]. At temperatures $T \ge T_c$, the effective mass M^*_{FC} related to FC is given by [7, 11]

$$M^*_{FC} \simeq p_F \frac{p_f - p_i}{4T}. \tag{3}$$

Multiplying both sides of Eq. (3) by $p_f - p_i$, we obtain the energy scale E_0 separating the slowly dispersing low-energy part related to the effective mass M^*_{FC} from the faster-dispersing relatively high-energy part defined by the effective mass M^*_L [7, 11]:

$$E_0 \simeq 4T. \tag{4}$$

It is clear from Eq. (4) that the scale E_0 does not depend on the range $p_f - p_i$. It is natural to assume that we have returned back to the Landau theory by integrating out high-energy degrees of freedom and introducing the quasiparticles. The sole difference between the Landau Fermi liquid and a Fermi liquid having undergone FCQPT is that we have to expand the number of relevant low-energy degrees of freedom by introducing a new type of quasiparticle with the effective mass M^*_{FC} given by Eq. (3) and the energy scale E_0 given by Eq. (4). It is seen from Eqs. (1) and (2) that the FC quasiparticles form a collective state, since their energies are defined by the macroscopic number of quasiparticles within the region $p_i - p_f$. The shape of the spectra is not affected by the Landau interaction, which, generally speaking, depends on the system's properties, including the collective states, impurities, etc. The only thing defined by the interaction is the width of the region $p_i - p_f$, provided that the interaction is suffi-

ciently strong to produce the FC phase transition at all. The spectra related to FC are of universal form and determined by T, as follows from Eq. (3). Thus, the system's properties and dynamics are dominated by a strong collective effect originating from FCQPT and determined by the macroscopic number of quasiparticles in the range L_{FC}. Such a system can be viewed as a strongly correlated system and cannot be disturbed by the scattering of individual quasiparticles, thermal excitations, impurities, etc., and has features of a quantum protectorate [7, 12, 13].

The appearance of FCQPT in Fermi liquids, when the effective interaction becomes sufficiently large, was predicted in [14]. FCQPT precedes the formation of charge-density waves or stripes, which take place at some value $x = x_{cdw}$ with $x_{FC} > x_{cdw}$, while the Wigner solidification takes place at even lower values of x and leads to an insulator. In the same way, the effective mass inevitably diverges as soon as the density x becomes sufficiently large approaching the critical density at which 2D ^{3}He begins to solidify, as was observed in [2].

Now we consider the divergence of the effective mass in 2D and 3D Fermi liquids at $T = 0$, when the density x approaches FCQPT from the side of the normal LFL. First, we calculate the divergence of M^* as a function of the difference $(x_{FC} - x)$ in the case of 2D ^{3}He. For this purpose, we use the equation for M^* obtained in [14], where the divergence of the effective mass M^* due to the onset of FC in different Fermi liquids including ^{3}He was predicted:

$$\frac{1}{M^*} = \frac{1}{M} + \frac{1}{4\pi^2}\int_{-1}^{1}\int_{0}^{g_0}\frac{v(q(y))}{[1 - R(q(y), \omega = 0, g)\chi_0(q(y), \omega = 0)]^2}\frac{ydydg}{\sqrt{1-y^2}}. \quad (5)$$

Here, we adopt the shorthand $p_F\sqrt{2(1-y)} = q(y)$, where $q(y)$ is the transferred momentum, M is the bare mass, ω is the frequency, $v(q)$ is the bare interaction, and the integral is taken over the coupling constant g from zero to its real value g_0. In Eq. (5), both $\chi_0(q, \omega)$ and $R(q, \omega)$, being the linear response function of noninteracting Fermi liquid and the effective interaction, respectively, define the linear response function of the system under consideration:

$$\chi(q, \omega, g) = \frac{\chi_0(q, \omega)}{1 - R(q, \omega, g)\chi_0(q, \omega)}. \quad (6)$$

In the vicinity of charge-density wave instability, occurring at the density x_{cdw}, the singular part of the function χ^{-1} on the disordered side is of the well-known form (see, e.g., [15])

$$\chi^{-1}(q, \omega, g) \propto (x_{cdw} - x) + (q - q_c)^2 + (g_0 - g), \quad (7)$$

where $q_c \sim 2p_F$ is the wave number of the charge-density wave. Upon substituting Eq. (7) into Eq. (5) and performing the integrations, the equation for the effective mass M^* can be cast in the form [16]

$$\frac{1}{M^*} = \frac{1}{M} - \frac{C}{\sqrt{x_{cdw} - x}}, \quad (8)$$

where C is some positive constant. It is seen from Eq. (8) that M^* diverges at some point x_{FC}, which is referred to as the critical point, as a function of the difference $(x_{FC} - x)$

$$M^* \sim M\frac{x_{FC}}{x_{FC} - x}. \quad (9)$$

It follows from the derivation of Eqs. (8) and (9) that the form of these equations is independent of the bare interaction $v(q)$; therefore, both of these equations are also applicable to a 2D electron liquid or to another Fermi liquid. It is also seen from Eqs. (8) and (9) that FCQPT precedes the formation of charge-density waves. As a consequence of this, the effective mass diverges at high densities in the case of 2D ^{3}He, and it diverges at low densities in the case of 2D electron systems, in accordance with experimental facts [2, 3]. Note that in both cases the difference $(x_{FC} - x)$ has to be positive, because x_{FC} represents the solution of Eq. (8). Thus, considering electron systems, we have to replace $(x_{FC} - x)$ with $(x - x_{FC})$. In the case of a 3D system, the effective mass is given by [14]

$$\frac{1}{M^*} = \frac{1}{M} + \frac{p_F}{4\pi^2}\int_{-1}^{1}\int_{0}^{g_0}\frac{v(q(y))ydydg}{[1 - R(q(y), \omega = 0, g)\chi_0(q(y), \omega = 0)]^2}. \quad (10)$$

A comparison of Eq. (10) and Eq. (5) shows that there is no fundamental difference between these equations, and along the same lines we again arrive at Eqs. (8) and (9). The only difference between 2D electron systems and 3D ones is that FCQPT occurs at densities that are well below those corresponding to 2D systems, while, in the bulk ^{3}He, FCQPT probably cannot take place, being absorbed by the first-order solidification.

In deriving Eq. (9), we assumed that the temperature $T = 0$. It is seen from Eq. (3) that the effective mass decreases when the temperature increases. The same is true when the system is above the critical point. Therefore, when T exceeds some temperature $T^*(x)$, Eq. (9) is no longer valid, and M^* depends on the temperature as well. To estimate $T^*(x)$, we can compare the deviation $\Delta x = |x - x_{FC}|$ with the deviation $\Delta x(T)$, generated by T. The deviation Δx can be expressed in terms of $M^*(x)$ using Eq. (9), $\Delta x/x \sim M/M^*(x)$. On the other hand, the temperature smoothing out the Fermi function $\theta(p_F - p)$ at p_F induces the variation $p_F\Delta p/M^*(x) \sim T$.

As a result, we have $\Delta x(T)/x \sim M^*(x)T/p_F^2$. Comparing these deviations, we find that at $T \geq T^*(x)$ the effective mass depends noticeably on the temperature, and the equation for $T^*(x)$ becomes

$$T^*(x) \sim p_F^2 \frac{M}{(M^*(x))^2} \sim \varepsilon_F(x)\left(\frac{M}{M^*(x)}\right)^2. \quad (11)$$

Here, $\varepsilon_F(x)$ is the Fermi energy of noninteracting electrons with mass M. From Eq. (11) it follows that M^* is always finite, provided that $T > 0$. We can consider $T^*(x)$ as the energy scale $e_0(x) \simeq T^*(x)$. This scale defines the area $(\mu - e_0(x))$ in the single-particle spectrum where M^* is approximately constant, being given by $M^* = d\varepsilon(p)/dp$ [10]. According to Eqs. (9) and (11), it is easily verified that $e_0(x)$ can be written in the form

$$e_0(x) \sim \varepsilon_F\left(\frac{x - x_{FC}}{x_{FC}}\right)^2. \quad (12)$$

At $T \ll e_0(x)$ and above the critical point, the effective mass $M^*(x)$ is finite, the energy scale E_0 given by Eq. (4) vanishes, and the system exhibits LFL behavior. At temperatures $T \geq e_0(x)$, the effective mass M^* starts to depend on the temperature, and NFL behavior is observed. Thus, at $|x - x_{FC}|/x_{FC} \ll 1$, the system can be considered as highly correlated: at $T \ll e_0(x)$, the system is LFL, while, at temperatures $T \geq e_0(x)$, the system possesses NFL behavior. Then, it is clear that at $T \longrightarrow 0$ the WF law is preserved. At $|x - x_{FC}|/x_{FC} \ll 1$, the effective mass given by Eq. (9) is very large, the Kadowaki–Woods ratio A/γ_0^2 is obeyed, and the resistivity exhibits T^2 behavior, as was demonstrated within a simple model of highly correlated liquid [17]. On the other hand, at $T \geq e_0(x)$, strong deviations from T^2 behavior occur. We suppose that the resistivity follows a T^α dependence with $1 < \alpha < 2$ at $T \geq e_0(x)$. Here, $\alpha = 1$ corresponds to a strongly correlated liquid with FC and $\alpha = 2$ corresponds to LFL [7, 17]. We note that the outlined behavior was observed in several heavy-fermion metals [15]. When the system's density x is outside the region $|x - x_{FC}|/x_{FC} \ll 1$, the scale e_0 becomes comparable with the Fermi level, and the effective mass becomes $M^* \sim M$ and is approximately constant at energies $(\mu - \varepsilon) \leq e_0$. Therefore, the system becomes a normal Landau Fermi liquid.

We can expect to observe such a highly correlated electron (or hole) liquid in heavily overdoped high-T_c compounds, which are located beyond the superconducting dome. Let us recall that, beyond the FCQPT point, the superconducting gap Δ_1 can be very small or even absent [18]. Indeed, recent experimental data have shown that this liquid does exist in heavily overdoped nonsuperconducting $La_{1.7}Sr_{0.3}CuO_4$ [6]. Note that, up to $T = 55$ K, the resistivity exhibits T^2 behavior, while, at $T \geq 100$ K, the resistivity follows a $T^{1.6}$ dependence [6]. Thus, we can estimate that $e_0(x) \sim 50$ K.

Now consider $M^*(B)$ as a function of a weak external magnetic field B at finite temperatures. The density x belongs to the area $(x - x_{FC})/x \ll 1$, and the electron system in question is highly correlated. The case when the system has undergone FCQPT was studied in [19]. This consideration will be applicable to any 2D or 3D electronic Fermi system. The application of a magnetic field B leads to a weakly polarized state, or Zeeman splitting, when some levels at the Fermi level are occupied by spin-up polarized quasiparticles. The width $\delta p = p_{F1} - p_{F2}$ of the area in the momentum space occupied by these quasiparticles is on the order of

$$p_F \delta p/M^* \sim B\mu_{\text{eff}}. \quad (13)$$

Here, $\mu_{\text{eff}} \sim \mu_B$ is the electron magnetic effective moment, p_{F1} is the Fermi momentum of the spin-up electrons, and p_{F2} is the Fermi momentum of the spin-down electrons. As a result, the Zeeman splitting leads to the change Δx in the density x

$$\Delta x/x_{FC} \sim \delta p^2/p_F^2. \quad (14)$$

We assume that $\Delta x/x_{FC} \ll 1$. Now, it follows from Eqs. (9) and (14) that

$$M^*(B) \sim M(\varepsilon_F/B\mu_{\text{eff}})^{2/3}. \quad (15)$$

We note that M^* is determined by Eq. (15) as long as $M^*(B) \leq M^*(x)$; otherwise, we have to use Eq. (9). It follows from Eq. (15) that the application of a magnetic field reduces the effective mass. At finite temperatures $T \leq T^*(x)$, the effective mass is given by Eq. (15). At temperatures $T \sim T^*(x)$, both the magnetic field and temperature contribute to the decrease in M^*. At $T^*(x) \ll T$, the effective mass is a diminishing function of the temperature. It is clear from Eq. (15) that $M^*(B)$ remains finite even at $x \longrightarrow x_{FC}$ and $T \longrightarrow 0$. In that case, the effective mass $M^*(x)$ in Eq. (11) has to be replaced by $M^*(B)$. The behavior described above can be visualized by measuring the magnetic susceptibility $\chi(T)$ at finite magnetic field, so that $M^*(x) \geq M^*(B)$. The function $\chi(T)$ is a decreasing function of T at $T \sim e_0$. At $T \ll e_0$, the function $\chi(T)$ becomes independent of T and starts to depend on B, being a decreasing function of B.

Let us comment briefly on the problem of realization of the highly correlated liquid in dilute Fermi gases and in low-density neutron matter. We consider an infinitely extended system composed of Fermi particles, or atoms, interacting by an artificially constructed potential with the desirable scattering length a. These objects may be viewed as trapped Fermi gases, which are systems composed of Fermi atoms interacting by a potential with almost any desirable scattering length, similarly to that done for the trapped Bose gases (see, e.g., [20]). If a is negative, the system becomes unstable at densities $x \sim |a|^{-3}$, provided that the scattering length is

the dominant parameter of the problem. This means that $|a|$ is much larger than the radius of the interaction or any other relevant parameter of the system. The compressibility $K(x)$ vanishes at the density $x_{c1} \sim |a|^{-3}$, making the system completely unstable [21]. Expressing the linear response function in terms of the compressibility [22],

$$\chi(q \longrightarrow 0, i\omega \longrightarrow 0) = -(d^2E/d\rho^2)^{-1}, \qquad (16)$$

we find that the linear response function has a pole at the origin, $q \simeq 0$, $\omega \simeq 0$, at the same point x_{c1}. To find the behavior of the effective mass M^* as a function of the density, we substitute Eq. (7) into Eq. (10) taking into account the fact that x_{cdw} is replaced by x_{c1} and $q_c/p_F \ll 1$ due to Eq. (16). At low momenta $q/p_F \sim 1$, the potential $v(q)$ is attractive, because the scattering length is the dominant parameter and is negative. Therefore, the integral on the right-hand side of Eq. (10) is negative and diverges at $x \longrightarrow x_{1c}$. The above consideration can be applied to clarify the fact that the effective mass M^* is again given by Eq. (9) with $x_{FC} < x_{c1}$. Note that the superfluid correlations cannot stop the system from squeezing, since their contribution to the ground state energy is negative. After all, the superfluid correlations can be considered as additional degrees of freedom, which can therefore only decrease the energy. We conclude that highly correlated behavior can be observed in traps by measuring the density of states at the Fermi level, which becomes extremely large as $x \longrightarrow x_{FC}$. At these densities, the system remains stable because $x_{FC} < x_{c1}$. It seems quite probable that the neutron–neutron scattering length ($a \simeq -20$ fm) is sufficiently large to make it the dominant parameter and to permit the neutron matter to have an equilibrium energy, equilibrium density, and a singular point x_{c1} at which the compressibility vanishes [23]. Therefore, we can expect FCQPT to take place in low-density neutron matter, leading to the stabilization of the matter by lowering its ground state energy. A more detailed analysis of this issue will be published elsewhere.

To conclude, we have shown that our simple model based on FCQPT can explain the main features of the highly correlated liquid observed in different Fermi liquids. Thus, FCQPT can be viewed as a universal cause of highly correlated behavior.

I am grateful to CTSPS for the hospitality during my stay in Atlanta. I also thank G. Japaridze for fruitful discussions. This work was supported in part by the Russian Foundation for Basic Research, project no. 01-02-17189.

REFERENCES

1. K.-D. Morhard, C. Bauerle, J. Bossy, *et al.*, Phys. Rev. B **53**, 2658 (1996).
2. A. Casey *et al.*, J. Low Temp. Phys. **113**, 293 (1998).
3. A. A. Shashkin, S. V. Kravchenko, V. T. Dolgopolov, and T. M. Klapwijk, Phys. Rev. B **66**, 073303 (2002).
4. M. Pfitzner and P. Wölfe, Phys. Rev. B **33**, 2003 (1986).
5. K. Kadowaki and S. B. Woods, Solid State Commun. **58**, 507 (1986).
6. S. Nakamae *et al.*, cond-mat/0212283.
7. M. Ya. Amusia and V. R. Shaginyan, Pis'ma Zh. Éksp. Teor. Fiz. **73**, 268 (2001) [JETP Lett. **73**, 232 (2001)]; S. A. Artamonov and V. R. Shaginyan, Zh. Éksp. Teor. Fiz. **119**, 331 (2001) [JETP **92**, 287 (2001)]; M. Ya. Amusia and V. R. Shaginyan, Phys. Rev. B **63**, 224507 (2001); V. R. Shaginyan, Physica B & C (Amsterdam) **312–313**, 413 (2002).
8. V. A. Khodel and V. R. Shaginyan, Pis'ma Zh. Éksp. Teor. Fiz. **51**, 488 (1990) [JETP Lett. **51**, 553 (1990)]; V. A. Khodel, V. R. Shaginyan, and V. V. Khodel, Phys. Rep. **249**, 1 (1994).
9. G. E. Volovik, Pis'ma Zh. Éksp. Teor. Fiz. **53**, 208 (1991) [JETP Lett. **53**, 222 (1991)].
10. L. D. Landau, Zh. Éksp. Teor. Fiz. **30**, 1058 (1956) [Sov. Phys. JETP **3**, 920 (1956)].
11. M. Ya. Amusia, S. A. Artamonov, and V. R. Shaginyan, Pis'ma Zh. Éksp. Teor. Fiz. **74**, 396 (1998) [JETP Lett. **74**, 396 (2001)].
12. R. B. Laughlin and D. Pines, Proc. Natl. Acad. Sci. USA **97**, 28 (2000).
13. P. W. Anderson, cond-mat/007185; cond-mat/0007287.
14. V. A. Khodel, V. R. Shaginyan, and M. V. Zverev, Pis'ma Zh. Éksp. Teor. Fiz. **65**, 242 (1997) [JETP Lett. **65**, 253 (1997)].
15. C. M. Varma, Z. Nussinov, and Wim van Saarloos, Phys. Rep. **361**, 267 (2002).
16. V. R. Shaginyan, cond-mat/0208568.
17. V. A. Khodel and P. Schuck, Z. Phys. B **104**, 505 (1997).
18. M. Ya. Amusia and V. R. Shaginyan, Pis'ma Zh. Éksp. Teor. Fiz. **76**, 774 (2002) [JETP Lett. **76**, 651 (2002)].
19. Yu. G. Pogorelov and V. R. Shaginyan, Pis'ma Zh. Éksp. Teor. Fiz. **76**, 614 (2002) [JETP Lett. **76**, 532 (2002)].
20. S. Inouye *et al.*, Nature **392**, 151 (1998).
21. M. Ya. Amusia, A. Z. Msezane, and V. R. Shaginyan, Phys. Lett. A **293**, 205 (2002).
22. L. D. Landau and E. M. Lifshitz, *Statistical Physics*, 3rd ed. (Nauka, Moscow, 1976; Addison-Wesley, Reading, MA, 1970), Part 1.
23. M. Ya. Amusia and V. R. Shaginyan, Eur. Phys. J. A **8**, 77 (2000).